Université de Neuchâtel
Institut de Microtechnique

Liquid crystal diffractive optical elements

Thèse

Présentée à la faculté des sciences
pour obtenir le grade de docteur ès sciences
par

Manuel Bouvier

Neuchâtel, Juillet 2000

UFO Dissartation Band 396

Die Deutsche Bibliothek – CIP-Einheitsaufnahme

Ein Titelsatz für diese Publikation ist bei Der Deutschen Bibliothek erhältlich.

Dissertation der Universität Neuchâtel
Datum der mündlichen Prüfung: 21.11.2000
Referenten: Prof. Dr. R. Dändliker
Dr. H.-P. Herzig
Dr. J. Grupp
Dr. P. Ambs

UFO Atelier für Gestaltung & Verlag GbR
D-78476 Allensbach
Internet www.ufo-verlag.de
Erste Auflage 2001

ISBN 3-930803-96-8

IMPRIMATUR POUR LA THESE

Liquid crystal diffractive optical elements

de M. Manuel Bouvier

UNIVERSITE DE NEUCHATEL

FACULTE DES SCIENCES

La Faculté des sciences de l'Université de Neuchâtel sur le rapport des membres du jury,

MM. R. Dändliker (directeur de thèse), H.-P. Herzig, J. Grupp (Asulab, Marin) et P. Ambs (Mulhouse)

autorise l'impression de la présente thèse.

Neuchâtel, le 21 novembre 2000

Le doyen:

J.-P. Derendinger

Contents

Abstract

This thesis deals with the diffractive devices that can be realized with planar-nematic liquid crystals. A large part of this work consists of computer calculations done for one, two and three-dimensional models of liquid crystal devices like Twisted Nematic switches, blazed gratings and lenses, respectively. The calculations are made not only to know how the molecules are rearranged by the electric field applied, but also to know the phase modulation of light and the far-field image after propagation. Special interest has been put in two-dimensional spatial phase modulators like binary gratings and multilevel gratings. They can be reconfigured so that a tunable hologram becomes available. To prove the validity of the calculations, prototypes have been constructed and measured, giving a good agreement with the calculation. The results can be easily extended to lenses or other three-dimensional phase modulators based on the same configurations as the gratings.

Introduction

Multiplexing of the optical beams of the fiber optics is a major issue in the telecommunication systems nowadays. In the early days, the combination of fiber optics for long distance communication and the classical cable transmission for the connection with the end user allowed to convert the optical signal into a electrical one by means of photo-detectors and then do the multiplexing of the signal electronically. Nevertheless, the connection between nodes by fiber optics requires an optical to electrical and back to optical conversion of the signal making the systems heavy since a new optical source is required. Electro-optical switching can be one possible solution for those systems.

Electro-optical transparent switches are switches for optical signals that do not make the optical to electrical and back to optical conversion to allow the multiplexing of the signal. In this domain, two solution are available. The most recent is to use micro-mirrors or deformable reflective membranes resulting from the new advances in photolithographic processes. Several version of these have been presented. Binary micro-mirrors are electro-statically driven and are actually used for recent projection devices. Reflective membranes with a matrix of electrodes to perform deformation on the film are actually used in adaptive optics.

Another possibility is to use liquid crystal devices. The great advantage of these devices is the low production cost. The technology actually required is well known and although liquid crystals mixtures are relatively expensive, the volume required is minimal. Electrical driving requirements are also uncritical, with rms values below 5 V at 1kHz for square signals.

The present work concerns planar-nematic liquid crystal devices. These devices are intended to spatially modulate the phase retardation of a linearly polarized laser beam. This is done by modulating the orientation of the liquid crystal molecules so that the effective birefringence is spatially modulated. The modulation is obtained through arrays of electrodes with a single applied voltage in the case of binary and sinusoidal gratings, or a freely configurable set of voltages for blazed gratings, lenses or reconfigurable holograms in general.

Special interest has been put on the modelization of those devices. Based on finite difference

calculation, a commercial software like LCDMaster allows to modelize the spatial rearrangement of the liquid crystal molecules by the presence of a complex electric field. With the resulting arrangement, matrix calculations allow to obtain the phase modulation originated by the device. Finally the propagation into the far-field of the modulated wavefront is calculated by means of Fourier transforms.

The thesis has the following structure:

Chapter 1 is dedicated to the basic properties of liquid crystals that are required to understand how the devices work. This includes the different anisotropies, that is, dielectric anisotropy for the reorientation through external electric fields, elastic anisotropy that results in different kinds of rearrangement depending on the reorientation through the electric field and also the birefringence which is responsible for the optical phase modulation.

Chapter 2 is a brief introduction to the technology used for the fabrication of the devices and a discussion of problems and alternative techniques proposed or developed.

Chapter 3 concerns the model and software used for the simulation of distorted nematic liquid crystal media under the action of an external electric field. A commercial software (LCD-Master[1]) based on the Frank-Oseen model of liquid crystals and using finite differences to perform the calculations has been used all along to modelize the behavior of the devices to be realized.

Chapter 4 discusses the calculation models used for the propagation of light in a birefringent media. Jones matrix method is used since it can be proved that the propagation can be considered straight although lateral refractive index gradients exist.

Chapter 5 is entirely dedicated to binary gratings. Those are driven with a single voltage applied to a comb-like electrode. This chapter discusses the limitations in the dimensions that can be resolved through liquid crystal devices.

Chapter 6 continues with blazed gratings. These devices can be freely reconfigured, changing either the periodicity, i.e. number of electrodes per period, or the modulation depth. In addition, the possibility to extend the same designs to lenses or three-dimensional modulation devices is discussed.

[1]LCDMaster is trademark of Shintech Ltd. Japan

Chapter 1

Properties of liquid crystals

1.1 Introduction

If something makes the liquid crystals so interesting, it is the very special properties. Few substances have such a combination of properties, and of such importance. Extremely thin layers, in the μm range, can perform phase retardation of one wavelength and more. The molecules can be reoriented and moved like in a liquid but still torque and shear constraints take place, like in a solid. The arrangement can be altered by external, low intensity forces, like those resulting from magnetic or electric fields. Electric voltages in the range of 1 volt are sufficient, while electro-optic modulators are several mm thick and require kilovolt stimulation.

In this chapter, a brief review of the liquid crystal state of matter and the properties of nematic liquid crystals will be presented.

1.2 Liquid crystals: phases and configurations

As the name clearly indicates, liquid crystals are compounds which show properties that are assigned to the crystalline state of the matter, as well as properties corresponding to the liquid state of the matter. This is not common in traditional materials, in which transition from solid to liquid is clearly defined. Those compounds are indeed not classical, but a result of the organic chemistry and the aromatic groups. They do not show a steep transition from the solid to the liquid state, but intermediate phases. These mesomorphic (= intermediate) phases show the very special properties liquid crystals are known for.

Liquid crystals are considered liquid, because the molecules can move and reorient themselves within a confined space by means of external forces, for example. The specific shapes of

the liquid crystal molecules results in a anisotropic viscous behavior.

Liquid crystals are considerod crystal-like because they show some degree of regular arrangement. This order is not as rigorous and long range as the one in crystals, in the sense that there is not a regular lattice defined. The different liquid crystal phases have different types and degrees of order. Nematic liquid crystals have an orientational order, while they do not have positional order. Smectics have a positional order, but restricted to layers. These are the main phases, but other mesomorphic phases exist. Figure 1.1 shows a schematic view of the phases depending on temperature for the commonly used thermo-tropic liquid crystals. While increasing the temperature, the initially crystalline phase with long range order and static molecules, looses its rigid structure. First the molecules gain some rotational mobility, then the long range order is lost and only a layered arrangement is maintained. Finally, and just before the isotropic state, the nematic phase has only an average orientational order.

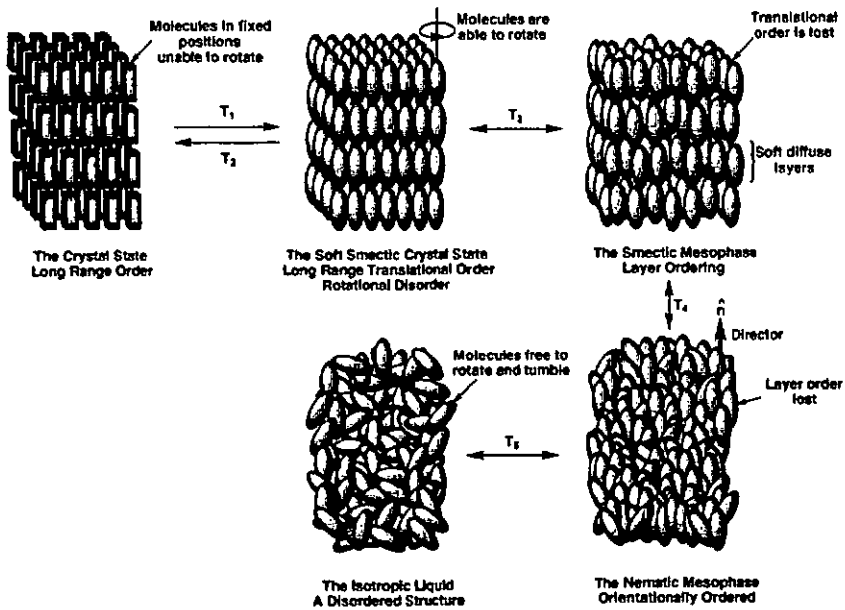

Figure 1.1: *Positional and orientational order in nematic and smectic phases.* [1]

Liquid crystal molecules have also specific shapes. The most common is the cigar or rod-like (calamitic) molecule, represented like a cigar in Fig. 1.2, with the long axis as symmetry axis.

But the molecules are not rigid, and therefore the resulting macroscopic properties are averaged values. They result in uniaxial characteristics, i.e. $\varepsilon_\perp$ and $\varepsilon_\parallel$ for the dielectric anisotropy, or n_e and n_o for the optical anisotropy.

1.3 Properties of the nematic liquid crystals

The most commonly used phase of liquid crystals for applications is the nematic phase. As shown in Fig. 1.2, there is no short range positional nor orientational order of the calamitic (cigar-like) molecules. Nevertheless, a long-range orientational order exists, which is represented by an unitary vector n, called director, also shown in Fig. 1.2. The orientation of the director is an average of the orientation of the molecules. For simplicity, the director is used as a macroscopic reference for the molecules. The anisotropic properties of the molecules are referred to the director, typically as parallel or perpendicular to it.

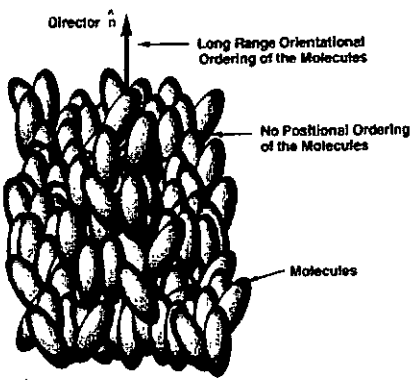

Figure 1.2: *Nematic phase. The orientation of the calamitic-shaped molecules is represented by the director* n. [1]

1.3.1 Elastic properties

As mentioned before, the liquid crystal is viscous and therefore sensitive to torque or sheer. In addition, the specific shape of the molecules makes the behavior of the liquid crystal very sensitive to the direction of the constraint. According to the molecular model established by

Oseen and reviewed by several authors, the general expression of the elastic free energy density is [2]

$$f_e = K_1 \cdot (\nabla \cdot \mathbf{n}) - K_2 \cdot (\mathbf{n} \cdot \nabla \times \mathbf{n})$$

$$+\frac{1}{2}K_{11} \cdot (\nabla \cdot \mathbf{n})^2 + \frac{1}{2}K_{22} \cdot [\mathbf{n} \cdot (\nabla \cdot \mathbf{n})]^2 + \frac{1}{2}K_{33} \cdot [\mathbf{n} \times (\nabla \times \mathbf{n})]$$

$$-K_{12} \cdot [\mathbf{n} \cdot (\nabla \times \mathbf{n})] \cdot (\nabla \cdot \mathbf{n}) - \frac{1}{2}(K_{22} - K_{24}) \cdot \nabla \cdot [\mathbf{n} \times \nabla \times \mathbf{n} + \mathbf{n} \cdot (\nabla \cdot \mathbf{n})]$$

$$+K_{13} \cdot \nabla \cdot [\mathbf{n} \cdot (\nabla \cdot \mathbf{n})] - K_{23} \cdot \nabla \cdot \{\mathbf{n} \cdot [\mathbf{n} \cdot (\nabla \cdot \mathbf{n})]\}, \qquad (1.1)$$

where ∇ is the Nabla vector, n the director and the different K_i and K_{nn} the elastic constants. The constants noted K_{nn} have the dimension of a force [N] except the K_i type like K_1 and K_2 which have the dimension [N/m] of a force per unit length, since they are related to the surface and not the volume. Equation (1.1) is the general formulation for liquid crystals, which does not yet take the specific properties of the nematics into account. Non-polarity, enantiomorphism or symmetry considerations reduce the number of the elastic constants involved. Also, several of the constants are surface-related and do not concern the elastic energy of the bulk. As a result of these considerations, the final result for the nematic elastic energy density of the bulk becomes [2]

$$f = \frac{1}{2}\left\{K_{11} \cdot (div\,\mathbf{n})^2 + K_{22} \cdot [\mathbf{n} \cdot (\mathbf{rot}\,\mathbf{n}) + q_0]^2 + K_{33} \cdot [\mathbf{n} \times (\mathbf{rot}\,\mathbf{n})]^2\right\}, \qquad (1.2)$$

where $q_0 = -K_2/K_{22}$ is the pitch (length required for an helix to turn 360^o) of the cholesteric configuration, which result when chiral dopants are added to the nematic liquid crystal.

1.3.2 Dielectric properties

The electro-chemical bounding of two different atoms results in a electric dipole, due to the different electro-negativity of the atoms. A complex molecule, such as the ones that become mesogens, can be regarded as a system of dipoles, with a global dipole resulting from the contributions of the discrete dipoles. Also, complex molecules do not have a rigid structure and their configuration can change in time, resulting in a rearrangement of the dipoles and the resulting

global dipole. The dielectric properties of the media results from an average of these properties.

The effect of re-orientation by means of an external electric field in the nematic liquid crystal molecules is the result of the dielectric anisotropy of the material. The electric energy density f_E of the media resulting from the interaction of the electric field vector $\mathbf{E}$ and the dielectric tensor ε, is given by

$$f_E = \mathbf{D} \cdot \mathbf{E} = (\varepsilon \cdot \mathbf{E}) \cdot \mathbf{E}, \tag{1.3}$$

where $\mathbf{D}$ is the electric displacement. The calamitic shape of the molecules reduces the dielectric tensor to

$$\begin{bmatrix} \varepsilon_\perp & 0 & 0 \\ 0 & \varepsilon_\perp & 0 \\ 0 & 0 & \varepsilon_\parallel \end{bmatrix} \tag{1.4}$$

with $\varepsilon_\parallel$ and $\varepsilon_\perp$ the parallel and perpendicular components with respect to the director $\mathbf{n}$. Finally, the dielectric anisotropy is obtained by the difference

$$\Delta\varepsilon = \varepsilon_\parallel - \varepsilon_\perp. \tag{1.5}$$

This value is usually positive for calamitic liquid crystals, $\Delta\varepsilon > 0$, which result in an alignment of the director $\mathbf{n}$ (long axis) parallel to the applied electric field $\mathbf{E}$. Perpendicular alignment to the electric field occurs for negative anisotropy, which is the case for molecules with strong lateral dipole moments.

The dielectric anisotropy changes with the frequency of the electric signal. For static or quasi-static fields they have constant values, but with increasing frequency the values of the dielectric constants drop in certain frequency ranges. It is also possible that the sign of the anisotropy changes, as shown in Fig. 1.3.

1.3.3 Optical properties

The propagation of light is modified by the properties of media. An electro-magnetic wave is slowed down by the media, compared with the same wave propagating in vacuum. The wave equation

$$\nabla^2\mathbf{E} - \mu \cdot \mu_0 \cdot \varepsilon \cdot \varepsilon_0 \cdot \frac{\partial^2\mathbf{E}}{\partial t^2} = 0 \tag{1.6}$$

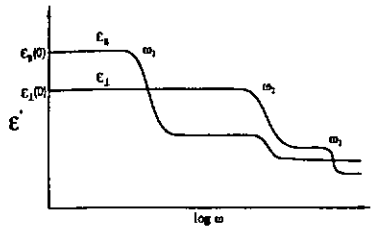

Figure 1.3: *Schematic frequency response of the dielectric constants $\varepsilon_{\parallel}$ and $\varepsilon_{\perp}$, parallel and perpendicular with respect to the director* n. *For static and quasi-static electric signals, the anisotropy is maintained, but sign reversal can occur for higher frequencies.*

in an anisotropic medium has plane wave as solutions with the phase velocity

$$v_p = c/n = \sqrt{\frac{\mu_0 \cdot \varepsilon_0}{\mu \cdot \varepsilon}}, \tag{1.7}$$

where $c = \sqrt{\mu_0 \cdot \varepsilon_0}$ is the speed of light in vacuum and $n = \sqrt{\mu \cdot \varepsilon}$ is the index of refraction of the medium. With the assumption $\mu = 1$ for non-magnetic media, the refractive index is in fact the square root of the dielectric permeability ε at the frequency of the electromagnetic wave.

In a anisotropic media, the situation changes. The medium is not defined by a single scalar dielectric constant, but by a tensor, which can be represented in diagonal form

$$\varepsilon = \begin{bmatrix} \varepsilon_1 & 0 & 0 \\ 0 & \varepsilon_2 & 0 \\ 0 & 0 & \varepsilon_3 \end{bmatrix}. \tag{1.8}$$

The corresponding quadratic form in space can be rewritten as

$$\varepsilon_1 \cdot x^2 + \varepsilon_2 \cdot y^2 + \varepsilon_3 \cdot z^2 = \frac{x^2}{n_1^2} + \frac{y^2}{n_2^2} + \frac{z^2}{n_3^2} = 1. \tag{1.9}$$

which is known as the index ellipsoid with the major axes n_1, n_2 and n_3. Calamitic liquid crystals have one axis of rotational symmetry and are thus in the category of uniaxial optical birefringence. The corresponding index ellipsoid is also of rotational symmetry with the mayor axis $n_1 = n_2 = n_o$ and $n_3 = n_e$, where n_o and n_e are known as the ordinary and extraordinary index of refraction. For any given wave-vector k, one finds two plane wave solutions, with orthogonal linear polarizations, which propagate with different phase velocities. The corresponding index

of refraction are n_o for the ordinary polarization and

$$n_{eff}(\theta) = \frac{n_o \cdot n_e}{\sqrt{n_o^2 \cdot \cos(\theta)^2 + n_e^2 \cdot \sin(\theta)^2}} \tag{1.10}$$

for the extraordinary polarization, where θ is the angle between the wave-vector k and the optical axis z. Figure 1.4 shows the ellipsoid and the wave vector together with the solutions for both waves (D).

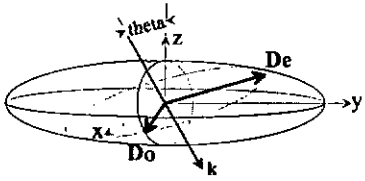

Figure 1.4: *Index ellipsoid for uniaxial birefringent media.* k *is the wave-vector,* z *is the optical axis and* D_o *and* D_e *are the electric displacement vectors for the two eigen-polarizations. In the case of nematic liquid crystals, the optical axis* z *is parallel to the director* n.

The accumulated phase difference $\Delta\varphi$ through a liquid crystal becomes then

$$\Delta\varphi = k \cdot d \cdot n_{eff} - k \cdot d \cdot n_o = k \cdot d \cdot \Delta n, \tag{1.11}$$

where $k = 2\pi/\lambda$ is the wavenumber, d the thickness of the liquid crystal and $\Delta n = n_{eff} - n_o$ the birefringence. The phase retardation $\Delta\varphi$ is the main optical value to be considered in liquid crystal devices.

Wavelength dependence of the refractive index (dispersion)

The refractive index dispersion model is derived from quantum mechanical theory, and concerns the molecular polarizability at the considered wavelengths. According to Wu [3, 4], the polarizability of nematics is related to the oscillator strength relative to the main axes. The single band model results in

$$n = G \cdot \frac{\lambda^2 \cdot \lambda_0^2}{\lambda^2 - \lambda_0^2}, \tag{1.12}$$

where G represents different molecular properties (density, oscillator strength...) at the mean resonance wavelength λ_0. Both constants (G and λ_0) are calculated from empirical values of n. Since λ_0 is usually in the UV, Eq. (1.12) can be simplified to the Cauchy formula (1.13) for

visible wavelengths ($\lambda > \lambda_0$),

$$n = G \cdot \lambda_0^2 \cdot \left[1 + \left(\frac{\lambda_0}{\lambda}\right)^2 + \left(\frac{\lambda_0}{\lambda}\right)^4 + \ldots\right] = A + \frac{B}{\lambda^2} + \frac{C}{\lambda^4} + \ldots . \tag{1.13}$$

Equation (1.12) is not valid in the vicinity of the molecular vibrational bands, but these occur for wavelengths longer than 3 μm typically [3].

The index for the common IR wavelengths used in fiber optic applications, 800 nm, 1300nm and 1550 nm, can be extrapolated after measurements done in the visible spectrum, needed to determine the three coefficients A, B and C for the ordinary and extraordinary index. This is valid as long as the wavelength are not close to resonance frequencies. In Fig. 1.5a the resulting dispersions of the ordinary and extraordinary refractive index of a nematic liquid crystal (BL006 by Merck) are shown. Figure 1.5b shows the resulting birefringence

$$\Delta n\,(\lambda) = n_e\,(\lambda) - n_o\,(\lambda)\,. \tag{1.14}$$

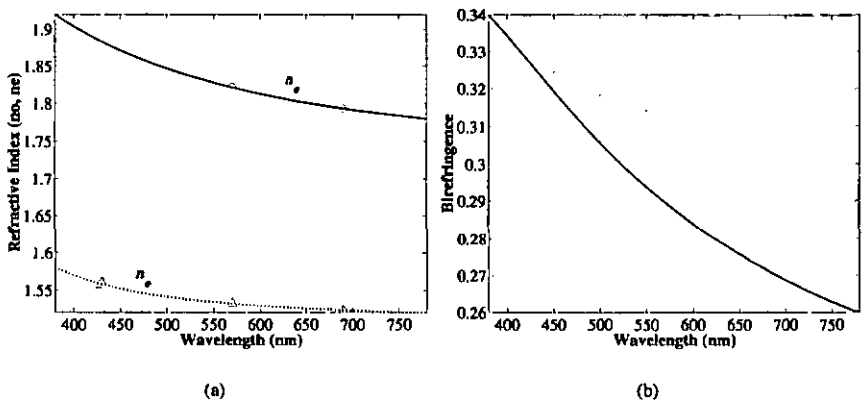

Figure 1.5: *Dispersion af BL006 (Merck) using Eq. (1.13) from 3 measured values. a) refractive index, b) resulting birefringence.*

The current applications of liquid crystals such as displays, are not monochromatic but cover the whole visible spectra. The optical function of such devices require typically a specific phase retardation calculated from Eq. (1.11). But the optimization is only possible for one wavelength, since the phase shift for the visible wavelengths is not constant but follows the dispersion relation

$$\frac{\partial \varphi}{\partial \lambda} \simeq \frac{\partial}{\partial \lambda}\left(2\pi \cdot d \cdot \frac{B}{\lambda^3}\right) \sim \frac{1}{\lambda^4}. \tag{1.15}$$

This means that the variation on the retardation is more important for longer wavelengths. Optimizing a LC display requires correction of this dispersion using birefringent foils, double cells and other techniques.

Another aspect to consider is the temperature sensitivity of the refractive indices. Figure 1.6 shows the decay of the birefringence with increasing temperature. This will in turn strongly change the performance of the device that will not be optimal anymore. Note that the birefringence is zero when the temperature reaches the point of the nematic to isotropic phase transformation.

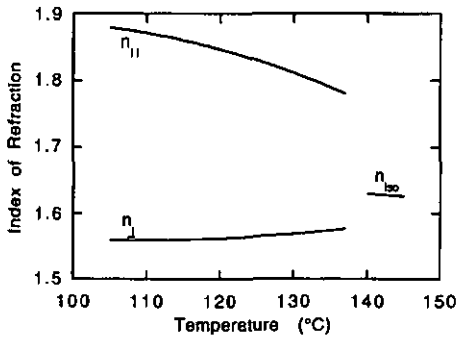

Figure 1.6: *Temperature dependence of the refractive indices.*

Summary

Three fundamental properties are of importance for the realization of liquid crystal devices:

1. *Visco-elastic behavior.* By means of the three main elastic constants (K_{11} K_{22} K_{33}), the liquid crystal can recover from an externally induced stress to an original equilibrium arrangement. The elastic free energy that allows this recovering is calculated after

$$f = \frac{1}{2}\left\{K_{11} \cdot (div\,\mathbf{n})^2 + K_{22} \cdot [\mathbf{n} \cdot (\mathrm{rot}\,\mathbf{n}) + q_0]^2 + K_{33} \cdot [\mathbf{n} \times (\mathrm{rot}\,\mathbf{n})]^2\right\}.$$

2. *Dielectric anisotropy.* This macroscopic property allows to rearrange the molecules by means of an external electric field. The electric free energy is calculated after

$$f_E = \mathbf{D} \cdot \mathbf{E} = (\varepsilon \cdot \mathbf{E}) \cdot \mathbf{E},$$

with the tensor ε and the resulting anisotropy $\Delta\varepsilon = \varepsilon_{\parallel} - \varepsilon_{\perp}$.

3. *Birefringence.* The polarization of light is modified by the refractive index anisotropy $\Delta n = n_{eff} - n_o$, where the effective extraordinary index

$$n_{eff}(\theta) = \frac{n_o \cdot n_e}{\sqrt{n_o^2 \cdot \sin(\theta)^2 + n_e^2 \cdot \cos(\theta)^2}}$$

depends on the orientation of the liquid crystal respectively to the wave vector

4. *Index dispersion.* The refractive index is related to the wavelength and the dispersion can often (not in the vicinity of resonance frequencies) be approximated by the Cauchy formula

$$n_{o,e} \simeq A_{o,e} + \frac{B_{o,e}}{\lambda^2} + \dots .$$

Chapter 2

Technological improvements for liquid crystal devices

2.1 Introduction

In this chapter, technological improvements developed for liquid crystal display (LCD) applications are presented. Current LCD's are based on nematic liquid crystals with different configurations depending on the properties desired for the device. Figure 2.1 shows the different components of a generic twisted nematic device. The nematic liquid crystal layer is sandwiched between two glass substrates with a thin transparent and conductive layer of Indium-Tin-Oxide (ITO). This layer will serve as electrodes after being structured to the desired pattern. The layer is covered with a protective SiO_2 layer and over this layer, a layer of polyimide is spin-coated. The polyimide layer is rubbed with a velour roll in a specific direction so that the liquid crystal molecules are strongly anchored along this direction. The layers in the upper and lower substrate are rubbed in different directions to obtain an angle, between these two directions, below 90^o in the case of the twisted nematic (TN) devices or in a range between 180^o and 270^o for super-twisted nematic (STN) devices. Between the two orientations of the molecules determined by the rubbing of the polyimide layer, the nematic molecules arrange themselves to form a helix, structure which minimizes the elastic energy of the system. The pitch of the helix is, in the case of STN devices, determined with a chiral dopant together with the alignment directions. The last element in the cell is the spacer. The optical function is directly related to the thickness and therefore small spherical spacers are randomly distributed between both substrates. The atmospheric pressure and an adhesive frame in the borders of the cell maintains the elements together at the thickness of the spacers.

The improvements made concern the fabrication as well as the optical performance of liquid crystal devices. High resolution structures, with a geometrical size similar to the size of the spacers, are perturbed by the presence of these spacers within the active zone. A new technology has been developed to define the thickness and reduce the variations over the whole area. Also mechanical stability has been improved.

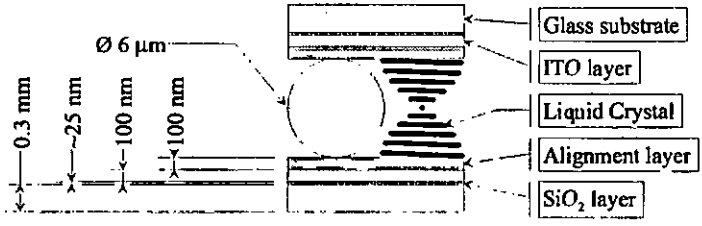

Figure 2.1: *Layers composing a liquid crystal device.*

2.2 Fabrication of liquid crystal devices

In this section, the fundamental components and steps in the fabrication of a liquid crystal device are reviewed. As explained in the introduction and with Fig. 2.1, the devices are mainly a stack of different layers with different function each. The classical techniques are presented together with the improvements made for specific applications.

2.2.1 Glass substrates and conductive layer

The first element of the stack represented in Fig. 2.1 is the substrate. High quality glass is used, covered with a conductive and transparent or reflective layer. The glass substrate is several hundreds of micrometers thick, and the conductive layer typically 25 nm thick for a resistivity of $50\,\Omega/square$. This layer is usually already deposited by the glass supplier, reaching high uniformity and accuracy in both electric and transmissive properties. The conductive layer is made of a Indium Tin Oxide (ITO). The oxygen content is very important for both the conductivity (higher for lower concentration) and the transmission (higher for higher concentration). Between this conductive layer and the glass substrate, a SiO_2 layer is present for protection purposes. The refractive index of the ITO layer has a value around 1.7 but is variable, depending on the final composition of the ITO layer.

The electrodes or segments are etched into this layer using photolithographic processes. The conductive layer is covered with photo-resist which will be structured with the desired pattern. The ITO will then be etched either in an acid bath or in a plasma chamber, depending on the feature size of the pattern. In the μm range, plasma etch is preferred, because of its controlled directionality, although the photo-resist must be thick enough to support the attack. For feature sizes larger than 10 μm, wet etch is preferred, even if the acid attacks also the ITO under the photo-resist mask.

The glass thickness, and thus its weight, is preferred to be as small as possible. Thin glass plates are highly deformable. This causes the device to be mechanically unstable, with locally varying thickness and sensitivity to external stresses, resulting in reduced optical performance. A typical thickness for small displays is 0.3 mm.

2.2.2 Alignment layer

The alignment layer is a component with several functions in the device.

1. As thin dielectric layer, it isolates the molecules from the structured electrode. The edges of the electrodes create very strong electric fields locally, that can result in electro-chemical decomposition of the molecules. The thin layer smoothes the electric field and reduces the effect of fringing fields.

2. As alignment layer, it assures the anchoring of the molecules at the interface. This anchoring determines the orientation (azimuth angle) and the inclination (polar angle) of the molecules at the boundaries. This will determine the relaxed configuration of the liquid crystal together with the characteristics of the specific phase or configuration (nematic, twisted-nematic, smectic).

Several alignment techniques and materials are available. The easiest way is not to use any additional layer and to rub directly the glass substrate. This is clearly the less secure method, very sensitive to any irregularity and not reliable in the long term. Another method used before the appearance of polyimides, is the oblique evaporation of SiO [5]. The pre-tilt angle is then fixed controlling the incidence angle of the substrate relatively to the source.

Nowadays, the common technique is to use polyimide layers. They are very reliable and easy to integrate into clean room processes. The polyimide is typically spin-coated or printed, depending on the thickness, over the desired surface and a thermal polymerization cycle follows.

Finally, the substrate is mechanically rubbed with velour to determine the direction of the alignment, as illustrated in Fig. 2.2. The pre-tilt angle is mainly fixed by the material itself, but some adjusting, specially through rubbing speed, is possible during the process.

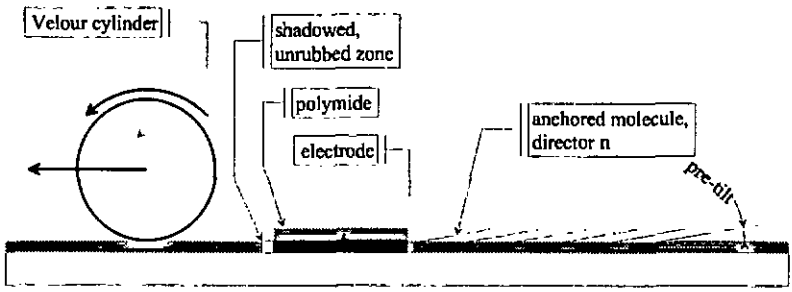

Figure 2.2: *Alignment sense and direction determination by means of mechanical rubbing of the alignment layer. The pre-tilt angle depends on the polymer, but also on the rubbing process (sense, speed).*

New photo-sensitive polyimides are used to determine the alignment direction and pre-tilt angle. Mechanical rubbing is source of defects, like the white lines that appear along the electrodes shown in Fig. 2.5a, due to the shadowing effect in the presence of large polyimide steps illustrated in Fig. 2.2 or to dirt from the velour roll or other sources. In the case of photo-sensitive polyimides, the alignment is a result of molecular re-arrangement in the polymer layer by linearly polarized UV exposure. The pre-tilt angle is then determined by the angle of incidence of the UV light. The main interest of this technology [6, 7], together with the cleanness, is the possibility to create patterns of different alignment over a single substrate, making several exposures through different masks. For example, a pixel of a twisted nematic (TN) display can be divided in 4 sub-pixels with different alignment directions, and the angular dependence is highly improved [8]. This was already done with classical polyimides, but it required to cover the polyimide with photo-resist, structure it, rub and remove the photo-resist for each new desired rubbing direction [9, 10]. And finally, micro-grooves can be engraved into the polyimide using laser or e-beam [11].

Pre-tilt angle

The pre-tilt angle is the angle between the substrate and the director of the anchored molecule, as shown in Fig. 2.2. For planar alignment, the values are typically between 1^{o} and 15^{o}, depending on the application and the structure desired. Nematic (N) and twisted-nematic (TN) devices

usually require low pre-tilt values, which give steeper response to the external electric fields. Figure 2.3 is a simulation of the electro-optical response depending on the pre-tilt angle. The director in the central layer (d/2) has a steeper response at the threshold voltage for very low pre-tilt values. This threshold is not clearly defined in the case of large pre-tilt values (dotted lines). *Super-twisted-nematic devices, which already have a steep response to the electric fields* through the strong twist, require larger pre-tilt angles for larger twist, essentially to maintain the desired twisted configuration.

The interest of a non-zero pre-tilt angle comes from the fact that it renders the system asymmetric for twisted structures. In a twisted-nematic cell, with a pre-tilt angle of 0°, the twist could be clockwise or counterclockwise. With the presence of a pre-tilt angle, there is a sense of rotation with less energy than for the other.

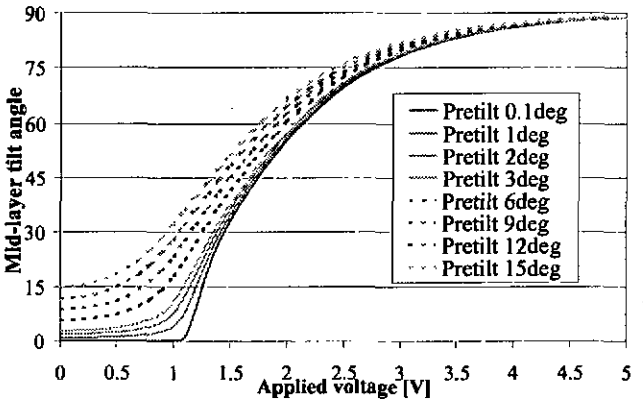

Figure 2.3: *Influence of the pre-tilt angle in the nematic arrangement. The liquid crystal response (for N and TN) is steeper when the pre-tilt angle is very small, which results in a well-defined threshold voltage.*

2.2.3 Assembling

Two substrates, each one with a specific electrode pattern, are assembled face to face. To keep a fixed distance between these substrates, calibrated spacers are used. Those are either spheres or cylinders, and are randomly spread over the surface. Thank to the refractive index difference between ITO and glass, the structured patterns of the ITO layer are recognizable and used as

alignment marks for the top and bottom substrate. Finally, both substrates are glued together leaving a small aperture for vacuum filling.

The presence of the spaeers reduces the optical performance of the liquid crystal device [12]. It is possible to solve this problem for some applications using thick glass, several mm thick, and placing the spacers only at the corners of the substrate, outside the active zone. Another approach is to strategically place the spacers in zones where it does not change the optical function, for example between two pixels, as shown in Fig. 2.4. This can be done in reflective, active devices as part of the transistor fabrication in the Si substrate.

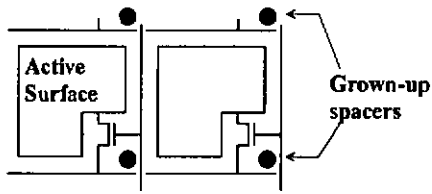

Figure 2.4: *Strategic placement of spacers. Reflective-Active-Matrix displays in Si-technology use grown columns of Si as spacers.*

2.2.4 Filllng

Filling with nematics can easily be performed by capillar attraction, because the typical thickness of the devices are in the 5 to 10 μm range. This technique is not very reliable, compared with vacuum filling. Vacuum filling has the major advantage to remove the air solved in the liquid crystal. Air bubbles in the device are sources of disclinations and optically inactive spots within the active zone. After filling, the cell must be sealed. But as a result of the elasticity of glass and the glue put only at the border of the glass plate, the cell is over-filled and must be flattened by removing the excess of liquid crystal. When finally sealed, the external pressure assures the contact of both substrates with the spacers.

The cholesteric texture is very viscous, and common vacuum filling requires a long time to complete. Higher vacuum is not recommended, since some components of the LC mixture could evaporate. Higher temperature might be a solution, but it must not be forgotten that the cell must be heated too by contact, since it is in vacuum, otherwise the cold cell makes the heating of the LC useless. The temperature is also limited by the evaporation of the components in the LC mixture. Finally, the process can be accelerated by combining vacuum followed by high pressure.

2.3 Thickness control

The performances of a liquid crystal devices are directly related to the thickness. Not only the optical retardation is directly related ($k \cdot d \cdot \Delta n$), but also the switching is related to the thickness ($\tau \propto d^2$). Thus the control and the uniformity of the cell thickness are of great importance. The usual technology uses spherical or cylindrical spacers distributed randomly over the hole area to keep the thickness constant. This makes the thickness to about $0.1\,\mu m$ accurate. But the presence of the spacers disturbs the optical function of the liquid crystal. Not only the device is optically inactive at this point, but also the surrounding liquid crystal structure is perturbed, which results in reduced efficiency [12]. In the case of fine gratings, the spacers are of the same size as the structures. Figure 2.5a shows both the shadowing effect on rubbing discussed before, which appears as white lines. Also, the spacers become transmissive spots. In Fig. 2.5b, the electrodes are grouped in number of three and 4 different voltages are applied (12 electrodes per period). The spacers are also a source of disclinations, as it can clearly be seen in Fig. 2.5b. This cell is also excessively filled, which means that the spacers are not in contact with both substrates and can move within the cell through the flow of the liquid crystal. The figure shows how the spacers have been grouped into lines through repetitive switching on and off.

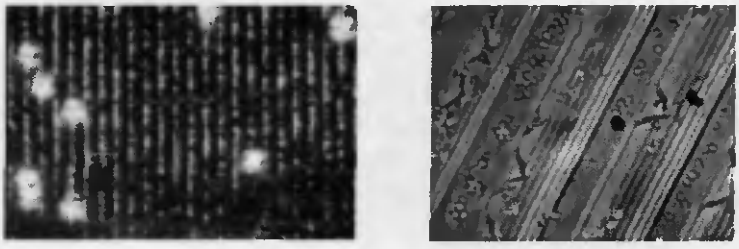

(a) (b)

Figure 2.5: *High frequency gratings with spacers of similar size. a) Under crossed polarizers, the image should be black, but the spacers and the bad alignment in the borders of the electrodes become transmission spots. b) The spacers can cause disclinations to appear. The bad thickness control allows flow of the spacers that are grouped. In these pictures, the spacer density is excessive.*

It would be of great interest to remove the spacers from the active zone. This is possible when this zone is very small or when thick glass is used [13]. Obviously, this is not the case for flat panel displays, but is the best approach for prototyping.

2.3.1 Photo-resist spacers and ribs

A first possibility to overcome the problem of the presence of spacers in the active zone is to use photo-resist to fabricate discrete spacers on the substrate, following the principle shown in Fig. 2.4. The advantage of doing so is the control over the distribution and density of the spacers, minimizing the perturbing effects on the liquid crystal phase. In order to minimize the effect of the presence of spacers in the active zone, a regular pattern of polymer columns can be fabricated using photo-resist and a mask with the required pattern. To make it simple, this columns are not aligned with the electrode pattern, but this is uncritical in low resolution devices. The size and density of the dots in the mask is related to the pressure the cell must support, but clearly below the classical random spread spheres. Experience has shown that the density can be quite low (diameter = 20 μm, period = 10 mm) and thus the effect on the optical function is strongly reduced. Additionally, the photo-resist adheres to both substrates improving the mechanical reliability and the thickness control. The cell cannot inflate when filled through vacuum technique, as discussed before.

A second use of this technology has been investigated. Together with the spacer function, the photo-resist can also serve as a barrier. Using specific designs, it is possible to reserve different zones for different liquid crystals within the same plane. The advantage of this process is multiple. First the spacers are out of the active zone and do not perturb the optical functionality of the liquid crystal. Second, the mechanical rigidity of the whole cell is improved and the device is less sensitive to external stresses. This is very important for other liquid crystal textures, such as the cholesteric texture [14] or ferroelectric liquid crystals [15, 16]. Finally, the use of different liquid crystals can solve some of the negative aspects of the liquid crystals, such as angular dependence. Also different functions could be implemented within the same plane, for example, different colors. This example is discussed later.

Self-Allgnment [1]

The use of an additional mask for the creation of the spacers is usually not welcome in production lines, because it adds an additional step. In addition, the alignment of the mask with the existing pattern is critical. Thus, methods of self-alignment are desired for any photolithographic processes.

The principle of self alignment is simple. The idea is to use the structures of a previous step of the fabrication cycle as mask for the following step. Figure 2.6 shows an example of

[1]For this technology, patents are pending in favor of ASULAB S. A.

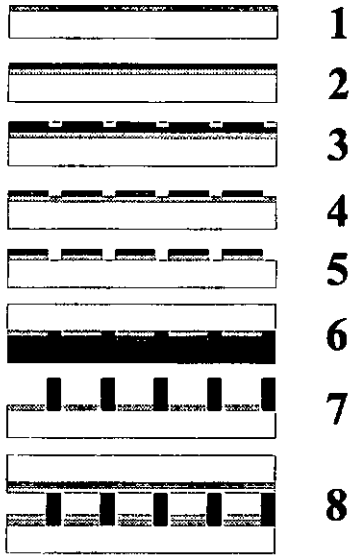

Figure 2.6: *Self-alignment procedure.*

self-alignment used for liquid crystal arrays. The process is as follows:

1. Positive photo-resist is spin-coated over the ITO surface of the substrate.
2. The electrode pattern mask (positive pattern) is used for structuration of the photo-resist by UV-exposure.
3. The exposed photo-resist is removed with the corresponding solvents.
4. The ITO layer is wet-etched.
5. Negative photo-resist is spin-coated over the remaining positive photo-resist.
6. In order to use the positive photo-resist as mask, the substrate is UV-exposed from the opposite face of the substrate.
7. Not exposed negative photo-resist is removed together with the remaining positive photo-resist.
8. After spin-coating the alignment layers, the two substrates are aligned and assembled by heat in vacuum

Using this process, only the negative photo-resist ribs remain exactly between the structured electrodes. The ribs made of negative photo-resist can be higher than the positive photo-resist

layer as presented in Fig. 2.6. The process requires chemical compatibility of the different photo-resists and solvents, which is not obvious. This problem disappears when reflective displays are considered. Beginning with the metallized layer, the process is slightly modified after step 4:

5. The alignment polymer is spin-coated over the etched metallic layer, processed and conveniently rubbed.
6. The negative photo-resist is spin-coated and processed.
7. UV-exposure through the opposite face. The metallic electrodes serve as mask.
8. Removal of the not exposed negative photo-resist.

From the technological point of view, reflective devices have important advantages. First, there is no mix of positive and negative photo-resist. The negative photo-resist required for transmissive cells is not common and requires fine tuning of the UV-exposure time. Second, the alignment layer is spin-coated over a flat surface. For the transmissive cell, it can only be spin-coated after ribs construction. The uniformity of such a layer has been investigated [17] and it appears to be inappropriate. Finally, reflective LC-devices require half the thickness of transmissive devices, thus reducing the switching time τ by a factor of 4 ($\tau \propto d^2$). Nevertheless, the choice of a transmissive or a reflective depends on the application.

The final step for the cell construction is assembling. The counter-electrode substrate is put over the substrate with the ribs. After alignment, the cell is put in a plastic bag which is in turn evacuated, so that the atmospheric pressure assures contact of all the surfaces of the ribs with the other substrate. If the photo-resist of the ribs has not been completely dried during the previous steps, a thermal cycle below the melting temperature [18] can assure an adhesive contact of all the ribs on the second substrate. No further gluing is required. The assembly resists to peeling-off.

One of the drawbacks of this technique is the presence of four boundaries compared to the two boundaries defined by the upper and lower substrate and the rubbed polyimide (see Fig. 2.1). Those boundaries determine the relaxed state of the liquid crystal phase. Now, four boundaries represent a new arrangement. Additionally, the above described process does not determine uniquely a preferential anchoring on the lateral walls generated by the photo-resist ribs.

With the help of LCDMaster, a finite element simulation software that will be presented in the following chapter, it is possible to model the effect of an additional anchoring boundary on the lateral wall. Figure 2.7 shows the possible effect of a lateral boundary in a nematic cell. Without any applied voltage, the planar director distribution is perturbed by the lateral boundary. The width of this altered zone is related to the liquid crystal properties and the thickness of the cell.

Figure 2.8a clearly presents the advantages of solid ribs compared to a free inter-electrode

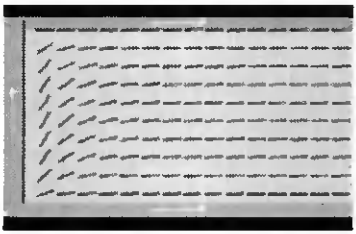

(a)

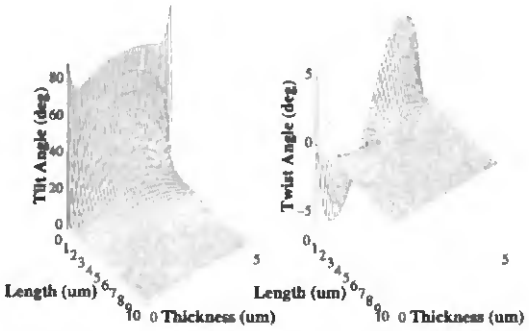

(b)

Figure 2.7: *(a) Model for calculation with additional lateral boundary. (b) Final state of the nematic cell through lateral alignment. (NLC, thickness = 5 μm, length = 10 μm, pre-twist = 0, upper and lower pre-tilt = 2°, lateral pre-tilt = 90°).*

space. Under crossed polarizers, the ribs appear as black horizontal lines in both switched and un-switched states. On the other hand, since the vertical inter-electrode spaces are filled with liquid crystal, they appear white in the homeotropic (vertical) state of the liquid crystal and in an undefined state in the focal-conic state. While the optical effect of the ribs is fixed, the uncontrolled LC has an undefined and therefore variable optical function.

Figure 2.8b shows how the lateral boundaries can perturb the phase arrangement in the case of cholesteric textures. The anchoring at the new boundaries break the cholesteric (helical) texture (Fig. 2.9), although this process is considerably slow. A solution to the texture-destruction is to use polymer-dispersed liquid crystals (PDLC). The polymer is present in very low concentration,

Figure 2.8: *Transmission through crossed polorizers for cholesteric textures in rib-delimited pixels. (a) Homeotropic texture (fully transparent) under applied voltage (U = 50 V). (b) Focal-conic-like texture after switching back to the selective reflection (Fig. 2.10).*

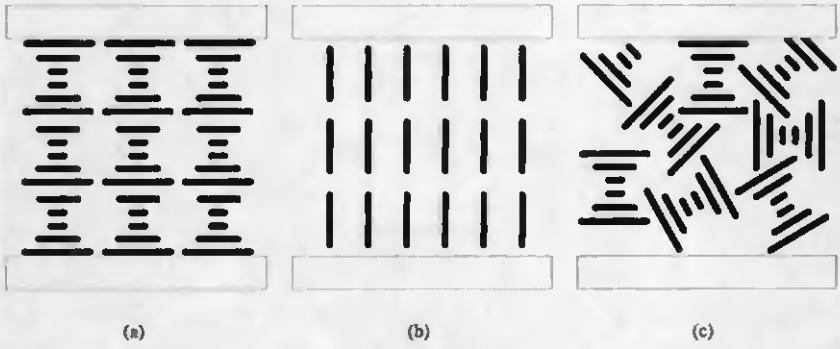

Figure 2.9: *Stable configurations of cholesteric texture used for devices. Before any driving signal is applied, the texture is the one shown in sub-figure (a). The reflection is like the one calculated for Fig. 2.10. Under an applied voltage, far stronger than the usual nematic devices, the liquid crystal is arranged homeotropically and becomes transparent (b). When the signal is removed, it relaxes to a stable state which is not reflective. When switched back, the texture is not recovered as in (a). The cholesteric helix is recovered in different domains, although maintaining its pitch (c). The reflection color is the same but looks diffuse, milky.*

but the web which is formed by polymerization stops the propagation of the perturbation of the lateral boundaries. Additionally, it stabilizes the cholesteric mixture.

An additional particularity of confined CT-structures is that they do not recover the initial configuration, except after being heated and becoming isotropic. The initial configuration is

illustrated in Fig. 2.9a, where the cholesteric helix is complete between the two boundaries. When the switch on signal is applied, the phase first becomes homeotropic and then relaxes to a stable state which is not in the Bragg region. Finally, when switched off, the helical structure is recovered but in a fragmented manner, shown in Fig. 2.9c. The pitch is maintained and thus the reflection window (Fig. (2.10)), but the aspect is more diffuse that the original. This device is bistable, i.e., the two selected states are stable even without any applied field, but both require a specific signal to be changed.

Application: multi-liquid-crystal cells with ribs

An application of the photo-resist ribs is to create different closed zones that can be filled separately with different liquid crystals. In the present example, the goal is to fill the cell with cholesteric liquid crystal. The interest of cholesteric liquid crystals is that they reflect circular polarized light at the wavelength which matches the pitch of the cholesteric structure in the media. An effective cholesteric reflector needs to have a thickness of more than 10 times the pitch of the helix. Higher number of periods improve the selectivity and steepness of the reflective mirror. Practically it can be described as a Bragg reflector.

Figure 2.10 shows the result of a calculation using the 4x4 method implemented in LCDMaster, described in chapter 3. The spectral width of the reflection is delimited by the helical pitch and the ordinary and extra-ordinary refractive index, i.e.

$$pitch \cdot n_o \leq \lambda \leq pitch \cdot n_e. \tag{2.1}$$

Combining different liquid crystals with different chirality, it is possible to adjust the central wavelength and the width of the reflection window. This solution would be more efficient and simple to fabricate than the usual grey-level switch with additional color filter. Combining the color capabilities of cholesterics with the ribs technology, it is possible to combine the primary colors in a single layer. Figure 2.11 shows a basic concept for a bicolor liquid crystal cell. Two isolated zones are created by the photo-resist ribs. Each one can be filled with different liquid crystals for the different colors.

Another interesting aspect of the ribs technology applied to the cholesteric texture is the mechanical stability. The different configuration in a cholesteric switch are extremely sensitive to external stress. In fact, some configurations simply disappear when the display is pressed. The interest of the ribs comes from its resistance to external stress. Each column is physically isolated from the neighbors and, even if one column of cholesteric may loose its configuration, there is no

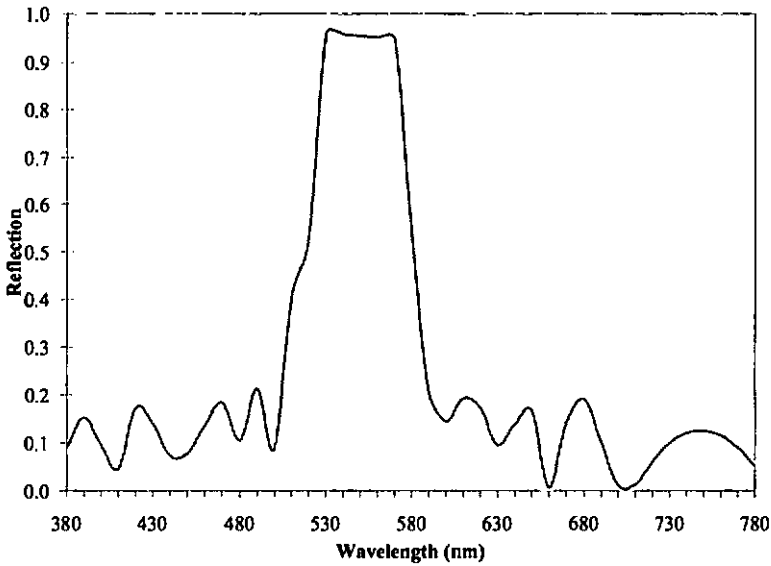

Figure 2.10: *Reflection of a cholesteric structure. (LC: ZLI-2293, pitch = 350 nm, thickness =* $3.5\,\mu m$, $\lambda_o = 550\,nm$, $n_e = 1.64$, $n_o = 1.50$.

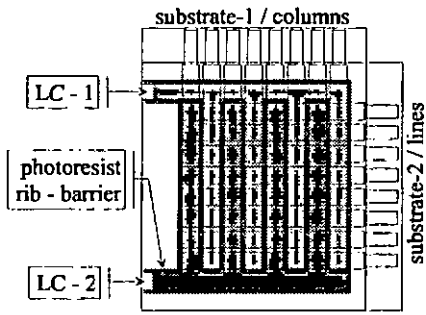

Figure 2.11: *Bi-color liquid crystal cell. The photo-resist ribs serve both as spacer and as barrier between the two liquid crystals.*

propagation of this destruction. Additionally, each column of LC being very thin, the required force is much higher than for a display using classical technology. Finally, the cholesteric switch

is bistable, i. e. once one state has been selected, the driving signal can be removed and the state is maintained. This is interesting, since it does not require constant refreshing of the display pattern.

2.4 Summary

The technological improvements realized, which lead also to patent publications, are the following:

1. *The randomly distributed spacers have been removed.* As a result, the liquid crystal phase is not perturbed in the active zone and the predefined operating configuration, such as twisted or super-twisted nematic, is obtained. The whole active area is thus functional. Therefore, the optical performance are only limited by the configuration itself.

2. *The thickness is controlled by a photo-resist structure.* The spacers have been replaced by photo-resist which is placed in the dead space of the electrodes. The active area is free of any other element than the liquid crystal. Nevertheless, the presence of a new boundary, the photo-resist wall, has an effect on the configuration of the liquid crystal along this boundary.

3. *Resistance to external stress has been increased.* The area occupied by the photo-resist structure is much more important than the one covered by the spacers. The resistance to external stress is enforced. In addition, the presence of walls also reduce the possibility of flow of the liquid crystal when the device is pressed. This is of great interest for cholesteric or ferroelectric devices, which depend on the structure of the liquid crystal in the device.

4. *Polymer-stabilized cholesteric mixtures have been developed.* The adjunction of a small quantity of polymer has two main positive effects. First, the mixture is more stable. Second, the presence of the polymerized web reduces the disturbing effect of the photo-resist walls.

5. *Different isolated domains are available.* They allow the use of different liquid crystals in the same layer.

Chapter 3

Reorientation of nematics under external fields

3.1 Introduction

A liquid crystal display is from the physical point of view a quite complex system. Several specific properties are involved in the description of the interaction between the liquid crystal and the external elements. Those are, apart from the liquid crystal itself: a) the physical boundaries, that determine the relaxed state of the liquid crystal, b) the external electric or magnetic field, which modifies the spatial orientation of the molecules by interaction with the anisotropic properties of the liquid crystal, and c) the birefringence, which is modulated by the spatial orientation of the molecules and changes the polarization of the transmitted light.

A macroscopic model is proposed, that describes the energy density of the liquid crystal bulk. An equilibrium of three forces, originated by the elastic properties of the liquid crystal, the electric or magnetic energy from the interaction of the LC with an external field, and the specific conditions imposed by the boundaries, is obtained when the total energy density is minimized. The bulk energy is calculated after the Frank-Oseen model, which is a vectorial model. Other approaches are possible, such as the Monte-Carlo algorithm [19] or the Q-tensor representation [20, 21].

This chapter introduces a macroscopic model for liquid crystals and for the calculation of externally distorted distributions of the nematic liquid crystal. Some special cases, which allow analytic solutions, will be presented. Finally, the LCDMaster [22] implementation, using a finite element approach, is described.

3.2 Description of the device

Except for hybrid constructions, i.e. micro-structures and liquid crystal [23, 24, 25] and the more complex structure of polymer-dispersed liquid crystals [26, 27, 28, 29], liquid crystal devices can be described by the simple arrangement shown in Fig. 3.1. Glass substrates with a thin conductive layer of Indium and Tin Oxide (ITO) are covered with a polymer layer that is mechanically rubbed. The liquid crystal is confined between two of these substrates and oriented by the boundaries along the rubbing direction. Additionally, the spacing between the two substrates is kept constant with spacer balls or fibers of defined diameter. Practically, the device model is simplified as follows. The glass substrate is ignored, since it does not medify the electric distribution in the bulk. The electrodes are supposed perfectly conductive, that is, no voltage gradients in the electrode. The dielectric layer modifies the electric field by means of the dielectric constant. The liquid crystal layer itself is reduced to the boundary layers and the bulk. Since strong anchoring will be assumed, the boundary layers have no degree of freedom, only the directors in the bulk are allowed to change orientation.

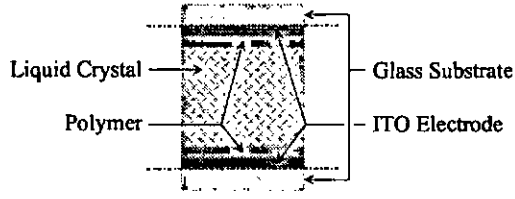

Figure 3.1: *Scheme of a liquid crystal device. The dash-dotted lines represent the limit of the cell model used for the calculation.*

3.3 Description of the contributions to the total energy

As seen from the description of the device, different contributions must be taken into account when dealing with liquid crystal devices. Not only the liquid crystal itself, but also the electric field and the effect of dielectric layers (polyimide, glass) are important. The different contributions to the energy are

$$F_{system} = F_{elastic} + F_{electric} + F_{boundaries} + F_{kinetic} + F_{i}. \tag{3.1}$$

The elastic energy $F_{elastic}$ of the stressed liquid crystal, the electric energy $F_{electric}$ from the electric field in the liquid crystal bulk resulting from the voltage applied to the ITO electrodes, the anchoring energy $F_{boundaries}$ at the liquid crystal - polymer interface, and the rotational energy $F_{kinetic}$ during transitions between two stable states. Other contributions F_i, such as flexo-electric phenomena or flow in the cell are neglected, since we are mainly interested in the final, stable states. Note that orientational variations are taken into account by $F_{kinetic}$, but not positional variations. The following paragraphs will discuss these different contributions.

3.3.1 Free energy of the distorted nematic liquid crystal bulk

The most commonly used model for the description of nematic distorted liquid crystal configurations is a macroscopic model [5, 30, 2]. The model assumes that the system is a weakly distorted continuous and anisotropic medium. This can be admitted considering that the thickness d of the device is in the μm range, typically 5 μm, while the longest dimension a of a liquid crystal molecule would be in the nm range. Since $a/d \ll 1$, the local optical properties are those of a uniaxial crystal with an extraordinary and ordinary refractive index n_e and n_o, respectively. Thus, the liquid crystal molecule is described by a vector $\mathbf{n}(\mathbf{r})$, called director, which gives the orientation $\mathbf{n}$ of the long axis of the rod-like (calamitic) molecules considered here, at any position $\mathbf{r}$ within the considered volume. The director is a unitary vector that represents the orientation of the molecules, and thus the states $-\mathbf{n}$ and $+\mathbf{n}$ are equivalent.

When one molecule changes its position relative to its neighbor molecules, the energy of the system is changed. The macroscopic model considers that the neighbor molecules exert an elastic force against the deformation. This amount of energy, given as energy density, is [5]

$$f_d = \frac{1}{2}\left\{K_{11}\,(div\,\mathbf{n})^2 + K_{22}\,(\mathbf{n}\cdot\mathbf{rot}\,\mathbf{n} + q_0)^2 + K_{33}\,(\mathbf{n}\times\mathbf{rot}\,\mathbf{n})^2\right\} \tag{3.2}$$

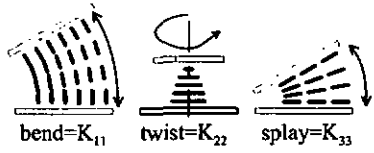

Figure 3.2: *Schematic description of the stress required for pure bend, twist and splay deformation.*

Equation (3.2) is the simplified formula of the Frank-Oseen model as already discussed in Eq. (1.2). This is the simplest formulation, with only three elastic contributions. It concerns

only the bulk of the liquid crystal and neglects other coefficients, specially surface contributions. Three different contributions are considered: pure splay, characterized by the elastic constant K_{11}, pure twist characterized by K_{22} and finally pure bend deformation, represented by K_{33}, as shown in Fig. 3.2. In the commonly used liquid crystal mixtures, $K_{33} > K_{11} > K_{22}$, and the order of magnitude is $10^{-11}N$. q_0 is a parameter added when the nematic includes a chiral dopant mixture to force the liquid crystal to twist in a given sense of rotation. This is required by the helical arrangement of the cholesteric texture, and also for the super-twisted nematic devices (STN) to assure the correct relaxed configuration, or in twisted nematic devices (TN) to avoid reverse twist.

One constant approximation

A common problem when dealing with this formula is the lack of a complete characterization of the liquid crystal parameters. It is indeed very rare that data sheets contains all of the three elastic constants. On the other hand, excluding very specific and friendly configurations, no analytical solution can be easily obtained from Eq. (3.2). A simplified model assumes that all three constants are identical, that is,

$$K_{11} = K_{22} = K_{33} = K. \tag{3.3}$$

Obviously, and given the differences between the elastic constants, this is a very rough approximation, but useful for estimations [31] or when no other data are available. After this simplification, the free energy density becomes [5]

$$f_d = \frac{1}{2}K\left\{(div\,\mathbf{n})^2 + (\mathrm{rot}\,\mathbf{n})^2\right\}. \tag{3.4}$$

3.3.2 The anchoring of the molecules at the surface

One of the most important problems in the realization of liquid crystal devices is to define the initial or relaxed state by an appropriate choice of the boundary conditions. Any perturbations in this initial configuration will be clearly visible. These perturbations create the so-called disclinations that describe a discontinuous transition between different domains [31]. Those zones can have different structures or arrangements and thus have different optical behavior, which

is usually not desired. These disclinations can have different origins, such as scratches on the substrate, spacers, dust, dirt or even the electric field.

The strength of the anchoring is a very important aspect of the liquid crystal device. If the anchoring surface is able to fix a well defined easy state, the anchoring is assumed to be strong, and independent of external stress, specially from the liquid crystal bulk. This is an important consideration, which reduces the calculation of the minimal energy density to the minima of the liquid crystal bulk energy density, with the boundary conditions imposed by the anchoring. The energetic contribution of the liquid crystal is therefore limited to the bulk, described by Eq. (3.2).

3.3.3 External field effects

External fields, either electric or magnetic, can modify the arrangement of the director within the liquid crystal bulk thanks to the orientational freedom of the molecules and its electric properties. With the assumptions made before, it comes out that the external field results in a torque applied to the molecule which will change only its orientation. The origin of this torque is different for different liquid crystal phases. In the case of the nematics, it is the dielectric or diamagnetic anisotropy which is responsible for the rearrangement. Under the action of an electric field, the molecular diclectric anisotropy results in a torque which tends to rotate the molecule and align it with the local field. The rotation will occur in the sense of minimizing the electric energy of the system.

As already shown in Eq. (1.3), the energy density

$$f_e = \mathbf{D} \cdot \mathbf{E} = (\varepsilon \cdot \mathbf{E}) \cdot \mathbf{E} \tag{3.5}$$

is the product of the electric field E and the electric displacement field D caused by the dielectric anisotropic media, ε being the dielectric anisotropy tensor that links the dielectric anisotropy with the director orientation n.

3.3.4 Viscosity

Another contribution to the behavior of confined liquid crystals is the viscosity. Apart from the a pure twist dcformation [5], any modification in the orientation of the molecules will result in flow. Flow in confined spaces is the result of pressure gradients. Nevertheless, flow is neglected. The only contribution taken in account is the rotational motion, since the model assumes that n (r) only represents the orientation of the molecules.

From the six viscosity constants, known as Leslie constants, the resulting rotational viscosity constant γ_1 is the only one taken into account, given that the model does not consider position changes of the molecules, i.e. flow. The rotational viscosity determines the evolution in time to the equilibrium state of the liquid crystal

$$\Gamma = \gamma_1 \frac{\partial \mathbf{n}}{\partial t}. \tag{3.6}$$

This is the only time dependent contribution in the macroscopic model.

3.3.5 Final description of the nematic liquid crystal device.

Four contributions to the director configuration have been presented. All these contributions act together in order to balance each other. The distorted liquid crystal will thus minimize the overall energy and reach an equilibrium state. Strong anchoring is assumed, and the anchoring energy is not considered. As a result, we obtain

$$F_{tot} = F_d + F_e + F_v, \tag{3.7}$$

where the F_i are the energies in the considered volume after integration of the energy densities f_i. With the addition of all energetic contributions, it is possible to minimize the energy of the system. Neglecting flow and flexo-electric contributions and assuming that the liquid crystal is not compressible, the instantaneous director distribution is obtained from [32]

$$\gamma_1 \frac{\partial \mathbf{n}}{\partial t} = \frac{d}{d\mathbf{r}} \left(\frac{\partial F}{\partial \mathbf{n}} \right) - \frac{\partial F}{\partial \mathbf{n}} + \lambda \cdot \mathbf{n} \tag{3.8}$$

where $\mathbf{n}(\mathbf{r})$ is the director at the position $\mathbf{r}$, and λ is a Lagrange multiplier required to assure that $\|\mathbf{n}\| = 1$.

3.3.6 Analytical solutions to the energy equation

To solve the differential Eq. (3.8) is not trivial. The only way to solve this equation is to use numerical methods, such as the finite element method. Nevertheless, with appropriate assumptions and simplifications, some important results can be obtained analytically. This results are, for example, the threshold voltage (or Fredericks transition voltage) and the switching-on and

switching-off times. Those are fundamental characteristics of a liquid crystal device, which describe its performance. For example, in matrix devices refreshing time is limited by the switch-off time, while the electronic driving requirements are given by the threshold voltage.

The assumptions made concern basically the director distribution and the characteristics of the cell. As explained before, anchoring is considered strong, and the boundary directors are thus fixed. Also, the only boundaries considered are the upper and lower substrates, whose relative distance defines the thickness. Otherwise, the device has an infinite extension, avoiding any lateral contribution from neighboring molecules. The calculation is made along the axis defining the thickness and the liquid crystal is represented as a column of directors. The components of these directors are illustrated in fig. (3.3) and are then given by

$$\mathbf{n} = \begin{bmatrix} n_x \\ n_y \\ n_z \end{bmatrix} = \begin{bmatrix} \cos(\varphi)\cos(\theta) \\ \cos(\varphi)\sin(\theta) \\ \sin(\varphi) \end{bmatrix}. \tag{3.9}$$

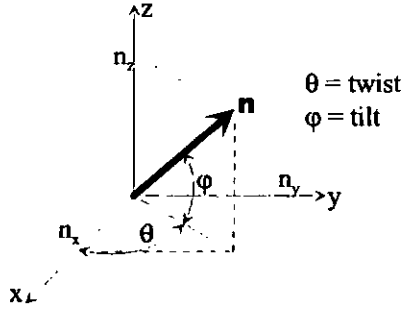

Figure 3.3: *Representation of the tilt (polar angle φ) and twist (azimuth angle θ) of the director* **n**.

Nematic alignment: pure twist deformation

The simplest configuration to solve analytically the Frank-Oseen Eq. (3.8) is the homogeneous-planar configuration [5, 30] shown in Fig. 3.4. The anchored molecules are parallel to each other and practically parallel to the surface. The director points perpendicular to the schematic section drawn. The external field is applied perpendicular to the molecules, which can be realized by

two parallel stripes of electrodes. This specific configuration allows to describe the director field

$$\mathbf{n} = \begin{bmatrix} \cos(\theta) \\ \sin(\theta) \\ 0 \end{bmatrix} \tag{3.10}$$

by a single variable, the twist angle $\theta(z)$, and the electric field

$$\mathbf{E} = \begin{bmatrix} 0 \\ E_y \\ 0 \end{bmatrix}. \tag{3.11}$$

The system is now reduced to a single equation and therefore becomes scalar. The dielectric tensor ϵ is now a scalar of the form $\epsilon_0 \cdot \Delta\epsilon$.

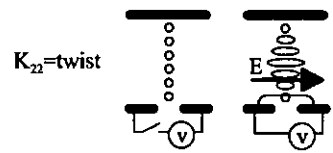

Figure 3.4: *Schematic device for pure twist deformation* ($E = E_y$).

The director profile rotates in the x,y plane, changing only its twist angle $\theta(z)$. Compared to pure splay or pure bend deformation, this is the only configuration where the dynamic behavior is not affected by back-flow. Under these conditions, one gets from Eq. (3.8) the differential equation

$$K_{22} \cdot \frac{d^2\theta}{dz^2} + \Delta\epsilon \cdot \epsilon_0 \cdot E_y^2 \cdot \sin(\theta) \cdot \cos(\theta) = \gamma_1 \cdot \frac{d\theta}{dt} \tag{3.12}$$

for the twist angle $\theta(z,t)$ as function of the position z and the time t. With the additional assumption that θ changes continuously, and $\theta \ll 1$, the equation simplifies to

$$K_{22} \cdot \frac{d^2\theta}{dz^2} + \Delta\epsilon \cdot \epsilon_0 \cdot E_y^2 \cdot \theta = \gamma_1 \cdot \frac{d\theta}{dt}, \tag{3.13}$$

which has the solution

$$\theta(z,t) = \theta_{max} \cdot \sin\left(\frac{\pi \cdot z}{d}\right) \cdot \exp\left(\frac{-t}{\tau}\right), \tag{3.14}$$

where τ is a time constant, d is the cell thickness, and $\theta_{max} = \theta(d/2)$ is the maximal twist angle at the center of the cell.

At equilibrium, the time-dependent term disappears and the Eq. (3.13) can be solved for the electrical field, using Eq. (3.14). The result gives the threshold field

$$E_{th} = \frac{\pi}{d}\sqrt{\frac{K_{22}}{\Delta\varepsilon \cdot \varepsilon_o}}. \tag{3.15}$$

necessary to induce any deformation through the electrical field.

Solving Eq. (3.13) including the time dependence gives the switch-on and switch-off times of the device. Under the action of the electric field the switching-on or rise time, that means, the time required to move from the relaxed state to the corresponding switched states $\theta\,(d/2) = 0$ *to* $\theta\,(d/2) = \theta_{max}$, is obtained by introducing $\partial^2\theta/\partial z^2 = -\theta \cdot (\pi/d)^2$ and $\partial\theta/\partial t = -\theta/\tau$, into Eq. (3.13). Solving for τ, one obtains for the rise-time or switch-on

$$\tau_r = \frac{\gamma_1}{\Delta\varepsilon \cdot \varepsilon_0 \cdot \left(E_y^2 - E_{th}^2\right)}, \tag{3.16}$$

for $E_y < E_{th}$, and for the fall-time or switching-off with $E_y = 0$

$$\tau_f = \frac{\gamma_1}{\Delta\epsilon \cdot \epsilon_0 \cdot E_{th}^2} = \frac{\gamma_1 \cdot d^2}{K_{22} \cdot \pi^2}. \tag{3.17}$$

From the previous equations, we recognize the most important parameters of the liquid crystal devices. Concerning the switching properties, the liquid crystal constants K_{ii} and $\Delta\epsilon$ are determinant, together with the effective liquid crystal thickness d. The time constants are directly proportional to the square value of the thickness, $\tau \propto d^2$, which is the most easily changeable variable, compared with the liquid crystal parameters.

The results in Table 3.1 give an idea of the typical values for the liquid crystal BL006 from Merck[TM]. Neglecting the flow effects during the switching, which modify the effective rotational viscosity, the above equations are also commonly used to get approximate results for the device.

The pure twist configuration has gained interest in recent years because of the improved optical properties of this type of device, compared with the classical twisted nematic (TN) and super-twisted nematic (STN) configurations. A mayor drawback is the dependence on the twist elastic constant K_{22}, which has always the lowest value of the three elastic constants considered, resulting in a very large relaxation time (τ_f) as can be seen in Table 3.1.

	γ_1 Pa.s	K_{ii} pN	$\Delta\epsilon$	E_{th} V/μm	U_{th} V	τ_f ms	τ_r (5 V) ms
splay (K_{11})	0.071	17.9	15.5	0.227	1.135	10.05	0.55
twist (K_{22})	0.071	15	15.5	0.208	1.040	12	0.54
bend (K_{33})	0.071	33	15.5	0.308	1.540	5.45	0.57

Table 3.1: *Physicol praperties of BL006 and estimations for th threshold electric field E_{th}, the corresponding voltoge U_{th}, the foll time τ_f ond the rise time τ_r corresponding to an applied voltage of 5 V. For splay and bend, these are rough approximations. (thickness = 5 μm)*

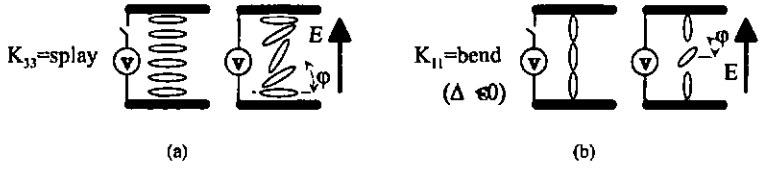

Figure 3.5: *Other configurations for nematic liquid crystals. (a) planar configuration, (b) homeotropic configuration, which requires negative dielectric onisotropy to be switched with a vertical field. With the configuration in Fig. 3.3, positive anisotrapy is used.*

Threshold voltage for the planar configuration shown in Fig. 3.5a is obtained from

$$\left(K_{11}\cos^2(\varphi)+K_{33}\sin^2(\varphi)\right)\frac{d^2\varphi}{dz^2}+\left[(K_{33}-K_{11})\cdot\left(\frac{d\varphi}{dz}\right)^2+\varepsilon_o\cdot\Delta\varepsilon\cdot E^2\right]\cdot\sin(\varphi)\cdot\cos(\varphi)=0, \tag{3.18}$$

which results from the solution of Eq. (3.8) for tilt ($\varphi(z)$) modulation [33]. Figure 3.5b shows the homeotropic configuration ($pre-tilt \simeq 90^o$) which requires negative dielectric anisotropy. The same result as for the planar configuration is obtained, permuting K_{11} and K_{33} in Eq. (3.18).

Since the threshold voltage is the voltage for which the director begins to change, φ and $d\varphi/dz \ll 1$, and the small angles approximation can be applied, i.e. $\sin(\varphi) \approx \varphi \ll 1$ and $\cos(\varphi) \approx 1$. This result in an equation similar to Eq. (3.13) but for the tilt modulation ($\varphi(z)$) and for elastic constants K_{11} and K_{33} respectively. Therefore, the same solution for the threshold electric field is found for the respective elastic constants. Nevertheless, Eq. (3.18) clearly demonstrates that pure bend or pure splay configurations do not exist. For simplicity and admitting that the medium will be weakly distorted, the previous equations are also used for these other types of deformations. The main interest is to include the fact that when the electric field

is perpendicular to the substrates

$$V_{th} = \frac{E_{th}}{d} = \pi \cdot \sqrt{\frac{K_{ii}}{\Delta\varepsilon \cdot \varepsilon_o}} \tag{3.19}$$

which is indcpendent of thc thickness of the liquid crystal layer. Table 3.1 resumes the results for all the configurations shown.

More accurate formulas for TN and STN configurations have been developed, including all three elastic constants [30]. For TN cells, the threshold voltage is found to be [30]

$$U_{th}^{TN} = \pi \sqrt{\frac{\pi}{\Delta\varepsilon \cdot \varepsilon_0}(4 \cdot K_{11} + K_{33} - 2 \cdot K_{22})}, \tag{3.20}$$

and for STN cells by [30]

$$U_{th}^{STN} = U_S \cdot \sqrt{1 + \frac{\theta_m}{\pi}\left(\frac{\theta_m}{\pi}\left(\frac{K_{33}}{K_{11}} - \frac{2 \cdot K_{22}}{K_{11}}\right) + \frac{4 \cdot K_{22} \cdot d}{K_{11} \cdot q_0}\right)} \tag{3.21}$$

$$U_S = \pi \sqrt{\frac{4\pi \cdot K_{11}}{\Delta\varepsilon \cdot \varepsilon_0}} \tag{3.22}$$

where θ_m is the pre-twist angle, d the thickness of the cell, and q_0 the liquid crystal pitch.

3.4 Calculation of the director profile with numerical methods

Analytical solutions for the director profile are useful approximations to obtain an overall idea of the behavior of the liquid crystal, but they are of limited value as a design tool. When more precise results are required, specially if two and three dimensional systems including fringing fields are considered, numerical solutions of the energy differential equation are necessary. In recent years, commercial software has become available. These programs (LCDMaster [22], TWIST [34], 2DIMOS [35]) include also some optical analysis features, such as the electro-optic response curve or thc viewing angle dependence. The analysis is completed with the addition of other optical components, such as polarizers and retardation plates.

The finite elements are commonly used to solve nonlinear problems. Typical applications of this approach are mechanical stress problems or heat transfer. The linearization of the equation is obtained by reducing the problem to a subset of small problems where a linear approximation

can be accepted [36, 37]. The derivatives are then substituted by finite differences [38].

3.4.1 Discrete model of the system

The system is divided in small pieces represented by a grid. Each point of the grid characterizes the device at this point. The physical properties of the media at the point, as well as the variables, are associated to each point. The spatial derivatives are then substituted be the differences between neighbor points of the grid. Time derivatives are obtained from two different instants at the same point.

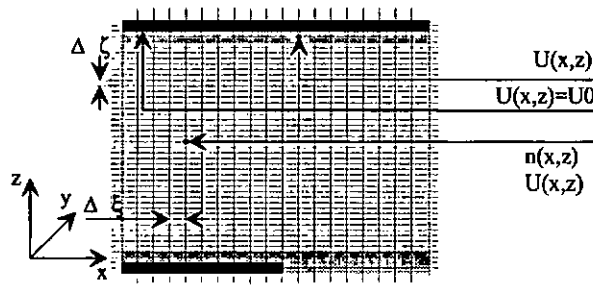

Figure 3.6: *Regular grid for finite element calculation in LCDMaster for two-dimensional problem. The black stripes represent the electrodes, which have a fixed voltage* U_0. *From these conditions, the electric potential* $U(x,z)$ *in the dielectric layers (grey stripes), as well as the electric field* $U(x,z)$ *and director* $\mathbf{n}(x,z)$ *orientation in the liquid crystal are calculated.*

The accuracy of the calculation is directly related to the mesh size in critical points. For optimal results, the grid should be adapted to the requirements of the calculations. A denser distribution of points is necessary where the gradients are high. Classical finite elements programs, for example for mechanical stress calculation, are self-adaptive, that means that the mesh is adapted by the program itself to be denser in critical points. In the case of LCDMaster [22], the grid is orthogonal and regularly spaced. This approach is not optimal, so that either the calculation is not accurate in some points of the grid or, the calculation takes too long to obtain the desired accuracy. The reason to do this is the simplicity of implementation and the fact that optical calculation is easy to perform with layered structures as will be discussed in the following chapter. Figure 3.6 shows the grid for a two-dimensional device model. Liquid crystal devices have different media to be considered for the calculations, which are, the liquid crystal, the dielectric layers and the electrodes. Each medium has a different effect on the electric field and different boundary conditions have to be imposed.

3.4.2 Boundary conditions for the electric field

Boundary conditions for the electrodes

The electrodes are considered ideal conductive media, which means that the whole electrode is at the same electric potential. Therefore, no gradients are possible in the electrode and along the boundaries of the electrode. Fixing the boundary value to solve the finite element problem is known as the Dirichlet [38] condition,

$$U_{electrode} = const. \tag{3.23}$$

The boundary of the electrode is an equipotential line, the electric field must be perpendicular to the boundary. This implies a condition for the gradients of the electric field, which is known as Neumann condition, and results in the equation

$$\frac{\partial}{\partial x} U_{boundary} = 0. \tag{3.24}$$

The Neumann condition is represented in Fig. 3.7 as B:. The field vector E points perpendicular to the boundary line, while the equipotential line (U=const.) is parallel to the boundary. In fact, the boundary is an equipotential line itself.

Boundary conditions for a periodic structure.

For a periodic structure, along the x or y axis, it is sufficient to calculate one period and to respect specific lateral boundary conditions. These boundaries are the left and right limits of Figs. 3.6 or 3.7. While the Neumann condition represents a kind of infinite extension of the media after the boundary, the periodic boundary condition imposes two constraints. Given that the first boundary and the last boundary must be identical because they represent the same point within the periodic structure, the condition is

$$U_{boundary}\left(\; X_{px} \quad Y_{py} \quad z \; \right) = U_{boundary}\left(\; X_0 \quad Y_0 \quad z \; \right), \forall z \tag{3.25}$$

where X_0, X_{px} represent both boundaries for the periodicity along x, with px as the period length, and Y_0, Y_{py} represent both boundaries for the periodicity along y with py as the period length. In this case the three-dimensional device is periodic in x and y. However, this condition is not jet sufficient; the gradient must also be a continuous function. This imposes the gradient along the axis of periodicity to be constant. It follows, for the X boundary,

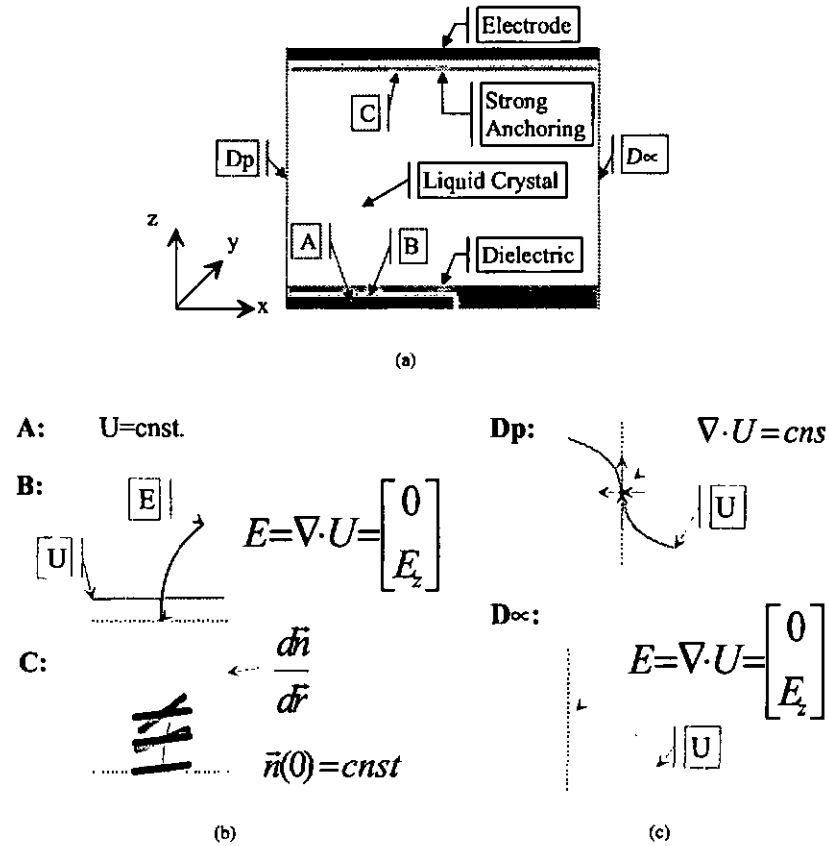

Figure 3.7: *Schematic representation of the different electric boundary conditions imposed to the system. A: Dirichlet condition. B: Neumann electrode-dielectric boundary condition. C: dielectric-LC boundary condition. D's: loterol periodic or infinity condition. The boundary is represented by a dotted line.*

$$\frac{\partial}{\partial x}U\left(X_0 \;\; y \;\; z\right)=\frac{\partial}{\partial x}U\left(X_{px} \;\; y \;\; z\right),\forall y,z \tag{3.26}$$

as shown in Fig. 3.7 as *Dp*. On the other hand, the normal Neumann condition represented in Fig. 3.7 as *D*∞ applies when the boundary is not periodic. There is no possibility to cause a gradient

by an external source. Therefore, the equipotential lines are perpendicular to this boundary and the electric field parallel is horizontal, i.e. $E_x = E_y = 0$ and $\mathrm{E} = E_z$.

3.4.3 Boundary condition for the liquid crystal

The liquid crystal boundaries are imposed by the model used for the energy calculation. As explained in section 3.3.2, the model assumes strong anchoring, which means that the molecules in contact with the interface cannot be reoriented by any means. The values of the directors of the interface are fixed and time independent. For the Z boundaries, the strong anchoring condition with the Neumann conditions are always valid (C in Fig. 3.7), while either periodic or Neumann conditions are possible for the X and Y boundaries.

3.4.4 Implementation of linear equations for the calculation

In the case of the energy equilibrium, the Lagrange multiplier λ is eliminated by multiplying Eq. (3.8) with n. Thus, the final formula used for the calculation is [32]

$$\gamma_1 \frac{\partial n_i}{\partial t} = (\delta_{ik} - n_i \cdot n_k) \left[\frac{\partial}{\partial x_j} \left(\frac{\partial F}{\partial n_{k,j}} \right) - \frac{\partial F}{\partial n_{k,k}} \right]. \tag{3.27}$$

From the Maxwell equations, and assuming that there are no charges, it follows that

$$div\,(\mathbf{D}) = div\,(\epsilon \cdot \mathrm{E}) = div\,(\epsilon \cdot \mathrm{grad}U) = 0. \tag{3.28}$$

For the calculation, the electric potential $U\,(\mathrm{r})$ is used, which is a scalar field [32], yielding

$$\frac{\partial}{\partial x_i} \left(\epsilon_{ij} \cdot \frac{\partial U}{\partial x_j} \right) = \frac{\partial}{\partial x_i} \left(\left[\epsilon_{\parallel} \cdot \delta_{ij} + \left(\epsilon_{\parallel} - \epsilon_{\perp} \right) \cdot n_i \cdot n_j \right] \cdot \frac{\partial U}{\partial x_j} \right) = 0 \tag{3.29}$$

The final step is to implement the derivatives as finite differences using the most appropriate methods [36, 37, 32, 38].

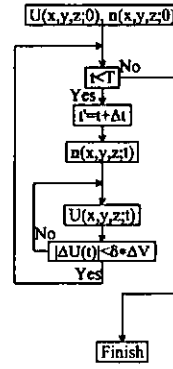

Figure 3.8: *Flow Chart of the calculation algorithm used in LCDMaster for two and three-dimensional calculations.*

3.4.5 Calculation algorithm.

In Fig. 3.8 the calculation flow chart is shown. This diagram shows that two different conditions control the loop, i.e. the time of calculation T and the electric potential correction $\delta \cdot \Delta V$. The increments in time (Δt) are fixed by the user, and an indicative value can be calculated using first order diffusion equations [32]. If the increment is too large, the equations do not converge. For one-dimensional calculations, it is possible to calculate until the system has reached equilibrium and the time condition falls. The loop is then controlled by the electric gradient.

The first operation is to adjust the director n orientation according to the electric field distribution from the previous step. Through this operation, the dielectric anisotropy distribution is also changed. The electric potential at each point is therefore re-calculated accordingly to Eqs. (3.28) and (3.29). This correction is made with a loop within the main loop which is controlled by the condition [32]

$$|\Delta U_{ij}| =\leq \delta \cdot |V_{max} - V_{min}|\,, \tag{3.30}$$

where δ is the error parameter set by the user and V_{max}, V_{min} are the highest and lowest potential values set by the user. This coefficient sets a limit to the modifications in the distribution of the electric field U, that is, it sets a limit to the intensity of the local electric field E during calculation. As for the time increments Δt, there is no convergence if the factor $\delta \cdot \Delta V$ is too large.

3.4.6 Examples of director profiles

One-dimensional simulations

A typical application of the simulation tool is to calculate the electro-optic behavior and the time required to switch-on and switch-off a TN cell. The electro-optic behavior is the relation between the applied voltage and the transmission through crossed polarizers. This is directly related to the re-arrangement of the directors by the electric fields applied. In Fig. 3.9 the tilt and twist angle along the thickness of a typical TN cell are shown at the equilibrium state for U = 0, 1, 2, 3, 4 and 5 V.

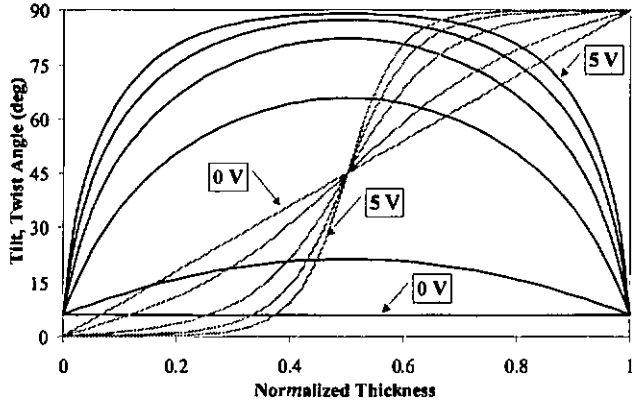

Figure 3.9: *One-dimensional simulation of a twisted nematic cell. The black lines represent the tilt angle between the pre-tilt value and the $\pi/2$ maximal value. The gray lines represent the twist angle going from 0 to $\pi/2$. (thickness d = 5 μm, pre-tilt = 6°, number of layers N = 50)*

At 0 V, the twist angle plotted as grey lines changes linearly from 0° to 90° along the thickness, while the tilt angle remains the same, fixed by the pre-tilt value. Increasing the applied voltage changes both tilt and twist, but differently. The tilt angle is mainly changed in the middle layer, increasing until the limit of 90° is reached. A smooth transition between this value and the pre-tilt angle determines the tilt across the cell. Higher voltage increases the part of directors reaching the upper tilt limit $\pi/2$. Meanwhile, the twist changes differently. On both extremities, the twist angle tends to become parallel to the alignment (0 or $\pi/2$), and the twisted helix is compressed to the center of the cell reducing its pitch. The transition becomes steep.

Figure 3.10 shows the temporal behavior of this re-orientation when the voltage is applied.

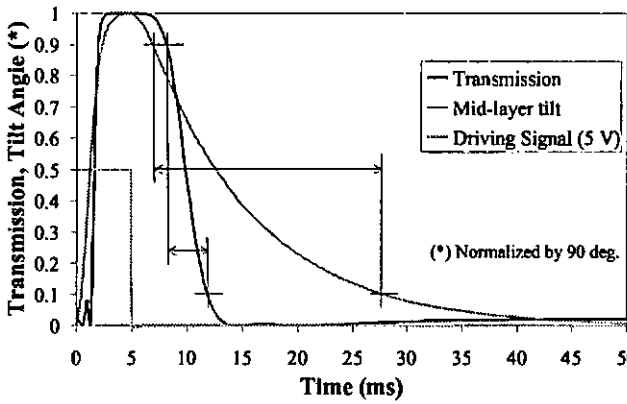

Figure 3.10: *Evolution of the mid-layer tilt angle vs. time in a TN cell when a voltage is applied (switch-on) and removed (switch-off). Transmission through parallel polarizers, aligned with one of the alignment layers*

The response is quite fast for full commutation accordingly to Eq. (3.16). As already shown in Table 3.1, the switch-on time is in the ms range. On the other hand, when the voltage is removed, the system tries to recover the initial relaxed state. This is a relaxation phenomena and this switching-off process will take longer time, as was described by Eq. (3.17). It will depend on the energy stored ($K_{ii}'s$) and the viscosity (γ_1), and it shows an exponential decay. The transmission through parallel polarizers of the TN cell has been added to show that transmission is not linearly related to the mid-layer tilt. Propagation through liquid crystals is discussed in chapter 4.

Two- and three-dimensional simulations

The extreme complexity of the director profiles in two and three dimensions makes the calculation of the equilibrium state too complex to be calculated directly. Instead, the temporal evolution is calculated until a stable distribution is reached. In the following figures, a two dimensional and a three-dimensional simulation are shown. A typical two dimensional simulation describes the cross-section of a diffractive grating, while a lens is a typical case of three dimensional simulation.

Figure 3.11 shows the structure of a simulated period of a planar-nematic grating. All three fundamental components of the cell, i.e. the electrodes, the dielectric layer and the liquid crystal directors, are represented, together with the electric equipotential lines. The directors, repre-

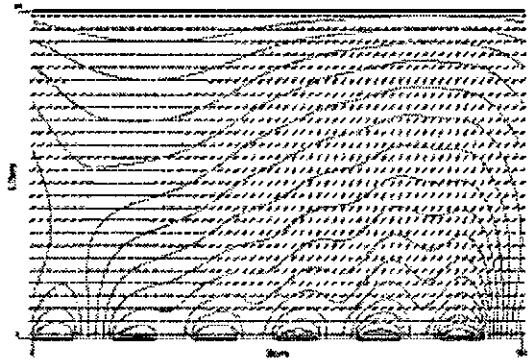

(a)

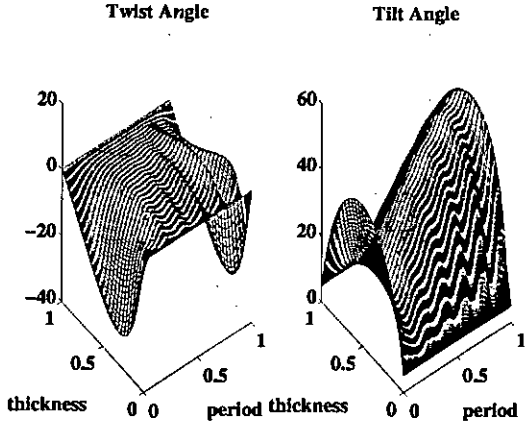

(b)

Figure 3.11: *Two-dimensional simulation for one period of a nematic multilevel grating. a) LCDMaster result with the equipotential lines and the short slabs representing the directors. b) tilt and twist distribution over the thickness and within one period. (Nx =300 layers, Nz =70 layers, thickness d = 6 μm, LC:BL006, t=200 ms).*

sented by short slabs, tend to align with the gradient of the electric potential U, which is the electric field E. The continuity at the lateral boundaries imposed by the periodic boundary condition appears clearly.

The three-dimensional simulation in Fig. 3.12 corresponds to a micro-lens. The lens function is caused by the orientation with the fringing field, resulting from the structured hole in the conductive layer. Due to the planar alignment, the dielectric anisotropy and the strong anchoring, the resulting electric field distribution and the resulting director distribution has not rotational symmetry. Figure 3.12b shows that the director pattern is not centered, but rather shifted, in the mid-layer of the cell. Cross-sections (Figs. 3.12a,c) of the same cell show also this asymmetry and even some reverse tilt in Fig. 3.12c.

3.5 Summary

1. *The macroscopic Fronk-Oseen model is used.* The elastic energy is calculated after three elastic constants corresponding to splay (K_{11}), twist (K_{22}) and bend (K_{33}). An eventual chirality is represented by the pitch parameter q_0.

$$f_d = \frac{1}{2}\left\{K_{11}\,(div\,\mathbf{n})^2 + K_{22}\,(\mathbf{n}\cdot\mathbf{rot}\,\mathbf{n} + q_0)^2 + K_{33}\,(\mathbf{n}\times\mathbf{rot}\,\mathbf{n})^2\right\}.$$

2. *External electric fields* E *rearronge the directors* n. The interaction is possible through the dielectric anisotropy represented by the tensor ε.

$$f_e = D\cdot\mathbf{E} = (\varepsilon\cdot\mathbf{E})\cdot\mathbf{E}.$$

3. *Only rotational viscosity* (γ_1) *is considered.* Flow, flexo-electricity or any other effect is not taken into account. The equilibrium of $F = f_d + f_e$ is calculated after

$$\gamma_1\frac{\partial\mathbf{n}}{\partial t} = \frac{d}{d\mathbf{r}}\left(\frac{\partial F}{\partial\mathbf{n}}\right) - \frac{\partial F}{\partial\mathbf{n}} + \lambda\cdot\mathbf{n}.$$

4. *There are no analytical solutions for the previous equation.* Approximate results for threshold voltages and rise and decay times are found in section 3.3.6.

5. *Finite difference methods are used to solve equilibrium equation.* commercial software like LCDMaster^{TM} or 2DIMOS^{TM} implement these algorithms to solve one- two- and

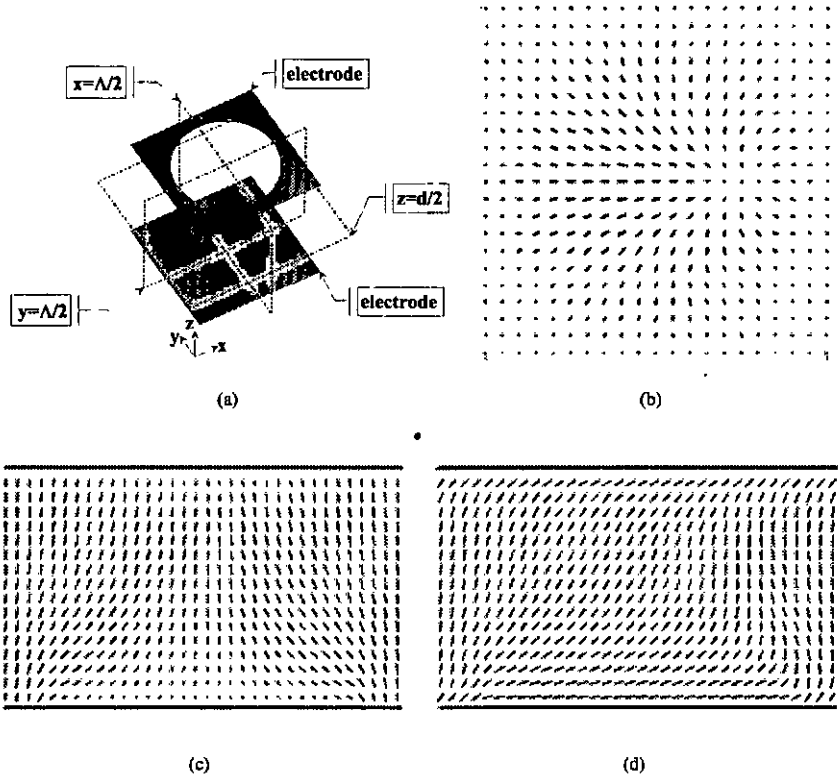

Figure 3.12: *Three-dimensional simulation of a planar-aligned micro-lens. a) model of the simulation cell. b) Horizontal cross-section at* $z = d/2$. *c) vertical cross-section at* $x = \Lambda/2$. *d) Vertical cross-section at* $y = \Lambda/2$. *(Dimensions: Box;* $150\ \mu m \times 150\ \mu m \times 50\ \mu m$, *diameter;* $120\ \mu m$, *mesh;* $100 \times 100 \times 70$, *LC: E7, pre-tilt* = $2°$).

three-dimensional problems. One-dimensional analysis is very complete, while two- and three-dimensional can only solve low resolution problems.

Chapter 4

Propagation in birefringent media

4.1 Introduction

Propagation of monochromatic waves through liquid crystals is considered in this chapter [39, 40, 41]. To calculate propagation of light through birefringent media, the Jones matrix calculus [39, 42, 43, 44] is the easiest to perform. Analytical solutions for special configurations can be found using this method [45, 46]. Rigorous methods based on the solution of Maxwell's equations, such as Berreman's 4×4 matrix method [47], are of interest when reflection must be taken into account, as it is the case for cholesterics [48].

Two and three-dimensional variations of the liquid crystal makes the calculation of light propagation more complicated. Wave propagation [49] or rigorous methods [50] have been proposed, but are hard to implement. The easiest solution is to use one-dimensional methods, that is, divide the cell in parallel columns and calculate straightforward. This is valid when normal incidence is considered and as long as the ray path can be assumed straight. Then, the calculation can be performed column-wise independently. Using ray-trace formulation [51, 52, 53], i.e. the Eikonal equation, this assumption can be proven for the thin layer gratings we use.

4.2 Representation of the polarization state

A monochromatic plane wave propagating along the $z - axis$ is described [54]

$$\mathbf{E}(z,t) = \mathbf{E} \cdot \cos\left(\omega \cdot t - n \cdot k \cdot z\right), \tag{4.1}$$

where E is the electric field, $\omega = 2\pi\upsilon$ the angular frequency, n the refractive index and $k = 2\pi/\lambda$ the wavenumber. In isotropic media, the transverse wave oscillates in a plane perpendicular to the axis of propagation. The state of polarization of this wave can be described by two orthogonal waves of the form

$$\begin{aligned} E_x(z,t) &= A \cdot \cos(\omega \cdot t - n \cdot k \cdot z - \delta_x) \\ E_y(z,t) &= B \cdot \cos(\omega \cdot t - n \cdot k \cdot z - \delta_y) \end{aligned} \quad , \tag{4.2}$$

with the amplitudes A and B, and the phase retardation δ_x and δ_y. Figure 4.1a shows the evolution in time of a wave in the xy plane, perpendicular to the propagation axis z. The polarization ellipse is determined by the ratio of the amplitudes $B/A = \tan\gamma$ and the phase difference $\delta = \delta_x - \delta_y$ of the two orthogonal waves. By a rotation of angle θ (azimuth), the ellipse is redefined by the semi-axes a and b and the ellipticity angle $b/a = \tan\varepsilon$. The amplitude of the wave is obtained from $E = \sqrt{a^2 + b^2}$.

Some special values of the ellipticity angle ε are interesting. Linear polarization is obtained when $\tan\varepsilon = 0$ and the ellipse collapses into a line. This occurs for $\delta = 0$ and for either $A = 0$ or $B = 0$. For $\tan\varepsilon = +1$ and $\tan\varepsilon = -1$ we obtain right-handed and left-handed circular polarized light respectively. This implies that $A = B$ and $\delta = \pm\pi$.

Another representation of the polarization is the Poincare sphere. With the relations

$$\begin{aligned} \tan 2\theta &= \tan 2\gamma \cdot \cos\delta \\ \sin 2\varepsilon &= \sin 2\gamma \cdot \sin\delta \end{aligned} \quad , \tag{4.3}$$

any polarization can be represented by a point on the surface of a sphere. As shown in Fig. 4.1b the circular polarization states ($\varepsilon = \pm\pi/4$) are the poles of the sphere, while the linear polarizations ($\varepsilon = 0$) are in the equator.

To determine the state of polarization from measurements, the Stokes parameters S_i are used. The relations

$$\begin{aligned} S_0 &= E_x \cdot E_x^* + E_y \cdot E_y^* = \sqrt{S_1^2 + S_2^2 + S_3^2} \\ S_1 &= E_x \cdot E_x^* - E_y \cdot E_y^* = S_0 \cdot \cos 2\varepsilon \cdot \cos 2\theta \\ S_2 &= E_x^* \cdot E_y + E_x \cdot E_y^* = S_0 \cdot \cos 2\varepsilon \cdot \sin 2\theta \\ S_3 &= E_x^* \cdot E_y - E_x \cdot E_y^* = S_0 \cdot \sin 2\varepsilon \end{aligned} \tag{4.4}$$

give the coordinates in the same space as the Poincare representation. Normalizing the S_i Stokes coordinates, we obtain Poincare coordinates $X_i = S_i/S_0$.

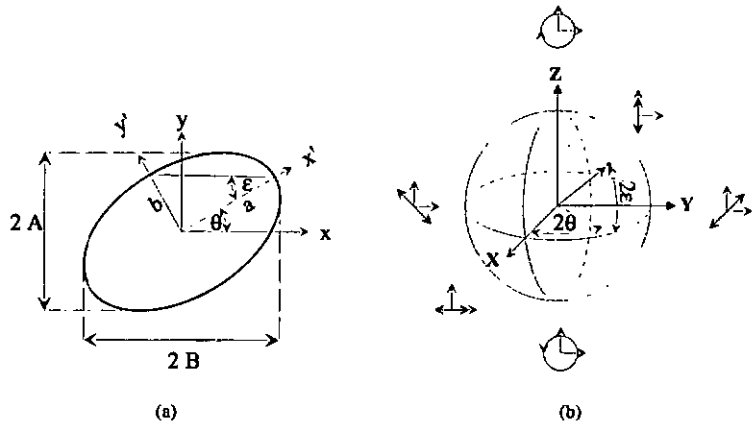

Figure 4.1: *Polarization representations a) Cartesian representation of the polarization ellipse. b) Poincare sphere used for the representation of the polarization.*

4.3 Jones matrix and paraxial propagation

The heavy notation used for the optical wave in Eq. (4.2) can be simplified by using the Jones representation of a polarized monochromatic wave. The temporal and spatial terms are equal for both components and can be omitted, reducing the representation of the polarization state to

$$\mathrm{j} = \begin{bmatrix} A \cdot \exp(-i \cdot \delta_x) \\ B \cdot \exp(-i \cdot \delta_y) \end{bmatrix}. \tag{4.5}$$

The propagation of polarized light through polarizing optical systems can be described by the Jones matrix formulation

$$\mathrm{j}_{out} = M \cdot \mathrm{j}_{in} \tag{4.6}$$

where j_{in} and j_{out} are the input and output Jones vectors defined in Eq. (4.5) and M is a 2×2 matrix, known as Jones matrix of the optical system.

For the case of propagation through birefringent media, the matrix takes the form

$$B = \begin{bmatrix} \exp(-i \cdot k \cdot d \cdot n_x) & 0 \\ 0 & \exp(-i \cdot k \cdot d \cdot n_y) \end{bmatrix}, \tag{4.7}$$

where $k = 2\pi/\lambda = \omega/c$ is the wavenumber, d the layer thickness and n_x and n_y are the refractive indexes of two eigen-polarizations. The phase of the two orthogonal waves are retarded by $k \cdot d \cdot n_{x,y}$. Known retardation plates are the half-wave plate, where $k \cdot d \cdot (n_x - n_y) = \pi$, and the quarter-wave plate, where $k \cdot d \cdot (n_x - n_y) = \pi/2$. The quarter-wave plate can transform a linear polarized wave into a circular one, and vice-versa.

Dichroic absorption is represented by the matrix

$$A = \begin{bmatrix} \exp(-\xi_x \cdot d) & 0 \\ 0 & \exp(-\xi_y \cdot d) \end{bmatrix}, \tag{4.8}$$

where ξ_x and ξ_y are the amplitude absorption coefficients of the two eigen-polarizations. For an ideal dichroic polarizer, the matrix becomes

$$P_x = \begin{bmatrix} 1 & 0 \\ 0 & 0 \end{bmatrix}. \tag{4.9}$$

Combined linear birefringence and dichroic absorption can be represented by the matrix

$$AB = \begin{bmatrix} \exp(-i \cdot d \cdot (k \cdot n_x - i \cdot \xi_x)) & 0 \\ 0 & \exp(-i \cdot d \cdot (k \cdot n_y - i \cdot \xi_y)) \end{bmatrix}. \tag{4.10}$$

If the elements are rotated with respect to the reference frame, the corresponding Jones matrices M_α are transformed as

$$M_\alpha = R(\alpha) \cdot M \cdot R(-\alpha), \tag{4.11}$$

where

$$R = \begin{bmatrix} \cos\alpha & \sin\alpha \\ -\sin\alpha & \cos\alpha \end{bmatrix} \tag{4.12}$$

is the well-known rotation matrix.

Optical activity of a media results in a rotation of the polarization state. The corresponding

Jones matrix O is therefore the same as the rotation matrix R but for the angle $-\alpha$, namely

$$O = \begin{bmatrix} \cos\alpha & -\sin\alpha \\ \sin\alpha & \cos\alpha \end{bmatrix}. \tag{4.13}$$

Typical liquid crystal devices have a twisted structure. For calculation, the device is modelized as a stack of retardation plates, each one slightly rotated respectively to the other. For TN or STN cells, the cell optical behavior is described by

$$M_T = \{R(-\alpha_N)\, B_N R(\alpha_N)\} \cdot \{R(-\alpha_{N-1})\, B_{N-1} R(\alpha_{N-1})\} \cdots \{R(-\alpha_1)\, B_1 R(\alpha_1)\}\,, \tag{4.14}$$

where α_i is the rotation angle of the i^{th} of N layers. Each of this layers of liquid crystal is characterized as a retardation plate B_i. For uniformly twisted configurations, $\alpha_i = \alpha = \theta/N$, where θ is the total twist and assuming $N \to \infty$, the final matrix becomes [39, 40],

$$M_0 = \begin{bmatrix} \frac{\sin(\theta\cdot\sigma)}{\sigma} & -\cos(\theta\cdot\sigma) - j\frac{u}{2}\frac{\sin(\theta\cdot\sigma)}{\sigma} \\ \cos(\theta\cdot\sigma) - j\frac{u}{2}\frac{\sin(\theta\cdot\sigma)}{\sigma} & \frac{\sin(\theta\cdot\sigma)}{\sigma} \end{bmatrix} \tag{4.15}$$

with the parameters $\sigma = \sqrt{1+u^2}$ and $u = \frac{\pi\cdot\Delta n\cdot d}{\theta\cdot\lambda}$.

As already discussed in the first chapter concerning the liquid crystal properties, the birefringence depends on the relative orientation of the molecules with respect to the wave-vector. In liquid crystal devices, it is the orientation of the molecules which is changed in order to change one of the refractive indexes of the propagating wave. Accordingly, the terms n_x, n_y have to be replaced by n_{eff} and n_o, where n_{eff} is given in Eq. (1.10).

Instead of tilt modulation, oblique incidence can also be considered [42, 43, 44], reformulating the LC-retardation matrix to take account of the effective angle between the ray and the tilted molecule and using Fresnel equation for the transmission-reflection matrix.

Analytic model for twisted nematic liquid crystals

With the matrix shown in Eq. (4.15) and ideal polarizers, like the one in Eq. (4.9), it is easy to describe the behavior of a uniformly twisted nematic cell, that is, in the off-state, when no voltage is applied. The classical configuration aligns the polarizer transmission axis with the alignment of the first liquid crystal layer. The output polarizer or analyzer is parallel or perpendicular to the first one. With this configuration, Gooch and Tarry [46] developed a formula for the transmission of twisted nematic devices. For the normally black configuration, that is, with parallel polarizers,

the matrix operations result in

$$\begin{bmatrix} 1 & 0 \\ 0 & 0 \end{bmatrix} \cdot M_\theta \cdot \begin{bmatrix} 1 & 0 \\ 0 & 0 \end{bmatrix} = \begin{bmatrix} \frac{\sin(\theta \cdot \sigma)}{\sigma} & 0 \\ 0 & 0 \end{bmatrix}. \tag{4.16}$$

Remembering that $\sigma = \sqrt{1+u^2}$, we obtain for the intensity transmission ,

$$T = \frac{\sin^2\left(\theta\sqrt{1+u^2}\right)}{(1+u^2)}, \tag{4.17}$$

with

$$u = \frac{\pi \cdot d \cdot \Delta n}{\theta \cdot \lambda}, \tag{4.18}$$

where θ is the overall twist angle, $\Delta n = n_e - n_o$ the birefringence, d the thickness and λ the optical wavelength.

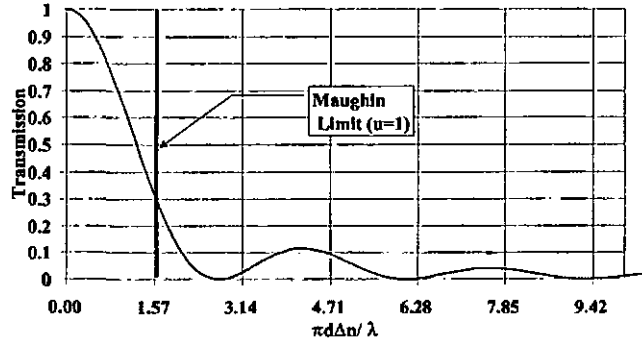

Figure 4.2: *Transmission for a TN cell ($\theta = \pi/2$) through parallel polarizers using Eq. (4.17). The minima correspond to linear polarization perpendicular to the analyzer.*

Figure 4.2 shows the transmission for a TN cell ($\theta = \pi/2$), using Eq. *(4.17)* with $\pi \cdot d \cdot \Delta n/\lambda$ as parameter. For $\pi \cdot d \cdot \Delta n/\lambda = 2.72$ The transmission is zero, which means that the output polarization is exactly linear and perpendicular to the analyzer. This is only valid for a single wavelength λ at a given thickness for a given liquid crystal ($\Delta n(\lambda)$), as shown in Eq. (4.18). In the first part of the curve, the device is said out of the Maughin condition

$$u \geq 1 \; or \; \pi \cdot \frac{d \cdot \Delta n}{\lambda} \geq \theta, \tag{4.19}$$

i.e. the twisted configuration characterized by the ratio d/θ is too short for the wave (λ) to be followed.

Ray propagation in inhomogeneous media

For the one-dimensional simulations, the propagation of the light ray is usually assumed to follow straight lines through the cell, since the cell is stratified along the z axis. Therefore, the index gradient exists only along z. This is not the case anymore in two or three-dimeosional simulations, where the directors are also laterally modulated across the cell. This means that transverse index gradients appear .

To obtain the phase profile from two or three-dimensional simulations done with LCDMaster, the easiest way to proceed is to calculate straightforward through the different columns of directors resulting from the regular orthogonal grid used by the program, as illustrated in Fig. 4.3. To proceed this way, a proof of the paraxial propagation of the ray is required. The effective index modulation ($n_{eff}(x,z)$) of a binary grating simulation is shown in Fig. 4.3a. The lateral modulation of the refractive index can render collinear calculation of the phase inaccurate [51] if the beam is deviated and propagates through a oeighbor column, as illustrated in Fig. 4.3b. If the ray propagates within a column not larger than the mesh step, and the angle at the output can be considered small, compared with the diffraction angle, Jones calculation can be considered valid.

The Fermat principle stipulates that the ray $\mathbf{r}(s)$ follows the shortest optical path between the points A and B, so that

$$\int_A^B n\,(\mathbf{r}) \cdot ds \rightarrow minimum, \tag{4.20}$$

which leads to [55],

$$\frac{d}{ds}\left(n(\mathbf{r})\frac{d\mathbf{r}}{ds}\right) = \mathbf{grad}\,(n)\,. \tag{4.21}$$

In homogeneous media (n=const.),one gets from Eq. (4.21) that rays propagate in straight lines. In this case, the optical path can be calculated as in Eq. (4.7) with $n \cdot d$. More accurate results require to take account of the gradients appearing from the switching of the liquid crystal and the finite dimensions of the electrodes.

To solve the two-dimensional case, we choose the coordinate system xz and the initial beam propagates along z, as illustrates Fig. 4.3b. The rays are represented by $x(z)$, so that the differential optical path becomes

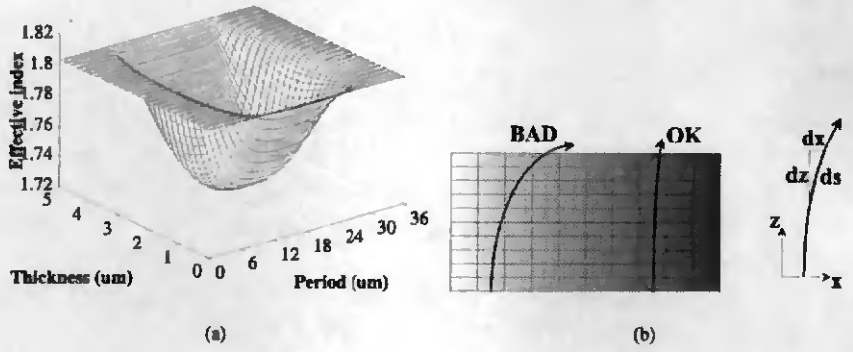

Figure 4.3: *Bi-dimensional gradients appearing in a two-dimensional simulation. a) Effective index* $(n_{eff}(x,z))$ *modulation through a period of a binary grating simulation. b) Column-wise calculation of the phase retardation after the regular grid obtained with LCDMaster. If the lateral gradient is too strong, the ray propagates out of the limits of a column. It is then not passible to proceed with Jones matrix calculation with the isolated columns.*

$$ds = dz \cdot \sqrt{1 + \left(\frac{dx}{dz}\right)^2} = dz \cdot \sqrt{1 + x'^2}. \tag{4.22}$$

We can proceed calculating the x component of Eq. (4.21), which yields to

$$\frac{n}{(1+x'^2)}x'' + \frac{\partial n}{\partial z} \cdot \frac{1}{(1+x'^2)} \cdot x' - \frac{n}{(1+x'^2)}x'^2 x'' = \frac{\partial n}{\partial x} \tag{4.23}$$

or

$$\frac{n}{(1+x'^2)}\left[x''(1-x'^2) + x' \cdot \frac{1}{n}\frac{\partial n}{\partial z}\right] = \frac{\partial n}{\partial x}, \tag{4.24}$$

where $x' = dx/dz$ and $x'' = dx/dz$. Assuming $x' \ll 1$, this later equation is simplified to

$$x'' \cong -\frac{1}{n} \cdot \frac{\partial n}{\partial z}x' + \frac{(1+x'^2)}{n} \cdot \frac{\partial n}{\partial x} \tag{4.25}$$

The differential equation can be solved using the Euler method implemented in Matlab. The input ray is normal to the device $(x'(z=0)=0)$. With a fixed step along O-z, the values of $n(x,z_i)$, $\frac{\partial}{\partial z}n(x,z_i)$, and $\frac{\partial}{\partial x}n(x,z_i)$ are approximated for each calculation step with a high order

polynomial (obtained after the data $n(x, z)$) to adjust these values to the lateral deviation of the ray. The coefficients A and B are obtained from these polynomials.

$$\begin{bmatrix} x' \\ x \end{bmatrix}' = \begin{bmatrix} A & 0 \\ 1 & 0 \end{bmatrix} \cdot \begin{bmatrix} x' \\ x \end{bmatrix} + \begin{bmatrix} B & 0 \\ 0 & 0 \end{bmatrix} \cdot \begin{bmatrix} x'^2 \\ x^2 \end{bmatrix} + \begin{bmatrix} B \\ 0 \end{bmatrix} \tag{4.26}$$

$$A = -\frac{1}{n} \cdot \frac{\partial n}{\partial z} \tag{4.27}$$

$$B = \frac{1}{n} \cdot \frac{\partial n}{\partial x} \tag{4.28}$$

This calculation is applied to planar-nematic devices, given that only one polarization is considered. Figure 4.4 shows the result of applying this calculation to the binary grating shown in Fig. 4.3a. The lateral gradient has been multiplied 10 times so that the deviation effect can be seen. The lateral gradients are not strong enough for our devices and straight propagation can be used to calculate the retardation in two and three-dimensional devices. This is mainly a consequence of the thickness of the liquid crystal layer, the reduced phase modulation, which is never higher than $2 \cdot \pi$, and the visco-elastic properties of liquid crystals that result in smooth transitions between highly distorted and undistorted local director profiles.

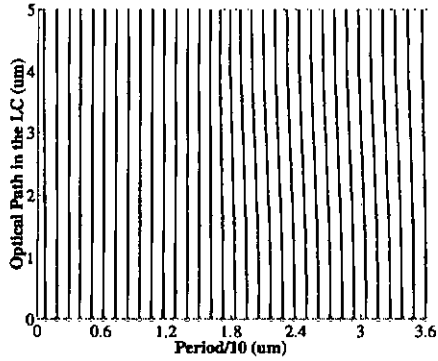

Figure 4.4: *Ray propagation through the binary grating period shown in Fig. 4.3a. Each ray starts at a circle for $z = 0$ and is expected to finish at a cross for $z = d$. The lateral gradients have been multiplied by 10 in order to see the deviation. The lateral gradient are very low and straightforward calculation is admitted.*

To have an idea of the lateral gradient limit allowing to use the straight propagation model, Eq. (4.25) is further simplified assuming that $\partial n/\partial z \ll 1$, which can be admitted for our thin,

high birefringent and weakly distorted cells. The equation is then roughly simplified to

$$x'' \cong \frac{1}{n} \cdot \frac{\partial n}{\partial x}, \tag{4.29}$$

which leads after integration and to

$$\delta = \frac{1}{2n} \cdot \frac{\partial n}{\partial x} \cdot z^2, \tag{4.30}$$

where δ is the lateral variation of the position. Having neglected the gradient along z means that the x component of the gradient is constant. Therefore, the maximal deviation is obtained when $\delta_{max} = \delta\,(z = d)$, and the limit gradient becomes

$$\left|\frac{\partial n}{\partial x}\right| < 2n\frac{\Delta x}{d^2}, \tag{4.31}$$

where $\Delta x = \delta_{max}$ is the width of the mesh in the simulation cell, d the thickness of the cell, λ the optical wavelength and n the refractive index. We can consider this gradient along x as a phase difference of the retardation between two neighbor columns, that is

$$\left|\frac{\Delta\varphi}{\Delta x}\right| = k \cdot d \cdot \left|\frac{\partial n}{\partial x}\right| < \frac{4\pi \cdot n \cdot \Delta x}{\lambda \cdot d}, \tag{4.32}$$

from where we can obtain the critical grid size

$$\Delta x < \sqrt{\frac{\Delta\varphi \cdot \lambda \cdot d}{4\pi \cdot n}}. \tag{4.33}$$

Using BL006 with a cell $6\ \mu m$ thick and $n(\lambda = 633\ nm) = 1.8$, a binary phase grating with $\Delta\varphi = \pi$ requires a grid size around $\Delta x \leq 0.725\ \mu m$, and a blazed grating with $\Delta\varphi = 2\pi$ requires $\Delta x \leq 1.03\ \mu m$. These results show clearly that the liquid crystal device used allow to calculate using Jones matrix method straightforward.

Another distinction made for diffraction gratings is the classification in thin and thick gratings. Thick gratings would require a rigorous approach for the calculation and diffraction. To distinguish whether a grating is thin or thick, we can use the criteria $Q' \cdot \gamma \leq 1$established by Gaylord & Moharam [56] with

$$\gamma = \frac{\pi \cdot \Delta\varepsilon \cdot d}{2 \cdot \lambda \cdot \sqrt{\varepsilon} \cdot \cos\theta} \tag{4.34}$$

$$Q' = \frac{2 \cdot \pi \cdot \lambda \cdot d}{\sqrt{\epsilon} \cdot \Lambda \cdot \cos\theta}. \tag{4.35}$$

Here, λ stands for the wavelength, Λ for the period, d for the thickness, θ for the incident angle and $\epsilon = n^2$. Using the distribution shown in Fig. 4.4a, with $d = 5\mu m$, $\Lambda = 25\mu m$, $\theta = 0$, $\lambda = 633nm$, $\epsilon = 3.08$ and $\Delta\epsilon = 0.16$, we obtain $Q' \cdot \gamma = 1.0125 \cdot 10^{-6}$. A simpler approach considering the angular-wavelength characteristics, uses the criteria $d/\Lambda \ll 10$ which is largely verified ($d/\Lambda = 0.2$).

We can conclude that our gratings can be considered as thin and the Jones matrix calculation accepted to reconstruct the phase profile after the director profile obtained by simulation.

4.4 4 x 4 matrix method

Jones matrix method is a fast and simple method to calculate transmission of the usual liquid crystal configurations. The improvements made concerning the oblique incidence renders this method very effective for LC-device design. Nevertheless, special configurations or more precise results require more precise and rigorous formulations. Berreman's formulation is a rigorous 4 x 4 matrix method derived from Maxwell equations in non-conductive media ($\sigma = \rho = 0$), ($\mu = 1$);

$$\text{rot}\,\mathbf{E} = \frac{\partial \mathbf{H}}{\partial t} \qquad \text{rot}\,\mathbf{H} = \frac{\partial \mathbf{O}}{\partial t} \qquad \mathbf{D} = \epsilon(z)\mathbf{E} \tag{4.36}$$

and $\epsilon\,(z)$ is the dielectric tensor describing the stratified media along z, the axis of stratification of the birefringent media.

Figure 4.5 shows the stratification of the media and the orientation of the electro-magnetic wave in the plane. The wave is therefore represented as a 4 component vector of the form [57, 47]

$$\psi = \begin{bmatrix} E_x \\ H_y \\ E_y \\ -H_x \end{bmatrix}. \tag{4.37}$$

The normal incidence allows to reduce the system of six equations resulting from Eqs. (4.36), to four. The system is then presented in the form

$$\frac{d\psi\,(z)}{dz} = i \cdot k_0 \cdot \Delta\,(z) \cdot \psi\,(z)\,, \tag{4.38}$$

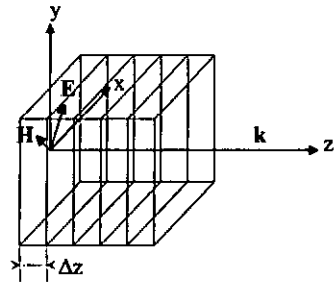

Figure 4.5: *Initial configuration for the Berreman representation of the normal incident electromagnetic wave* (E, H) *through a stratified media* $\Delta z = d/N$ *(d = thickness, N = number of strata).*

where

$$\Delta(z) = \begin{bmatrix} \Delta_{11} & \Delta_{12} & \Delta_{13} & 0 \\ \Delta_{21} & \Delta_{22} & \Delta_{23} & 0 \\ 0 & 0 & 0 & \Delta_{34} \\ \Delta_{41} & \Delta_{42} & \Delta_{43} & 0 \end{bmatrix} \tag{4.39}$$

is the matrix containing the parameters of the z-layer resulting from $\epsilon(z)$ [40, 41] . The coefficients Δ_{ij} assure also the tangential continuity of the fields at the interfaces . The difficulty is now to obtain a matrix P such that

$$\psi(z+h) = P(h) \cdot \psi(z) . \tag{4.40}$$

This matrix P is obtained from the expansion of .

$$P(h) = \exp(-j \cdot k_0 \cdot \Delta \cdot h) = \sum_{n=0}^{\infty} \frac{(-j \cdot k_0 \cdot h \cdot \Delta)^2}{n!} \tag{4.41}$$

using a third order approximation [57]

$$P(h) = \beta_0 \cdot I + \beta_1 \cdot \Delta + \beta_2 \cdot \Delta^2 + \beta_3 \cdot \Delta^3 + ... \tag{4.42}$$

For an inhomogeneous birefringent media, the matrix equation becomes

$$\psi(z+d) = P_n \cdot P_{n-1} \cdot ....P_2 \cdot P_1 \cdot \psi(z) \tag{4.43}$$

The layers of the stack must be thin enough to be considered as homogeneous and thus Δ independent of z within the considered layer. The final matrix $P(d) = \prod P_i$ describes the inhomogeneous birefringent media and it is possible to obtain the transmitted and reflected waves, from

$$\psi_{trans} = P(d) \cdot (\psi_{incident} + \psi_{reflected}) \tag{4.44}$$

Note that $P(d)$ is not reversible, i.e. the matrix describes the propagation in one sense. This is a consequence of the description of $\Delta(z)$ at the interfaces of the layers. Practically, for the small gradients of ε that occur in TN or STN cells, the coupling terms in P are so small that P is practically reversible. The 4×4 matrix can be decomposed in a sum of two 2×2 matrices. The forward propagation matrix is equivalent to the Jones matrix [58, 41]. This is not the case for large gradients, like those described by [59].

Figure 4.6a compares the calculation methods, i.e. 2×2 Jones matrix method, 4×4 Berreman matrix method and the analytical Gooch and Tarry approximation. The total extinction is practically identical for all methods, which is the most important consideration to obtain a high contrast ratio between the on and off state. Concerning the maximal transmission, the Gooch and Tarry formula gives the highest values, since it does not take account of the losses at the interfaces of the stratified model. This is done by the LCDMaster implementations of the 2×2 and 4×4 methods. While the 2×2 method only takes account of the losses, the 4×4 method considers the coupling of the forward and backward propagating waves. Figure 4.6b compares the 2×2 and 4×4 methods for a driven cell of optimized thickness.

4.5 Examples of optimization

4.5.1 Infrared TN-cell

With the tools presented, it is possible and quite easy to optimize a twisted nematic cell [60]. Our goal was to optimize a TN cell for monochromatic operation at the infrared wavelength of $1.55\ \mu m$, which is used for fiber optic communications. This is an uncommon wavelength for liquid crystals to operate, which are mainly used for white light or at least visible wavelengths. Indeed, LCDMaster only works with a spectrum between 380 nm and 780 nm. In addition, the documentation on liquid crystals does not contain the refractive index at $1.55\ \mu m$. Therefore, some calculation parameters have been changed in order to use LCDMaster for the calculations. To calculate with a wavelength included in the visible spectrum, the initial wavelength of 1550 nm is halved and 775 nm is used instead. By doing this division, any related geometrical param-

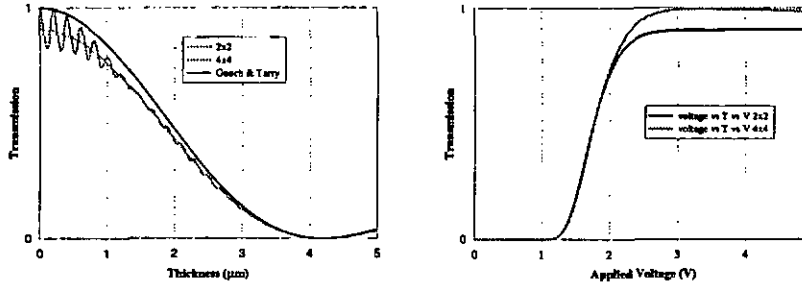

(a) (b)

Figure 4.6: *Transmission plots for TN cells using* 2×2, 4×4 *and Gooch and Tarry methods. a) Transmission vs. thickness for the stable configuration at 0 V. The optimal thickness is* 4.19 μm *b) Transmission vs. applied voltage for the optimized thickness. (LC: ZLI-2293@633nm, pre-tilt=2°,* Δn*=0.131)*

eters must be homothetically transformed to replicate the same conditions as the initial problem. Table 4.1 shows how these parameters and constants are modified.

parameter	physical unit	modified
λ	[m]	$\lambda/2$
K_{ii}	[N]	-
γ	[Pa.s]	$4 \cdot \gamma$
d	[m]	$d/2$
V	[V]	-
n	[]	-

Table 4.1: *Hamothetic modifications for the main parameters and constants of a cell.*

From the units of the parameters, one sees that the elastic constant K_{ii} are unchanged. This is different for the viscosity γ. Although is named rotational viscosity, the unit clearly shows an inverse square dependence to length units. The cell thickness d for calculation is also divided by 2, like the wavelength λ. In one-dimensional simulations, the voltage must not be changed since it appears to be directly proportional to the cell thickness d and inversely proportional to the distance between electrodes, also d, and therefore they compensate each other. Finally the refractive indexes n are not modified since the phase retardation is related to the ratio of thickness and wavelength d/λ, whose modifications compensate each other. However the birefringence at

1550 nm must be known. The 3-coefficient Cauchy approximation presented in Eq. (1.13), is used to extend the values from the visible to the infrared.

Thickness

The thickness of the device is calculated for the relaxed configuration and U = 0 V. We are looking for a device that performs a phase retardation of $(2m + 1) \cdot \pi$, which transforms the linear input polarization into a linear output polarization perpendicular to the initial one. Figure 4.7a shows the Stokes parameters of Eqs. (4.4) vs. the thickness obtained by simulation of a TN cell with liquid crystal ZLI-1565 at U = 0 V for a wavelength of 1550 nm. The output polarization state is perfectly linear, if $S_2 = S_3 = 0$. This occurs for a thickness of $11.95\ \mu m$. Figure 4.7b shows the Stokes parameters vs. the applied voltage of a cell of this thickness. The two operating points, relaxed and completely switched, are found at 0 V and 5 V, where both polarizations are practically linear. Since $S_3(V) \neq 0$, the linear polarization is not simply rotated but becomes slightly elliptic for the intermediate voltages, as shows Fig. 4.7c.

The operation mode is important, since it will determine the maximal contrast ratio, that is, the ratio of the transmission between the two operating points. The contrast ratio is highest when the transmission is lowest. Since the switched state is never perfectly homeotropic, there will be a residual ellipticity at the output. Thus, the only perfectly defined state, concerning the outcoming polarization state, it is the un-switched one (U = 0 V). The state of minimal transmission is then chosen to work in this mode, i.e. normally black (NB) with parallel polarizers. In this way the extinction is limited by the quality of the polarizers. High quality polarizing beam-splitters (PBS) can perform a contrast ratio of $CR = 10^5 = 50\ dB$.

Angular dependence of the contrast ration (CR)

The thickness optimization is valid for normal incidence. Since the birefringence of the liquid crystals depends on the incident angle, and the path is longer for oblique incidence, the transmission values will not be optimized anymore, thus reducing the efficiency of the device.

Figure 4.8 shows a iso-contrast simulation. The transmission of the two operating modes (0 V and 5 V) are calculated for different polar and azimuth angles of incidence. For each angle the contrast ratio is calculated and the lines of the contrast are plotted in the figure. The contrast ratio drops drastically when the incidence is not normal. Also, the cell is clearly not symmetrical when the azimuth angle is changed. Therefore, a bad alignment of the source has important consequences on the efficiency of the device.

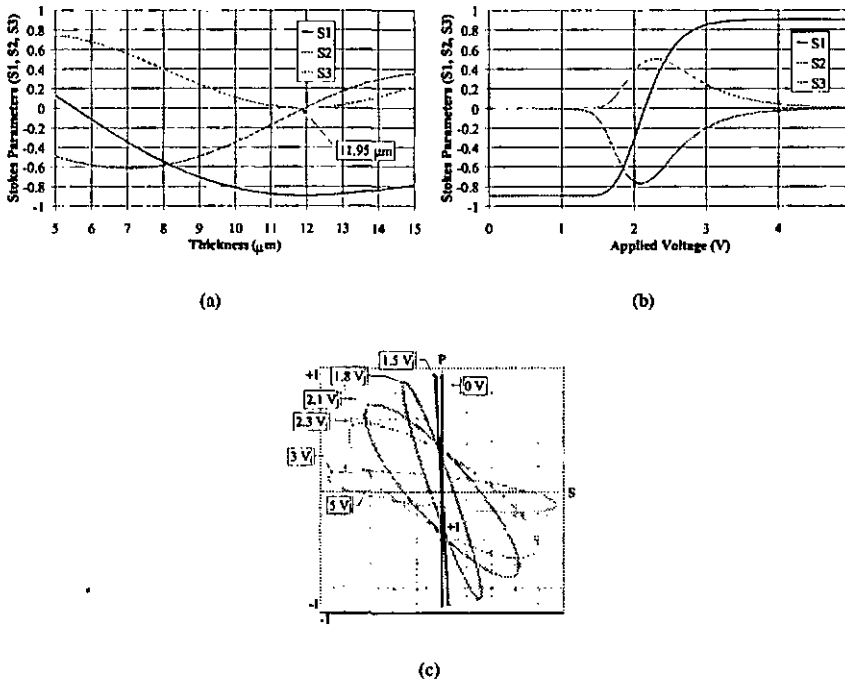

(a) (b)

(c)

Figure 4.7: *Simulation and optimization of a TN cell using the* 2×2 (Jones) matrix approach implemented in LCDMaster. *a) Stokes parameters* S_1, S_2 *and* S_3 *vs. thickness in the relaxed state* ($U = 0$ *V). The output is linearly polarized if* $S_2 = S_3 = 0$. *b) Stokes parameters vs. applied voltage for the cell of the ideal thickness* ($11.95\,\mu m$). *c) Polarization ellipses for different applied valtoges. (LC: ZLI-1565,* $\lambda = 1550$ *nm., pre-tilt* $= 2°$.)

4.5.2 Liquid crystal micro-lenses

Another situation where the liquid crystals directors are modulated laterally appears in micro-lenses. As shown in Fig. 4.9, arrays of lenses of $120\,\mu m$ in diameter are obtained using the pattern of the photolithographic mask (a), originally used for photo-resist micro-lenses (b)[61] as electrode pattern (c). The edge of the holes is responsible for fringing electric fields in the liquid crystal bulk. The tilt modulation is three-dimensional and is intended to obtain a spherical phase front modulation. The interest is to obtain a lens with variable focal length without any moving parts.

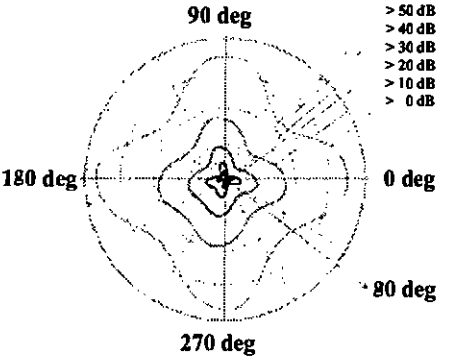

(a) Iso-contrast lines.

Figure 4.8: *Iso-contrast lines for the TN cell optimized for infrared operotion in Fig. 4.7.*

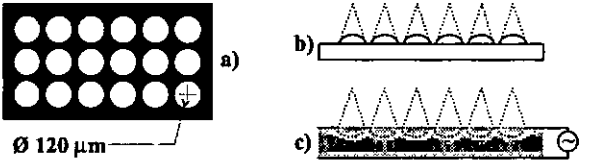

Figure 4.9: a) Schematic photolithographic mask used to fabricate photo-resist micro-lenses. b) Photo-resist micro-lenses array. c) Cross-section of a LC micro-lenses array.

Using three-dimensional simulations, the phase profile for different configuration, basically planar and homeotropic alignment, can be calculated [62]. From the practical point of view, the operating range is also of interest.

From the two configurations, only the homeotropic alignment has revolution symmetry. This means that this is the only configuration where the phase profile can be spheric. It also means that a cross section calculation is enough to calculate one cross-section. But on the other side, the directors are not aligned with the polarizer except for one orientation.

Planar alignment has not this problem with polarized light, but the director profile has no rotational symmetry. The deformation under applied voltage was already presented in Fig. 3.12. Parallel and perpendicular cross-sections, with respect to the alignment show very different di-

rector profiles.

The characteristic of these devices is its unusual thickness of some 50 μm. This large thickness results in several wavelengths of retardation within the liquid crystal. The index gradients in these cells, together with the effective thickness of the liquid crystal layer [51] could be enough to deviate the incident ray out of the considered liquid crystal column where Jones calculus is performed. Although the path is much longer than usual, the gradients are still too small to deviate the ray more than allowed. Still, the deviation is more important than with classical devices. Figure 4.10b shows the intensity distribution through crossed polarizers at 45° with respect to the alignment. The pattern is almost circular, but the asymmetries in the director field result in and a slightly shifted and elliptical pattern.

4.6 Summary

1. *Straight propagation can be considered.* In two- and three-dimensional devices, lateral gradients in thin layers ($< 10\ \mu m$) and low voltages ($< 5\ V$) are not strong enough.

2. *Jones matrix method is used in one-, two- and three-dimensional simulations.* This is allowed by the straight propagation proof. The director profiles of the simulations can be directly used for normal incidence.

3. *Phase profiles can be obtained after two- and three-dimensional simulations.* Using Jones matrix, the amplitude and phase retardation by the propagation through the liquid crystal device is calculated.

4. *Far-field propagation can be calculated.* With the phase profiles obtained before and with the Fraunhofer diffraction calculation, Fourier transformation gives the far-field diffraction image.

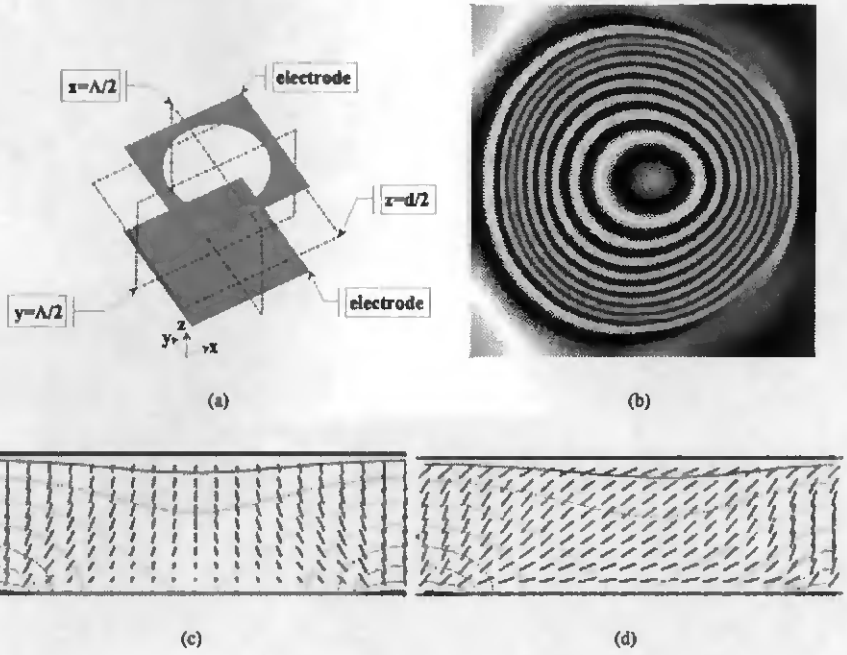

Figure 4.10: *Two cross-sections, parallel and perpendicular to the alignment. The directors and the equipotential lines are shown. a) Parallel cross-section of the simulation model. The deformation is not symmetrical respectively to the axis of the electrode. b) Perpendicular cross-section. The deformation is symmetric. c) Interference pattern of the lens function. The asymmetry is responsible for the shift of the pattern. Parameters: LC=BL006, U= 3 V, period* = 150 μm, *diameter* = 120 μm, *thickness* = 50 μm.

Chapter 5

Nematic binary phase gratings

5.1 Introduction

This chapter concerns planar nematic binary phase gratings. From the technological point of view, these are the simplest gratings to consider, since a single electrode with a comb-like structure in one of the substrates is enough to obtain a binary pattern in the liquid crystal layer.

Several other configurations are nevertheless possible. In additioo to the planar-oematic configuration [63] treated in this chapter, other possibilities have been considered. For example, an hybrid device, i.e. a micro-structured grating covered with a second substrate and filled with liquid crystal [23, 24]. This requires a good optimization of the phase shift through accurate control of the thickness and the phase retardation of the liquid crystal and the isotropic medium, to get high efficiency and contrast. The use of cholesteric mixtures with a pitch, such that the device is below the Maughin limit for the considered wavelength, is also interesting. Assuming that the wave undergoes a phase retardatioo corresponding to an averaged index of the liquid crystal whatever the input polarizatioo is, and that the micro-structure is isotropic, the cell could be considered polarization insensitive. When switched, the homeotropic configuration of the liquid crystal is also isotropic for normal incidence.

Polymer dispersed liquid crystals are also used for diffractive gratings. Holographic patterns are used for local polymerization, changing locally the density of liquid crystal [26]. Also, specific textures which result from special electric driving result in diffractive patterns [64, 65, 66]. In-plane electric fields from inter-digitated electrodes give also periodic modulation [67, 68].

Another interesting approach, which aims also to get polarization-insensitive devices, is based on multi-domain alignment [10, 69, 70]. Using rubbing technique or LPP [8], parallel strips with different alignment are produced in the liquid crystal layer, which results in neighbor

domains with mutually reverse twist. For short periods, and although the local domains are polarization sensitive, the far field diffraction pattern corresponds to polarization insensitive binary gratings. This configuration requires also optimization of the parameters.

5.2 General optical properties

Binary phase profile

A binary phase function is characterized by two levels of retardation

$$\begin{aligned} \varphi &= \varphi_0 \qquad 0 \le x < p \\ \varphi &= \varphi_0 + \Delta\varphi \quad p \le x < \Lambda \end{aligned} \qquad (p < \Lambda), \tag{5.1}$$

where Λ is the periodicity of the function, p is the position where the phase changes by $\Delta\varphi$ and φ_0 is the common phase retardation. Figure 5.1 illustrates a this binary phase function and its

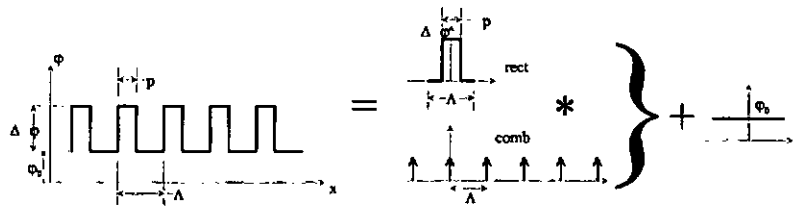

Figure 5.1: *Representation of a binary phase function ond its mathematicol representotion for Fourier transformation (the stor * stonds for convolution).*

decomposition in basic functions that can be easily be analyzed through Fourier transformation. For $p = \Lambda/2$, the phase function becomes

$$\varphi(x) = \varphi_0 + \Delta\varphi \cdot rect\left(\frac{2x}{\Lambda}\right) * comb(\frac{x}{\Lambda}) \tag{5.2}$$

and the Fraunhofer diffraction (Fourier Transformation FT) of the phase grating is obtained from [71]

$$\exp(i \cdot \varphi(x)) = \sum_{N=-\infty}^{\infty} A_N(\Delta\varphi) \exp(i \cdot N \cdot K \cdot x), \tag{5.3}$$

where $K = 2\pi/\Lambda$ and

$$A_N(\Delta\varphi) = sinc(\frac{N}{2}) \cdot \cos(N\frac{\pi}{2} + \frac{\Delta\varphi}{2}). \tag{5.4}$$

The far-field diffraction efficiency in a specific order N is then obtained from

$$\eta_N = |A_N|^2, \tag{5.5}$$

which yields

$$\eta_0 = \cos^2\left(\frac{\Delta\varphi}{2}\right) \qquad \eta_{2n+1} = \left(\frac{2}{\pi\,(2n+1)}\right)^2 \sin\left(\frac{\Delta\varphi}{2}\right) \qquad \eta_{2n} = 0. \tag{5.6}$$

In the case of a binary grating of duty cycle 50% ($p = \Lambda/2$) and $\Delta\varphi = \pi$, the zero order vanishes and light is only diffracted into the odd orders with the efficiency

$$\eta_{2n+1} = \left(\frac{2}{\pi\,(2n+1)}\right)^2 \tag{5.7}$$

The diffraction efficiency into the first orders is then $\eta_{\pm 1} = 40.53\%$, that is, 81% of the energy goes into the 1^{st} diffraction orders when the 0^{th} order vanishes. This case is illustrated in Fig. 5.2a.

Sinusoidal phase profile

Another type of grating which can easily be described is the sinusoidal phase grating. The phase function is then

$$\varphi\,(x) = \frac{\Delta\varphi}{2}\left(1 + \sin\left(2\pi\frac{x}{\Lambda}\right)\right), \tag{5.8}$$

with the period Λ and the amplitude $\Delta\varphi$ of the phase modulation.The Fraunhofer diffraction (FT) is obtained from [71]

$$\exp\left(i \cdot \frac{\Delta\varphi}{2} \sin\left(2\pi\frac{x}{\Lambda}\right)\right) = \sum_{N=-\infty}^{-\infty} J_N(\frac{\Delta\varphi}{2}) \cdot \exp\left(i \cdot N \cdot 2\pi\frac{x}{\Lambda}\right), \tag{5.9}$$

where J_N is the N^{th} order Bessel function. The diffraction efficiency in a specific order N becomes

$$\eta_N = J_N^2\left(\frac{\Delta\varphi}{2}\right). \tag{5.10}$$

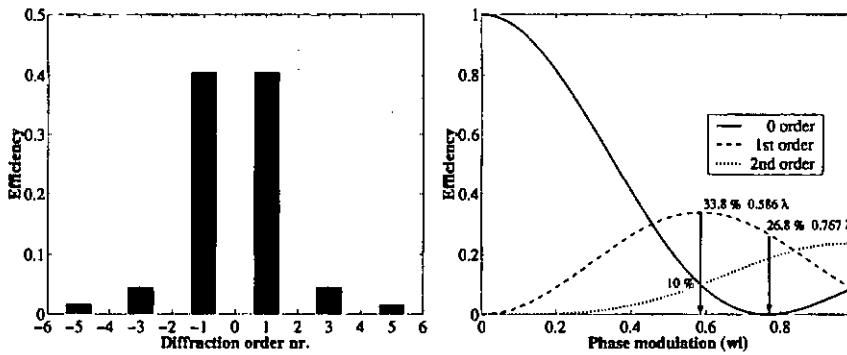

Figure 5.2: *Diffraction efficiencies of phase gratings. a) Binary phase grating with* $\Delta\varphi = \pi$ *and* $p = \frac{\Lambda}{2}$. *b) Zero,* 1^{st} *and* 2^{nd} *diffraction order of sinusoidal phase grating vs. modulation depth* $\Delta\varphi$.

Figure 5.2b shows the evolution of the 0^{th}, 1^{st} and 2^{nd} diffraction orders vs. the phase modulation amplitude $\Delta\varphi$. Compared with the binary grating in Fig. 5.2a, the maximal diffraction efficiency of the 1^{st} order and the extinction of the 0^{th} order do not occur for the same modulation. If the extinction of the 0^{th} is the goal, the efficiency of the 1^{st} order is only 26.8% instead of 33.8%, and the 2^{nd} is as high as 20%.

5.3 Simulated director profiles

Grating configuration

To produce a binary phase profile with nematic liquid crystals, two basic configurations with planar nematic arrangement are considered . Relative to the electrodes, the alignment can be either parallel or perpendicular, as shown in Fig. 5.3. These two arrangements should result in a local modulation of the director tilt angle only.

The input polarization must be parallel to the alignment direction. Maintaining the initial polarization state is desired, when the phase grating is part of a system including other polarization sensitive devices. Twisted configurations which might change the polarization or untwisted configurations which would become twisted during operation, are to be excluded.

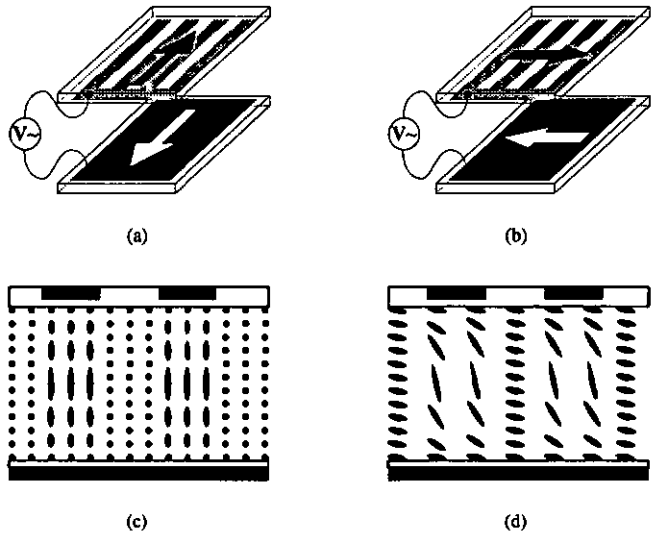

Figure 5.3: *Binary gratings with different alignment directions of the liquid crystal. (a) Parallel aligned grating and (b) perpendicular aligned grating rubbing directions. Spatial modulation of the directors for (c) parallel alignment and (d) perpendicular alignment.*

Alignment perpendicular to the electrodes

When a voltage is applied between the comb electrode and the counter-electrode shown in Fig. 5.3a, a vertical electrical field appears, which will increase the tilt angle of the directors between the electrode array and the counter-electrode, as shown in Fig. 5.3c. The difference $\Delta\varphi$ of the phase retardation is given by

$$\Delta\varphi = k \cdot d \cdot n_e - k \cdot \int n_{eff} \cdot dz. \tag{5.11}$$

This is the ideal case, but due to the elastic forces of the liquid crystal and the fringing fields appearing at the edges of the structured electrode, the director profile for the whole period is different. Figure 5.4a shows the parallel aligned cell as it appears in LCDMaster [22] after calculation. A single period with periodic boundary conditions is calculated, with the structured electrode at the top, and a full electrode at the bottom. The solid lines represent the equipotential lines. The dense equipotential lines close to the edges of the upper electrode indicate a very

strong electric field . The short sticks or dots represent the directors, tilt-modulated in the center of the cell and relaxed at the borders.

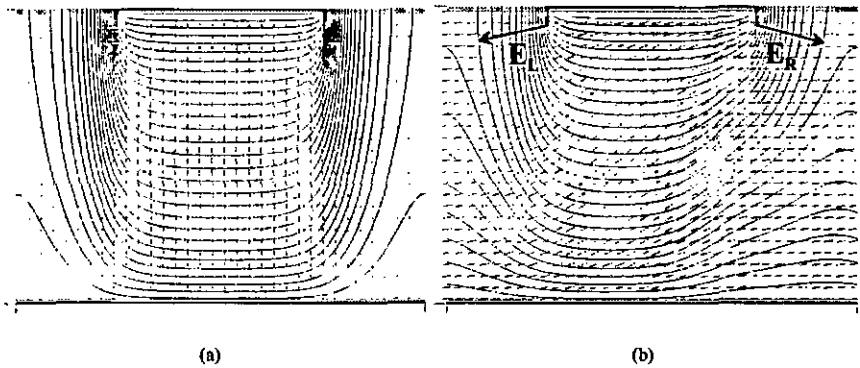

Figure 5.4: *Director simulations for (a) parallel and (b) perpendicular-aligned binary gratings. Periodic boundary conditions are imposed. The dark lines at the top and the bottom represent the electrodes, covered with a dielectric layer. The solid lines are the equipotential lines and the dots and sticks the directors. The width of the structured electrodes is half a period (see Fig. 5.5).*

Figure 5.5a shows how the tilt angle of the directors is modulated over a period and across the cell thickness. The modulated zone along the thickness can clearly be recognized in the center of the period, as well as the un-modulated zone at the extremities of the period. The main aspect characterizing nematic gratings is the transition between the modulated and the un-modulated zones. The Fig. 5.5a shows this smooth transition. The quality as binary grating will be mainly influenced by the relative width (respectively to the period) of this transition.

A second aspect characterizing this configuration is the appearance of twist modulation. As mentioned before, tilt-only modulation is required to maintain the same linear polarization at the output as at the input. Figure 5.5b shows that a twist modulation exists, although quite small ($< 10°$). The twist modulation is caused by the structure of the electrodes. At the edge, a strong horizontal fringing field appears, and the directors tend to align with it. Note that at any point of the cell, the electric field vector E is in the plane of the cross-section, while the director n is practically perpendicular to this plane. With the influence of the positive dielectric anisotropy, the oblique fringing fields are strong enough to initiate the twist re-orientation.

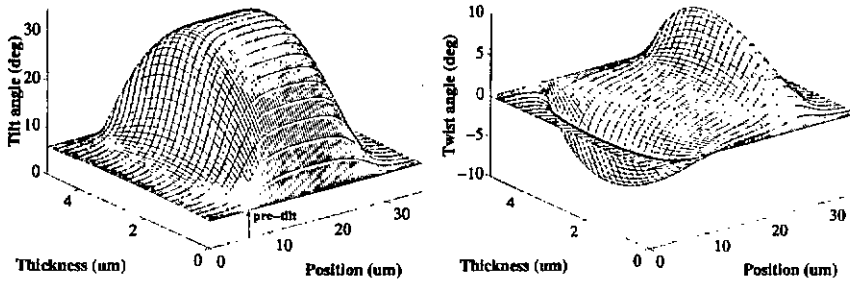

Figure 5.5: *Parallel alignment. a) Director tilt modulation for one period. b) Director twist distribution along the period and thickness.* ($U = 1.4\,V$, $p = 36\,\mu m$, $t = 4.6\,\mu m$, $pretilt = 6°$)

Alignment parallel to the electrodes

For this configuration, shown previously in Figs. 5.3b, the director and the electric field vector are in the same plane, thus no twist re-orientation will take place. But the fringing field is still present, inducing a perturbation of the director re-orientation locally. Figure 5.4b shows the simulated cell with perpendicular alignment. It appears clearly that the director profile is different compared with the perpendicular configuratioo (Fig. 5.4a) . The equipotential lines show an irregular distribution, quite different from the symmetric distribution of the parallel aligned configuration shown in Fig. 5.4a. The tilt distribution presented in Fig. 5.6a, shows also this asymmetry. The origin of this asymmetry is the fringing field together with the pre-tilt angle. Close to the upper electrode, the orientation of the electric field E (r) and the director n (r) are shown in Fig. 5.4b. On the left side of the upper electrode, the angle between the director n and the electric field E_L is quite small and the director will easily align with the field, rotating clockwise. On the opposite side of the electrode, the angle between E_R and the director is much larger and a anti-clockwise re-orientation is possible. Reverse tilt may occur, that is, a local value of the tilt angle smaller than the pre-tilt, as shown in Fig. 5.6b. The stress on each zone is unbalanced, and an asymmetric director profile results. In Fig. 5.6a, the complete director profile is shown. The asymmetry appears clearly together with a shift of the deformed pattern with respect to the center of the upper electrode.

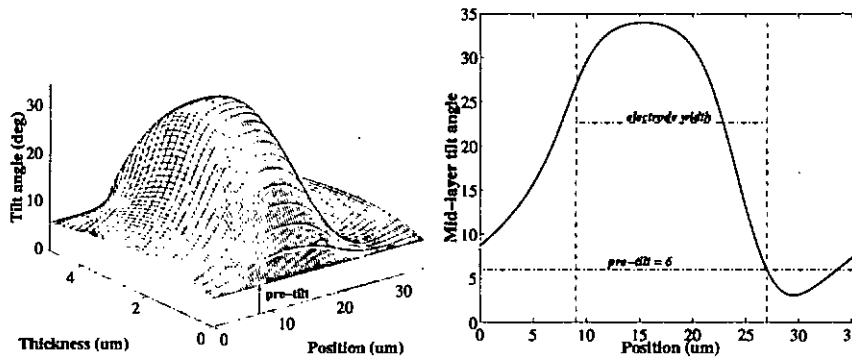

Figure 5.6: *Tilt modulation of the director for perpendicular alignment. a) Director tilt modulation for positive pre-tilt. b) Cross-section of the tilt distribution at half the cell thickness. The local stress and fringing field is responsible for the reverse tilt modulation. (same parameters as Fig. 5.5)*

5.4 Simulated phase profiles

With the tilt and twist distribution it is possible to calculate the phase profile. The use of the Jones matrix method appears to be appropriate for normal incidence. This is only true if the lateral index gradients are not large enough to deviate the beam out of the straight path. As shown in chapter 4, for these liquid crystal devices the transitions are smooth enough and the gradients small enough to accept Jones calculus.

For maximal efficiency, a binary phase profile is preferred to a sinusoidal one. But the elastic properties of nematic liquid crystals do not allow steep transitions. For a given cell thickness, period, and liquid crystal properties, the width of this transition is the same. Only for very short periods, these transition zones overlap and the required modulation is not reached. Figure 5.9 shows the profiles for parallel-aligned cells while Fig. 5.7 shows the results for perpendicular-alignment. The differences observed in the director profiles appear also in the phase profiles. Only parallel alignment shows a profile close to the desired binary profile, while perpendicular alignment shows an asymmetric phase profile. The periods of the different profiles have been normalized for comparison. The desired binary profile is practically obtained with long period, parallel aligned gratings, while a sinusoidal profile is obtained for shorter periods.

Perpendicular alignment

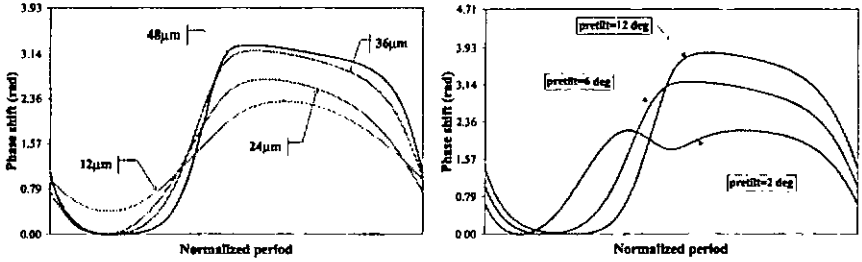

(a) (b)

Figure 5.7: *Perpendicular alignment phase profiles using Jones calculus obtained after the previously calculated director profiles a) For different period lengths.* ($thickness = 4.61\ \mu m$, $pretilt = 6°$, $U = 1.4\ V$, *except* $U = 1.9\ V$ *for* $12\ \mu m$ *period) b) For different pre-tilt angles.* ($period = 36\ \mu m$, $thickness = 4.61\ \mu m$, $pretilt = 12,\ 6\ \&\ 2°$, $U = 1.4\ V$).

Figure 5.7a shows that the phase profiles are clearly asymmetric. A possible remedy is to increase the pre-tilt angle. Figure 5.7b shows how the phase profile changes when the pre-tilt angle is changed. Lower pre-tilt result in the already mentioned reverse tilt, which causes an asymmetry in the director profile. With larger pre-tilt, the problem caused by the locally different orientation between the directors n and the electric field E discussed in Fig. 5.4b is reduced. The sense of rotation of the director is more clearly defined and the final director profile is closer to the symmetric profile desired for binary gratings.

Using the Fourier transform for periodic functions, the far field image (Fraunhofer diffraction) is calculated from the phase profiles, and the diffraction pattern is also asymmetric, as shown in Fig. 5.8b.

The asymmetric phase profile is responsible for the unbalanced diffraction pattern. From this point of view, perpendicular aligned gratings may have an advantage for some applications, for example for switchable blazed gratings.

Parallel alignment

As Fig. 5.9 shows, reducing the period changes the profile from almost binary to sinusoidal-like. The reduction of the period changes the form of the profile, but not the modulation depth,

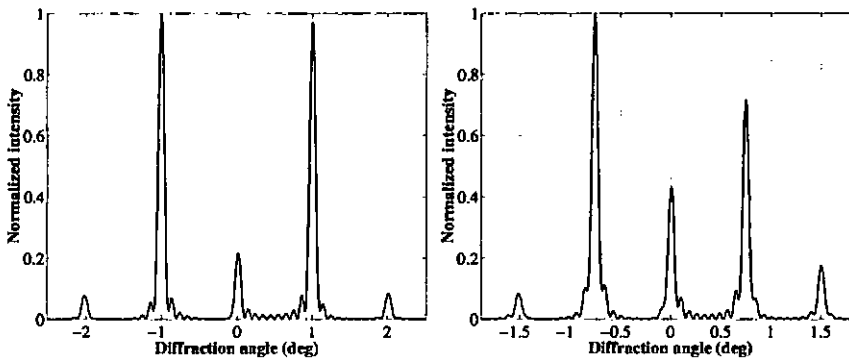

Figure 5.8: *Calculated far-field diffraction pattern for (a) parallel and (b) perpendicular-aligned gratings ($\Lambda = 36\ \mu m$, $\Delta\varphi = \pi$). The plots are normalized to the highest value.*

at least not until a critical period length is reached. When the period is further reduced, the director profile is modified over the whole period, that is, all the directors are tilt-modulated, thus resulting in a reduction of the modulation depth. Therefore, the voltage must be increased to reach π modulation ($\Lambda = 12\,\mu m$, $U = 1.9\,V$ in Fig. 5.9). Nevertheless, the voltage correction reaches a limit where it is no longer possible to reach the desired modulation depth. Note that the part of the phase function that links the high and low levels of retardation in the binary phase profile has a width (transition width) which is determined, for a given LC and the required voltage for π modulation, by the thickness of the cell. Since the period has been normalized in Fig. 5.9, these transitions do not look identical. Instead, the figure illustrates clearly how much this transition is important in the final shape of the phase function. When the critical period length is reached, the phase function is only composed of these transitions resulting in a sinusoidal-like phase profile.

In Fig. 5.10, the relation between the critical length for the period, the thickness and the required voltage is shown. With the assumption that the period is long enough, the required voltage for π modulation is calculated, as illustrates Fig. 5.10a. The curve has a asymptotic limit for very thick cells corresponding to the threshold voltage $V_{th} = \pi\sqrt{K/\varepsilon_0\Delta\varepsilon}$. Besides, a minimum thickness $d \geq \lambda/(2 \cdot \Delta n)$ is required. Figure 5.10b shows a linear relation between the thickness and the shortest period that performs π modulation for the voltages plotted in Fig.

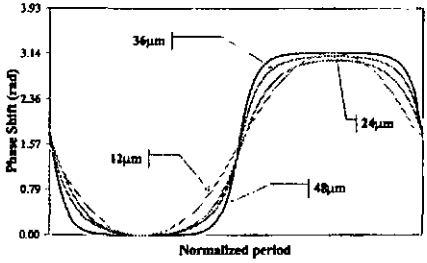

Figure 5.9: *Phase profiles for parallel aligned gratings using Jones calculus obtained after the previously calculated director profiles for different period lengths. (thickness* $= 4.61\ \mu m$, *pretilt* $= 6°$, $U = 1.4\ V$, *except* $U = 1.9\ V$ *for* $12\ \mu m$ *period).*

5.10a.

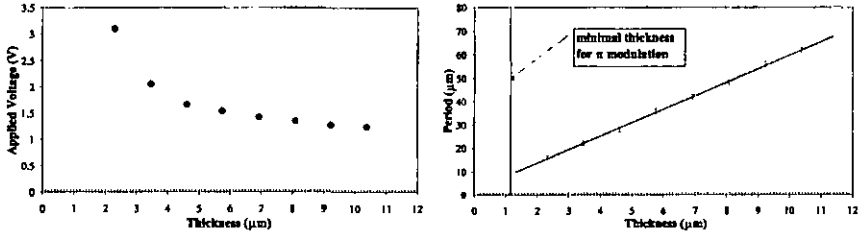

(a) (b)

Figure 5.10: *Calculation of the relations between thickness, voltage and critical period length for parallel-aligned gratings. a) For an uncritical period length, the voltage (U) required for* π *modulation vs. the cell thickness* d. *b) For the calculated thickness and voltage, the period length* Λ *is reduced until the modulation depth drops below* π. *This limit defines the critical period length.* ($pretilt = 6°$).

Using the Fourier transformation integral

$$A_N = \frac{1}{\Lambda}\int_{\Lambda} A(x)\cdot\exp\left(i\cdot\varphi(x)\right)\cdot\exp\left(-i\cdot\frac{2\pi\cdot x\cdot N}{\Lambda}\right)\cdot dx \qquad (5.12)$$

to calculate the amplitude of the N^{th} order diffraction in the far-field (Fraunhofer), the efficiency $\eta_N = |A_N|^2$ can be calculated numerically. The equation is used to calculate the diffraction

efficiency into the 1^{st} order ($N = 1$) for the phase profiles $\varphi(x)$. The profiles are obtained for a fixed thickness, and the corresponding voltage for π modulation. The plot labeled "U = 1.4 V" in Fig. 5.11 shows how the efficiency at constant voltage is reduced for shorter periods. Longer periods show an asymptotic efficiency towards the theoretical limit ($\simeq 40.5\,\%$) for binary gratings. Smaller periods change both the shape and, below the critical period length, also the modulation depth.

The second curve, labeled "optimized $\Delta\varphi$", shows the maximum efficiency possible for optimized modulation depth. The same director profiles have been used but the modulation depth of the phase profiles has been corrected to obtain the highest efficiency. The modulation must be increased for shorter, sinusoidal-like gratings, from the initial π modulation for binary phase gratings to $1.17 \cdot \pi$ for sinusoidal phase gratings.

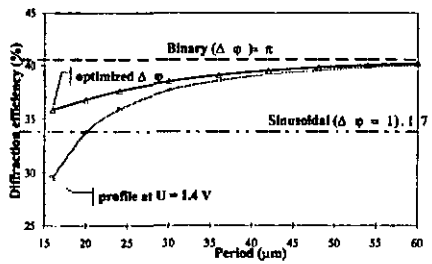

Figure 5.11: *Diffraction efficiency into the first order for parallel aligned cells using the values for U, d and Λ shown in Fig. 5.10.*

From the calculated phase profiles, the Fraunhofer diffraction pattern can be calculated using Fourier transform. The grating is assumed to be a thin element which modulates amplitude and phase. Figure 5.8a shows a typical diffraction pattern in the far-field for the calculated parallel aligned profiles. The modulation depth is π, but the zero order does not vanish, which means that the phase profile is not rectangular, but something between rectangular and sinusoidal. For the difference of the rectangular and sinusoidal phase grating see Fig. 5.2.

5.5 Experimental results

Cell fabrication

The gratings which have been realized are 6 μm thick, with periods of 24 μm, 36 μm and 48 μm (diffraction angles of 1.5^o, 1^o and 0.75^o at 633 nm) For this feature size ($> 12\ \mu m$), wet etching is used to structure the electrodes. PI 2545 or SN-70XX polyimides is spin-coated as alignment layer. The substrates are velour-rubbed and spherical spacers are used for thickness determination. The cells are driven with square signals of 1 kHz frequency.

Under this conditions, the cells are not critical in the sense described in section 5.4. The amplitude of the driving signal must not be corrected and is the same for all period lengths.

Experimental setup

Figure 5.12 shows the experimental set-up for the measurement of the diffraction patterns. The incident laser beam is spatially-filtered and an expanded plane wavefront is obtained with a collimating lens. The light is linear polarized with a high quality polarizer ($Contrast - Ratio > 10^5$), and the polarization plane is set parallel to the alignment of the liquid crystal in the cell. The incidence is normal to the substrate.

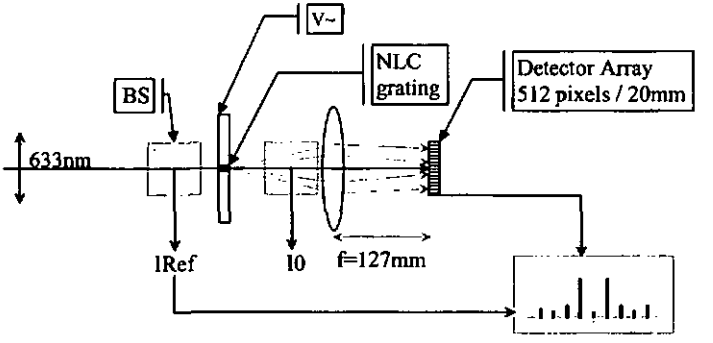

Figure 5.12: *Experimental setup for the measurement of diffraction patterns and efficiency.*

Perpendicular-aligned cells

The previous results with the calculated profiles already announced that the diffraction patterns will be asymmetric. The measured diffraction pattern is shown in Fig. 5.13a. Compared with the

calculated diffraction pattern in Fig. 5.8b, the shapes are qualitatively identical.

A more important aspect to point out is the behavior of the different diffraction orders as a function of the applied voltage. Figure 5.13b shows the measured efficiencies for the zero, $\pm 1^{st}$ and $\pm 2^{nd}$ order diffraction. The intensity of the zero order decreases smoothly and does not vanish in the considered range of voltages. The behavior of the $+1^{st}$ and -1^{st} orders is asymmetric as expected from the phase profile. Even considered as blazed grating, and considering the extinction of the zero order and a high contrast ratio between the selected order and the zero order as criteria, there is no optimized operating point in the considered voltage range. Although this grating is not efficient as blazed grating, the configuration shows great potential for multi-electrode blazed gratings, because of the smoother transition between the electrodes, compared to parallel aligned gratings.

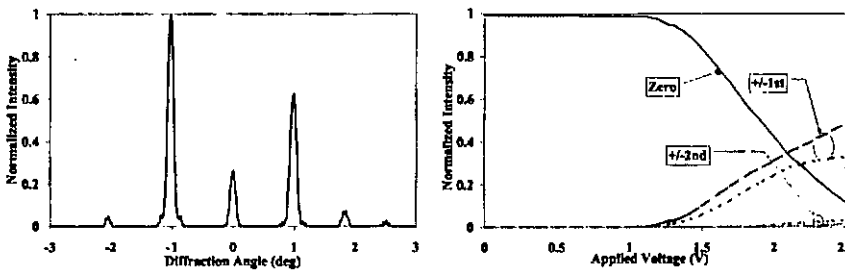

(a) (b)

Figure 5.13: *Perpendicular-aligned cells* ($\Lambda = 36\ \mu m$, $d = 6\ \mu m$). *a) Diffraction pattern for* $U = 1.5\ V$. *b) Measured intensities of the* 0, 1^{st} *and* 2^{nd} *diffraction orders vs. applied voltage.*

Parallel-aligned cells

Figure 5.14 shows the measured diffraction pattern and the diffraction intensities of the principal diffraction orders vs. applied voltage. Figure 5.14a shows a diffraction pattern where the zero order does nearly vanish. As predicted by the theoretical calculations and simulations in section 5.4, the diffraction pattern is symmetrical.

The measured intensities of the orders versus the applied voltage is shown in Fig. 5.14b. The diffraction for positive and negative orders is always the same. Also, a second operating point exists, where the 0^{th} order is again maximal and the 1^{st} vanishes. This corresponds to a

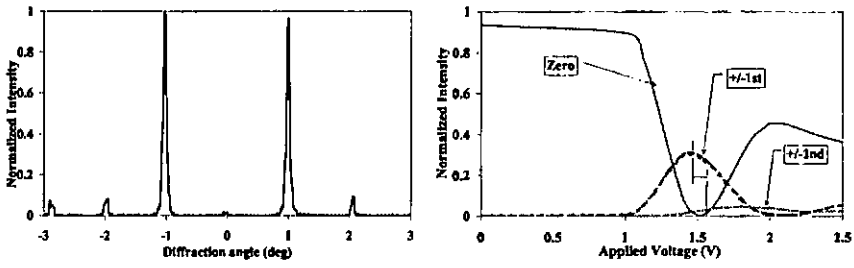

(a) (b)

Figure 5.14: *Parallel-aligned cell with* $\Lambda = 36\ \mu m$ *and* $d = 6\ \mu m$. *a) Diffraction pattern for best* 0^{th} *order extinction* ($U = 1.5\ V$). *b) Evolution of the* 0, 1^{st} *and* 2^{nd} *diffraction orders vs. the applied voltage.*

binary grating with a modulation depth of 2π, which is theoretically equivalent to no grating at all. The interest of this second operating point, although less efficient (50% of loss), is that this configuration has more elastic energy stored and would result in faster commutation through relaxation.

The second and most important aspect to point out is the difference in the required voltage for zero order extinction and maximal diffraction into the first order, observed in Fig. 5.14b. The same behavior appears in the theoretical efficiency plot for sinusoidal gratings (Fig. 5.2). Since high diffraction angle is preferred, the trend goes to shorter periods and more sinusoidal-like gratings. If contrast is the criteria, it is better to choose the best extinction voltage.

An additional perturbation comes from the amplitude grating produced by the refractive index difference between glass and the ITO of the structured electrodes. In this case, two gratings of the same period are superposed. For an amplitude grating, the $+1^{st}$ and -1^{st} diffraction orders have the same sign, contrary to a phase grating, for which they have opposite sign (see Eqs. (5.4) and (5.9)). Therefore the sum results in an asymmetric diffraction pattern. Nevertheless, the amplitude grating has only a small effect and can practically be neglected.

5.6 Alternative configurations for binary gratings

Hybrid liquid crystal grating

Using the ribs technology it is possible to create binary gratings as shown in Fig. 5.15. The ribs made with photo-resist are isotropic and the phase retardation is fixed. Between the ribs, the liquid crystal can have different configurations, i.e. planar-nematic, homeotropic, twisted-nematic or cholesteric. Nematic phases are not so interesting, given that they require linear polarization to be used. Instead, cholesteric phases below the Maughin limit could be of great interest to eliminate the entrance polarizer. The cholesteric phase can be used in this sense for wavelengths longer than the upper limit of the reflective window (see chapter 4).

The main problem appears at the new boundaries, introduced by the rib walls. There is no defined alignment at these surfaces and, if the alignment occurs in a manner opposed to the relaxed state, usually determined by the upper and lower boundaries, this state will be perturbed and the efficiency of the device would be strongly reduced.

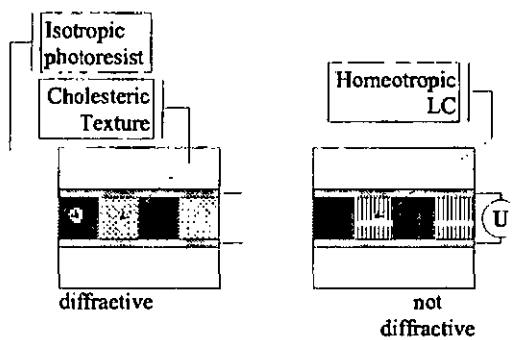

Figure 5.15: *Operation scheme for the hybrid binary grating with ribs and cholesteric texture.*

A second problem appears, when working below the Maughin limit. In twisted or super-twisted nematic cells, the linear polarization is intended to follow the helix of the liquid crystal and remains linear, changing only the orientation. Now, the polarization state is undetermined and the phase retardation is directly related to the thickness and an averaged refractive index. This means that precise thickness control is required for efficient operation of the grating. Since cholesteric textures are bistable, there is no possibility to electrically adjust the two operation states.

Figure 5.15 describes the two operation modes. When the cholesteric helix is present, the

phase retardation of the LC is different with respect to the retardation of the rib. This causes the binary phase grating. When the voltage is applied, the LC is homeotropic. The retardation is the same as the one of the ribs.

5.7 Summary

1. *The relative alignment between the electrode and the aligned directors has a fundamental effect on the director's arrangement.* Planar NLC binary gratings with an alignment parallel or perpendicular to the structured electrode do not give the same director profile.

2. *Only parallel-aligned gratings give binary-like phase profiles.* The shape of the phase profile changes from almost binary to sinusoidal-like when the period of the grating is reduced.

3. *The resolution limit, called critical period length, is linearly proportional to the thickness.* Below this limit, the phase modulation drops without correction of the applied voltage.

4. *The measured gratings prove the accuracy of the calculations.*

Chapter 6

Tunable phase gratings using multiple electrodes

6.1 Introduction

In this chapter, phase modulators with tunable phase profiles will be discussed. This is the logical way to follow after the binary gratings discussed in chapter 5. Most of the properties of multilevel gratings are logical consequences of the results obtained with binary gratings. Nevertheless, the characteristics desired for binary gratings are in general opposed to those of the tunable gratings considered here, i.e. blazed gratings.

The interest of tunable phase gratings is obvious. The same functions as made by lenses [72, 73] or prisms [74, 75] can be produced and corrected electrically. Even more complex modifications of the phase-front of a wave is possible, leading finally to a tunable hologram.

We will focus on blazed gratings. The goal of such a phase function is to deviate a beam by a certain angle as a prism does. This is done through diffraction instead of refraction. Figures 6.1 shows how the refractive prism can be replaced by a diffractive liquid crystal grating. The solid prism of Fig. 6.1a can be replaced by a solid blazed grating by making slices with a thickness of one wavelength, at least for monochromatic applications. The micro-prisms of the blazed gratings represented in Fig. 6.1b are difficult to fabricate, so they are replaced by a staircase using photolithographic processes. The efficiency of the staircase grating shown in Fig. 6.1c is related to the number of steps. The steps of the staircase can now be replaced by parallel electrodes with different voltages that will spatially modulate the liquid crystal and to obtain a phase modulation like the one illustrated in Fig. 6.1d.

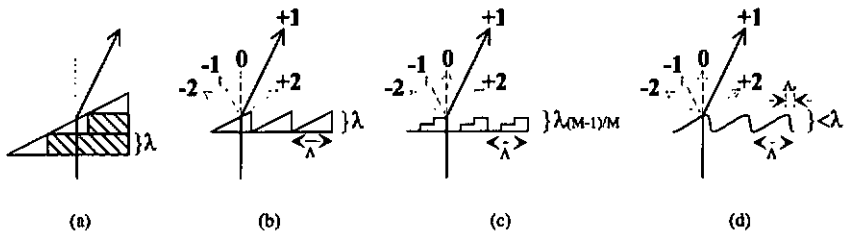

Figure 6.1: *Evalution from the refractive prism to the diffrative liquid crystal grating. a) Solid refractive prism. b) Ideal diffractive blazed grating. c) Staircase profile. d) Liquid crystal tunable grating.*

6.2 Simulated Electric Field and Director distributions

6.2.1 General description of the multilevel phase modulator

Figure 6.2 shows a cross section of the multilevel phase modulator. Parallel electrodes can be electrically driven with different voltages, V_1, V_2...V_m. The resulting electric field between these eloctrodes (V_i) and the counter-electrode (V_0) reduces locally the phase retardation by increasing the tilt angle of the underlying directors of the planar-aligned nematic liquid crystal.

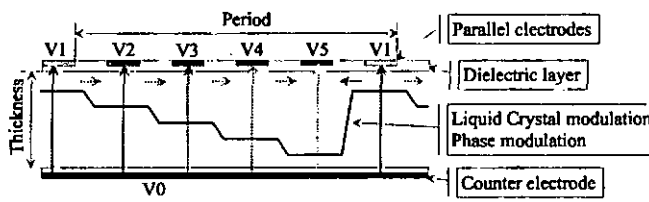

Figure 6.2: *Cross-section of a multilevel, periodic, liquid crystal grating. The different vertical fields created by the discrete electrodes are represented by the long vertical arrows. Also, horizontal fields appear between the discrete electrodes caused by the different applied voltages, in addition to the fringing fields of the discrete electrodes (see chapter 5).*

As for the binary gratings in chapter 5, two main configurations for planar-aligned nematic liquid crystal are possible in order to perform tilt modulation only. The alignment is either parallel or perpendicular to the electrodes. The device is polarization dependent. The input beam is assumed to be linearly polarized, parallel to the alignment of the director.

As it was already the case for the binary gratings, there are some side-effects that modify the expected performances of these devices. The fringing electric fields that appear at the edges of the electrodes of the binary gratings (chapter 5) are now re-enforced by the presence of the different applied voltages to the array of the electrodes. In addition, the pre-tilt angle will play an important role in the director re-arrangement, specially in the case of perpendicular-aligned devices.

6.2.2 Electric field distribution

For an easy manipulation of the blazed grating, a linear dependence of the phase shift as a function of the applied voltage would be ideal. This linear domain should have a dynamic range of 2π resulting in a minimum value for the thickness d imposed by the condition $d \cdot \Delta n/\lambda \geq 1$. Figure 6.3 shows the retardation vs. applied voltage of BL006 for $d = 6\ \mu m$ and different pre-tilt angles. The large birefringence ($\Delta n(633\ nm) = 0.28$) of this liquid crystal results in a modulation range of more than two wavelengths at 633nm. Increasing the pre-tilt angle has two consequences. First, the threshold voltage, clearly present for 0^o pre-tilt, is slightly reduced for small pre-tilt angles ($< 5^0$) and becomes undefined for larger pre-tilt angles. Also, the slope of the curves becomes smoother at small voltages.

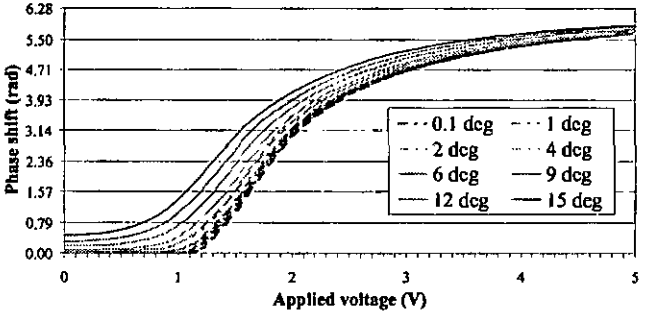

Figure 6.3: *Mid-layer tilt angle vs. applied voltage. (1D simulation, 50 layers, LC: BL006)*

The results obtained with one dimensional simulations, like those of Fig. 6.3, cannot be directly applied to gratings of high spatial frequency, since other constraints apply to the liquid crystal. The small electrodes and distances in between, together with the different voltages applied, result in an irregular reorientation of the molecules, and not only in a vertical reorientation caused by the vertical electric field. The electric field distribution is far more complex; the

electric fields from the different electrodes overlap. The main contributions to this director distribution of the nematic liquid crystal are: the liquid crystal dielectric and elastic properties, the cell thickness, the width and separation of the electrodes, the dielectric constant and thickness of the alignment layer [76], and finally the applied voltage. The last three aspects are of special importance for the multi-electrode gratings we are discussing.

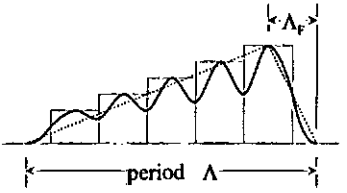

Figure 6.4: *The staircase profile of voltages applied to the electrodes becomes a smooth electrical profile in the liquid crystal.*

For the binary gratings (see chapter 5), the lower limit for the period length is determined by the extension of the fringing field beyond the lateral limits of the structured electrodes. While for binary gratings the overlap of fringing field should be avoided in order to obtain steep phase steps, for multilevel gratings overlap may be desired instead, in order to get smoother and more continuous transition between the electrodes, leading to a ramp instead of a staircase profile. On the other hand, a steep phase jump is required at the end of the period to obtain a high efficiency as blazed gratings. Figure 6.4 shows the different aspects discussed above. The closeness of the electrodes results in a smooth profile (solid line) which is close to a ramp with fly-back (dotted line).

To obtain a smooth ramp, thicker cells would be preferred. But due to the strong dependence between switching time and thickness ($\tau \propto d^2$), a better solution is to put the electrodes as close as possible together, than making a thick cell. The distance between electrodes is limited by the technological process (dry-etching), which is about 3 μm in our case.

Finally, small grating periods are required to perform large diffraction angles, with calls for small electrodes, going to the limit of the available technology. With such small structures the field distribution is mainly given by the overlap of the fringing fields. The resulting phase profiles will be smooth curves, very different from the staircase profile of Fig. 6.1c.

In-plane field

The Figs. 6.5 and 6.8 show that the main component of the electric field resulting from the potential lines is vertical. But they also show that a horizontal component of the field exists, specially close to and between the electrodes. The narrow field lines between the electrodes result in a very strong in-plane field, as illustrated by Fig. 6.6. This effect is specially important for parallel alignment. In the mid-layer, the field distribution is quite smooth and close to the desired blazed profile.

The in-plane effect has been studied in the mid-nineties to obtain better optical properties for commercial displays [77, 78, 79, 80, 27], but in our case this effect is undesired. Depending on the type of alignment considered, i.e. parallel or perpendicular to the electrodes, the effect is different.

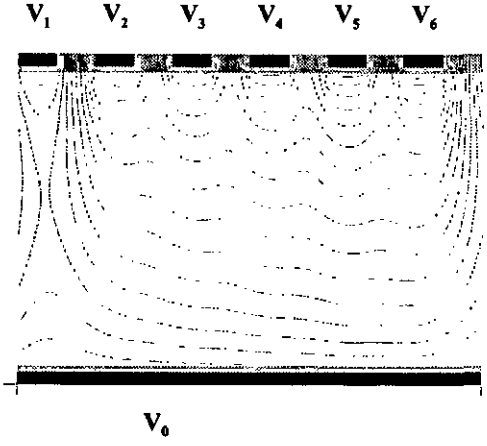

Figure 6.5: *Electric field profile for parallel aligned LC over one period of the grating. (6 level, electrode width and spacement = 3 μm, alignment layer thickness = 0.125 μm, cell thickness = 6 μm, BL006, $\Delta\varepsilon$ = 2.9, Voltages = 0, 1.7, 1.825, 1.975, 2.15 and 2.4 V.*

Parallel alignment

In the vicinity of the inter-electrode space, the electric field and the director is practically perpendicular. This means that if the electric field is strong enough, the director can be twisted. This reorientation is in conflict with the desirod tilt modulation, but occurs only close to the structured

substrate. Following Eqs. (3.15) and (3.19) of chapter 3, we know that the twist reorientation does not occur before a certain threshold voltage is reached. This threshold voltage [78] is given by,

$$V_{threshold}^{in-plane} = \pi \frac{l}{d} \sqrt{\frac{K_{22}}{\Delta\varepsilon \cdot \varepsilon_o}}, \tag{6.1}$$

where d is the cell thickness and l the distance between neighbor electrodes. Using BL006, with $K_{22} = 15\ pN$ and $\Delta\varepsilon = 17.3$, and $l = 3\ \mu m$, the threshold voltage for cells with a thickness $d = 6\ \mu m$ gets, $V_{th} \simeq 0.49\ V$. On the other hand, the threshold voltage for tilt modulation can be estimated by replacing K_{22} with K_{11} in Eq. (6.1). In this case, the distance l between electrodes is equal to the thickness d, which gives

$$V_{threshold}^{vertical} = \pi \sqrt{\frac{K_{11}}{\Delta\varepsilon \cdot \varepsilon_o}}. \tag{6.2}$$

With $K_{11} = 17.9\ pN$, Eq. (6.2) yields $V_{th} \simeq 1.1\ V$, which is close to the value shown in Fig. 6.3. Therefore, to obtain a smooth profile, the voltage difference between consecutive electrodes has to be small. For example, a high number of electrodes results in a smooth profile, since the highest voltage applied is the one required for 2π modulation and therefore independent of the number of electrodes.

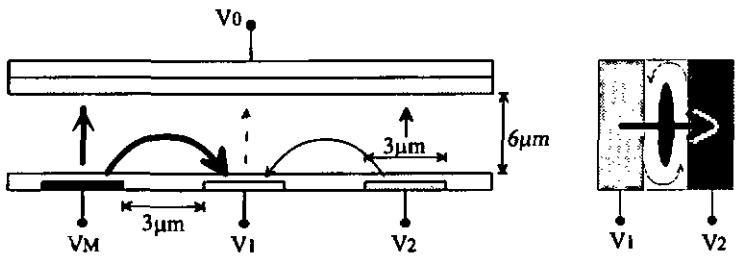

Figure 6.6: *The electrodes with the highest (V_M) and lowest (V_1) applied voltages produce a zone of high in-plane field. Also, the sense of field is reversed ($V_M > V_2 > V_1 \geq V_0 = 0$). For parallel or oblique alignment, the liquid crystal is twisted* [77].

As shown in Fig. 6.6, the first electrode (V_1) with the lowest applied voltage is the critical one concerning the in-plane field, . Usually at the same voltage as the counter-electrode, i.e. $V_0 = V_1 = 0$, it is neighbored by two electrodes with much higher voltages. V_M has the highest voltage ($\sim 2.5\ V$) and V_2 must be above the vertical threshold voltage ($> 1.1\ V$). Thus, the resulting in-plane field with V_1 is clearly above the calculated threshold of $0.5\ V$. For the other

electrodes ($V_3, V_4 ....V_{M-1}$), the in-plane field will depend on the number of electrodes M per period.

For small and closely spaced electrodes, it is no longer possible to think in terms of isolated electrodes, since the electric field of one electrode influences also its neighbor electrodes. The only solution to reduce the in-plane effect is to enlarge the electrodes, since thicker cells are excluded because they slow down the device. With a larger electrode it would be possible to increase the voltage of V_1 (usually set to 0 V) to a value below the vertical threshold, so that it does not modifies the directors but reduces the in-plane fields caused by $V_2 - V_1$ and $V_1 - V_M$.

Perpendicular Alignment

In this case, both the in-plane field and the director are practically parallel and in the cross-section plane shown in Fig. 6.7a. Thus, there is no danger of twist. Although in this case the in-plane electric field would keep the directors flat, and being a K_{33} dependent phenomena, the threshold voltage is extremely high. The in-plane field has practically no effect, as shows the absence of deep valleys in the equi-potential lines of Figs. 6.8a and b compared to those in Fig. 6.5.

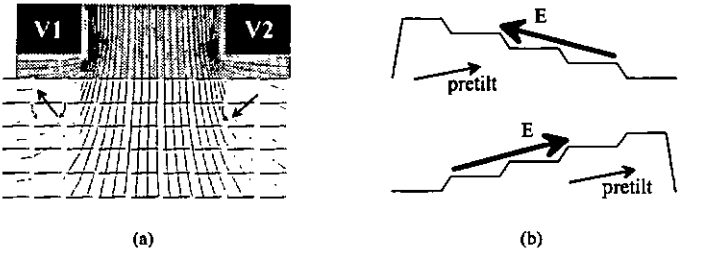

Figure 6.7: *The reverse tilt is caused by small pre-tilt and the fringing field. a) The relative orientation of the directors towards the local electric fields is different close to the edges of the electrodes. b) The sense of the voltage ramp and the direction of the pre-tilt will change the field distribution of perpendicular-aligned gratings as shown in Fig. 6.8.*

Already in the case of binary gratings, the reorientation of the directors was not the same on the two sides of the structured electrode. The relative orientation of the initial director and the local electric field is different, as shown in Fig. 6.7a. In the case of a staircase voltage profile, the pre-tilt can be either in the sense of the staircase or against it, as illustrates Fig. 6.7b. This small difference has strong consequences in the equilibrium state, as can be seen from the comparison of the equipotential lines in Figs. 6.8a and b.

The ideal solution would be a pre-tilt of zero. Practically, this is not feasible because of the uncertainty of the director reorientation. Being perpendicular to the electric field, the sense of the reorientation is not pre-determined and can be different on different periods. In the ideal, simulated case, either the algorithm does not obtain a equilibrium state or a disclination takes place because of the local fringing fields as occurred in low pre-tilt binary gratings. This same behavior was found in binary gratings, where reverse tilt occurs (see chapter 5).

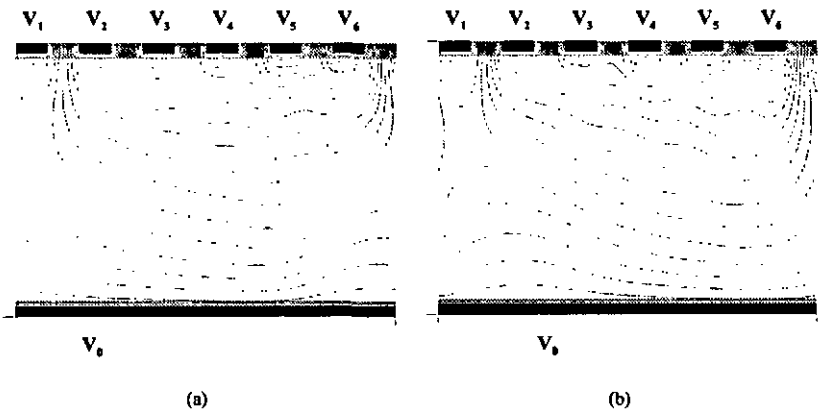

Figure 6.8: *Electric field profile for perpendicular aligned LC over one period of the grating. a) Positive pre-tilt. b) Negative pre-tilt. Same simulation conditions as Fig. 6.5.*

6.2.3 Director profile

Figures 6.9 and 6.10 show the tilt and twist angles of the director after reorientation resulting from the electric field distributions shown in Figs. 6.5 and 6.8. Although the devices are identical concerning the geometrical aspects (thicknesses, electrode width and spacing, pre-tilt angle, etc...) and the driving parameters (V_i values, frequency), the alignment direction, parallel or perpendicular to the electrodes, makes the difference. And, as mentioned before, the pre-tilt angle also differentiates the reorientation in the case of perpendicular alignment.

Parallel alignment

Figure 6.9a shows how the tilt profile reminds of the staircase profile, even if the electrodes are as close as possible. A thicker cell would smooth out the valleys in the tilt profile. The short

distance between the electrodes and the elastic behavior of the liquid crystal are responsible for the slight reorientation of the tilt angle at the beginning of the period, although the appliod voltage is zero at this first electrode.

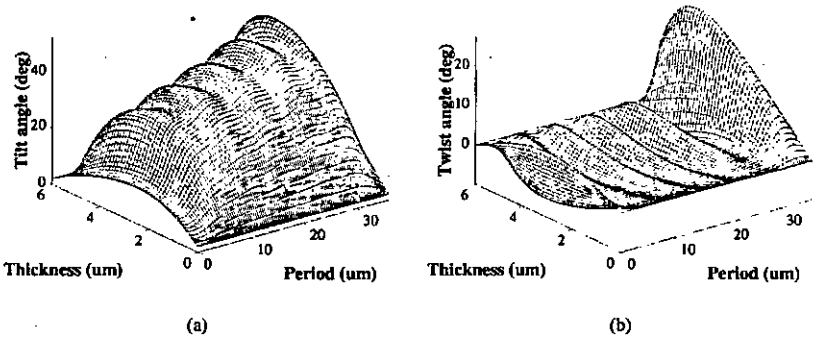

Figure 6.9: *Director profiles for planar-aligned liquid crystals resulting from the same simulation as Fig. 6.5. Although the applied voltages are the same, the resulting director distribution is quite different. This configuration shows an important high frequency undulation in the tilt distribution and the existence of twist modulation.*

But the twist is more important for parallel alignment. Figure 6.9b shows how the large in-plane fields can result in a twist angle rotation of 20°, while fringing fields in binary gratings caused only twist variations of less than 10° . This is, in fact, what happens between the other electrodes, since the voltage difference is quite low and the in-plane fields below the in-plane threshold voltage. The sense of the twist rotation is imposed by the intensity of the applied voltages, that is, by the local tilt gradients. As shows Fig. 6.9b, the maximal twist angle is negative between the intermediate electrodes but positive between the last and first electrode of a period.

In all cases shown in Figs. 6.9 and 6.10 both the valleys in the tilt modulation and the peaks in the twist modulation are closer to the structured substrate than to the counter-electrode. The use of two structured electrodes would increase both effects, making the device worse. It would also require perfect alignment.

Perpendicular alignment

At any point of the cell, the electric field vector and the director lie in the same plane. Thus, the twist angle will be zero whatever the applied voltages are. The main problem to be pointed out is the pre-tilt angle responsible for the asymmetry of the device. In order to compare the director profiles when the voltage staircase is reversed from V_1, $V_2 ... V_M$ to $V_M ... V_2$ V_1, the pre-tilt has been changed to the same but negative value instead, which is equivalent. Reversing the voltage staircase in order to change the sign of the diffraction order selected ($+1^{st} \rightarrow -1^{st}$), results in different directors profiles for this configuration as illustrate Figs. 6.10a and b. In addition, the directors are 'shifted' due to the different constraints. This is also true in the case of parallel-aligned gratings, where the local maxima of tilt angle are not centered with respect to the electrode. In Fig. 6.10b the smallest tilt values appear where the the highest vertical fields are. Also the shape appears smoother, but quite different from a staircase or a blazed profile. This clearly means that the device is not symmetrical and that the driving parameters must be readjusted when the light beam is steered from a positive to a negative diffraction order.

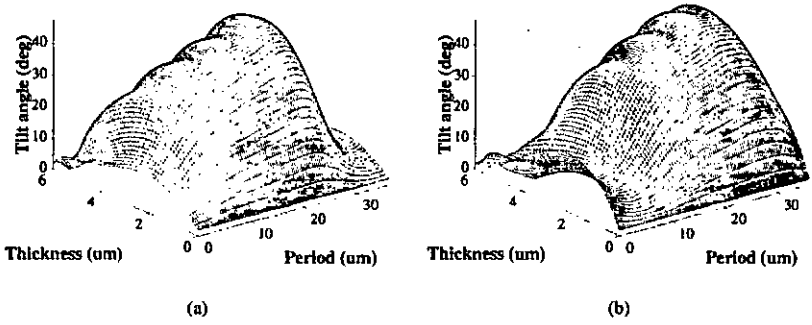

Figure 6.10: *Director profiles for perpendicular-aligned liquid crystals resulting from the same simulation a Fig. 6.8. Changing the sign of the pre-tilt is equivalent to change the sense of the voltage romp. a) and b) show different director profiles for the same but inverted voltage staircase / pre-tilt angle.*

Another aspect of the pre-tilt influence in the director profile comes from the small value of this angle. The problem already appeared in binary gratings. Figure 6.10b shows that the director distribution is somewhat disturbed between the electrodes with highest and lowest voltage. This

problem was already pointed out for small pre-tilt in binary gratings, where a reverse tilt was observed.

Figure 6.3 shows that higher pre-tilt reduces and finally smears out the threshold voltage, while it showed smoother and less asymmetric behavior in binary gratings. This change would improve both the symmetry and eliminate the reverse tilt, but an excessive pre-tilt would also increase the fly-back length Λ_F, which is the distance within the period going from the highest to the lowest value of the phase profile that will result from the calculated director profile.

6.3 Propagation of light

6.3.1 Phase grating function

The Jones matrix calculus can be used for two-dimensional simulations as long as the rays follow a nearly straight path within the limits of the columns defined by the grid used for the simulations. In chapter 4 it has been shown that the gradients resulting from two-dimensional simulation of binary gratings are not strong enough to require rigorous calculation. Even if the voltage required for 2π modulation in blazed gratings is higher than the one used for binary gratings, the lateral gradient will not increase enough to require rigorous calculation of the phase profile.

Perpendicular alignment

The most important property of this kind of device is the fact that the linear input polarization remains linear. The director is only tilt modulated, i.e. it rotates only in the plane parallel to the grating lines. As long as the polarization plane and the alignment direction are the same and the incidence is normal to the device, the linear polarization will be maintained. For the same reason, the transmission amplitude along the period is uniform. The only amplitude modulation comes from the difference of the refractive index between ITO and glass. Thus, the complex amplitude of the linear output polarization becomes Jones matrix that comes out from the parallel-aligned liquid crystal is,

$$v(x) = a\,(x) \cdot \exp\left(i \cdot \varphi_s^s\,(x)\right), \tag{6.3}$$

where s stands for perpendicular (senkrecht in German). The calculated phase profile using the previously calculated director profiles is shown in Fig. 6.11.

For this configuration the problem comes from the voltage driving and the pre-tilt angle. The director profiles in Fig. 6.10 have already revealed that the deformation is different when the

staircase voltage profiles are applied in opposite direction. The resulting phase profiles for 6-level gratings are shown in Fig. 6.11b. Not only the shape, but also the relative position with respect to the electrodes is different. This means that it will not be possible to switch from the -1^{st} diffraction order to the $+1^{st}$ simply reversing the voltage staircase. Each order will require a specific driving pattern.

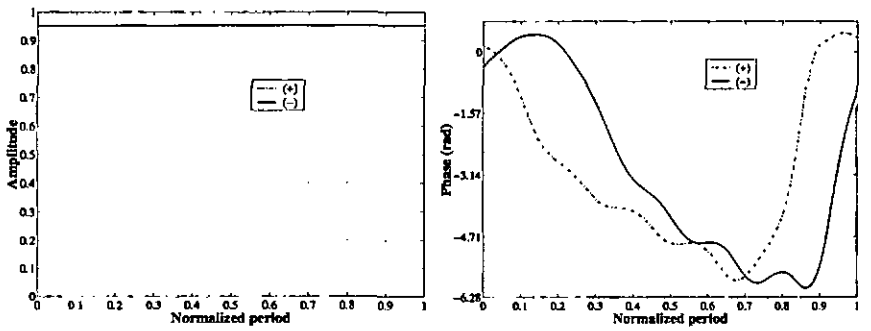

(a) (b)

Figure 6.11: *Amplitude (a) and phase (b) of the linearly polarized output wave (dash-dotted: + pre-tilt, solid: - pre-tilt).*

Parallel alignment

In this case, the device behaves symmetrically, but the linear input polarization is not maintained. In fact, the twist is responsible for a much stronger gradient at the end of the period. The question now is to know if the twist causes a too strong lateral gradient that would require a rigorous calculation of the propagation in the liquid crystal or if we can admit that the Maughin condition is respected and the linear polarization is maintained and follows the twisted liquid crystal, thus allowing Jones matrix calculation.

For linear polarized input, parallel to the alignment of the LC, the Jones vector at the output becomes

$$j_p(x) = \begin{bmatrix} b(x) \cdot \exp\left(i \cdot \varphi_p^s(x)\right) \\ d(x) \cdot \exp\left(i \cdot \varphi_p^p(x)\right) \end{bmatrix} \tag{6.4}$$

where $d(x)$ and $\varphi_p^p(x)$ are the parallel components and $b(x)$ and $\varphi_p^s(x)$ are the perpendicular

components of the output polarization, with respect of the input polarization. The perpendicular component is caused by the twist, i.e. the optical activity of the device. p stands for parallel.

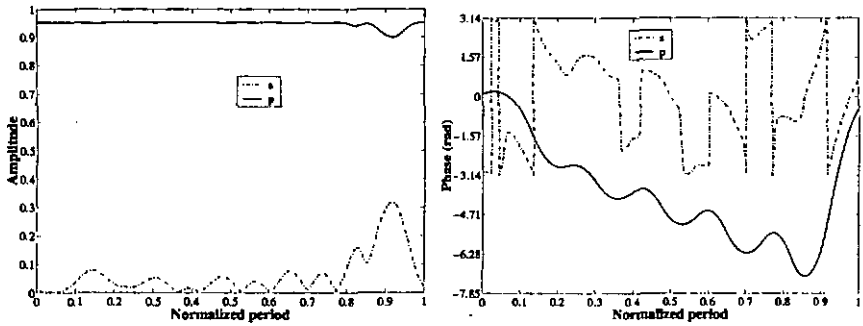

(a) (b)

Figure 6.12: *Amplitude and phase plots for a parallel aligned, 6 μm thick and 2° pre-tilt cell. The zero values that appear in the perpendicular term $b(x)$ are responsible for the discontinuities in the phase component $\varphi_p^s(x)$.*

Figure 6.12 shows amplitude and phase profiles for the parallel and perpendicular polarizations along the period of a 6 level grating. Figure 6.12a shows that almost all the energy goes to the parallel polarization component of the output. The phase profile for this polarization shows a more important influence of the high frequency modulation caused by the discrete electrodes than in the case for the perpendicular aligned gratings.

From Fig. 6.12a we see that the perpendicular polarization component is not zero ($b(x) \neq 0$), except at some points where discontinuities (π phase jumps) occur . Since the input polarization is parallel to the alignment, this means that the device is optically active, i.e. there is twist deformation. Except for the hot spot between the first and last electrode of consecutive periods, the value of $b(x)$ is relatively small compared to $d(x)$. Only where the twist deformation is relatively strong, the $b(x)$ becomes important. The Maughin condition $\left(\theta \leq \frac{\pi}{\lambda} \cdot d \cdot \Delta n\right)$, discussed in chapter 4, is respected in this critical zone. Using the maximal twist angle ($\theta_{max} \simeq 25°$) shown in Fig. 6.9b, we obtain that the twist should take place within a length of $0.32\,\mu m$, almost $1/20$ times the thickness, which is certainly no the case. We can conclude that the condition is respected.

6.3.2 Propagation in free space

Figure 6.13 shows the diffraction patterns for the parallel-aligned grating. Using the Fraunhofer approximation described in chapter 4 and with the FFT functions implemented in Matlab [81], the propagation in free space can be calculated from the phase and amplitude functions shown in Figs. 6.11 and 6.12. Both polarizations are calculated independently for the parallel-aligned cells and the intensities are added at the image plane. Practically, the contribution of the perpendicular component in Eq. (6.4) and Fig. 6.12 is neglectible.

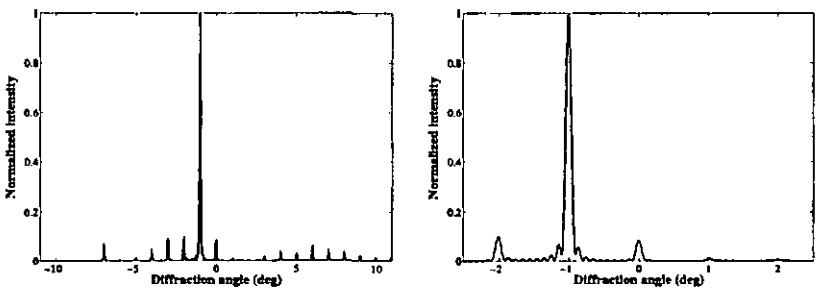

(a) (b)

Figure 6.13: *Diffraction pattern calculated for the profiles in Fig. 6.12 of a) between* $-2.5°$ *and* $2.5°$. *b) is the blown-up part. (6 levels, period* $p = 36\ \mu m$, $\lambda = 633\ nm$, *aperture* $d = 250\ \mu m$.

Figure 6.13a shows that the diffraction pattern has many orders. The -1^{st} order is the one selected by the blaze, while the others are parasitic orders due to residual modulation originating from the discrete electrodes.

Although the simulated phase profile has not been fine-tuned for high diffraction efficiency into the -1^{st} order and extinction of the 0^{th} order, the performance is quite good, as shown in the detail of Fig. 6.13b. Given the long time required to perform two-dimensional calculations of the director profile, fine tuning of the voltages for high efficiency has not been performed. Nevertheless, the diffraction efficiency has been calculated using the phase profiles and correcting the phase retardation to find the ideal phase modulation depth for the different profiles. Figure 6.14 shows the relation between diffraction efficiency and modulation depth using Eq. (5.5) and the phase profiles of Figs. 6.9 and 6.10. The efficiency of the diffraction into the first order can be estimated at 65%.

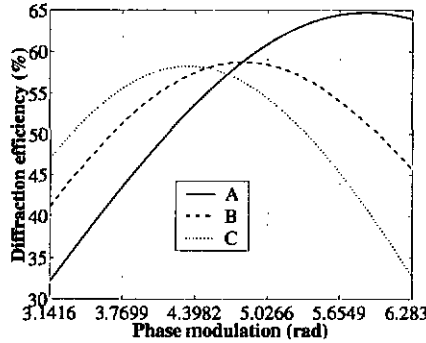

Figure 6.14: *Diffraction efficiency vs phase modulation depth for the phase profiles corresponding to parallel and perpendicular alignment. (A) Parallel alignment. (B) Perpendicular alignment with positive pre-tilt. (C) Perpendicular alignment with negative pre-tilt. Fly-back and high frequency modulation by the electrodes are the main causes for the relatively low value of the maximal efficiency (65%). (6 levels, $p = 36\ \mu m$, $d = 6\ \mu m$, pre-tilt = 2°)*

6.3.3 Efficiency estimation

To fabricate gratings of very small size, photolithographic processes can be used, approaching the blazed grating with a staircase of M steps. The steps must have an optical retardation equal to $2\pi/M$. The theoretical efficiency of an ideal staircase into the first order is [18],

$$\eta_M = \left(\frac{\sin\left(\frac{\pi}{M}\right)}{\frac{\pi}{M}} \right)^2 . \tag{6.5}$$

As seen in the previous sections, a liquid crystal cell with an array of parallel electrodes produces a staircase like phase profile (Fig. 6.4). But through the elastic properties of the liquid crystal, the steep profile will be smoothed out. The 2π steps at the borders of the period should be perfectly steep to obtain high efficiency. In practice, however, this transition has a finite width Λ_F, called fly-back length, which reduces the diffraction efficiency by,

$$\eta_{\Lambda_F} = \left(\frac{\Lambda - \Lambda_F}{\Lambda} \right)^2 \tag{6.6}$$

where Λ is the period length of the grating.

The resulting efficiency of a liquid crystal grating is then given by the product of Eqs. (6.5) and (6.6), with the assumption that $\Lambda_F \ll \Lambda$ [82, 83]. Figure 6.15 illustrates the improvement of

the diffraction efficiency vs. the number of steps, using Eq. (6.5). The efficiency η_F is calculated with the assumption that the fly-back length is equal to the width of one *step* ($\Lambda_F = \Lambda/M$). It is interesting to note, that the length fly-back is responsible for at least 20% of efficiency reduction.

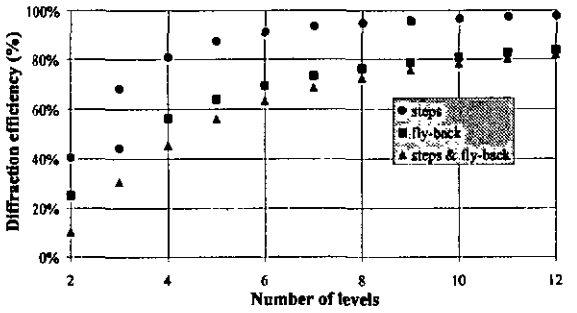

Figure 6.15: *Diffraction efficiencies for staircase profiles, fly-back effect and the product of both. The fly-back length Λ_F is assumed to be equal to the width of one step, that is $\Lambda_F = \frac{\Lambda}{M}$.*

6.3.4 Phase function model to calculate diffraction efficiency

The director profiles previously obtained with the finite element simulation give a good indication of the shape of the phase profiles. Nevertheless, it is not reasonable to spend hours of computer calculation to find the best profile and to fine-tune the applied voltages for any possible number of electrodes. Instead, simple models of the phase profile are used, inspired by the results obtained from the simulations. They take account of the most important parameters, such as the number of electrodes, the fly-back and the depth of the phase modulation.

Main phase profile model

As a result of the small dimensions of the electrodes, the phase profile is considered to be a continuous and smooth function. Therefore, the average phase function is modeled by two sinusoidal functions, as shown in Fig. 6.16a. The two parameters considered are the depth $\Delta\varphi$ of phase modulation and the fly-back length Λ_F. Mathematically, this profile is represented by,

$$\begin{aligned} \varphi(x) &= \tfrac{\Delta\varphi}{2} \sin\left(\tfrac{\pi \cdot x}{\Lambda - \Lambda_F} - \tfrac{\pi}{2}\right) \quad 0 < x \leq \Lambda - \Lambda_F \\ \varphi(x) &= \tfrac{\Delta\varphi}{2} \sin\left(\tfrac{\pi \cdot x}{\Lambda_F} + \tfrac{\pi}{2}\right) \quad \Lambda - \Lambda_F < x \leq \Lambda \end{aligned} \tag{6.7}$$

where Λ is the period length. Using the Eq. (5.12), the amplitude of the N^{th} order diffraction in the far-field (Fraunhofer), the efficiency $\eta_N = |A_N|^2$ can be calculated numerically. The results for the blazed diffraction order (N=1) are presented in Fig. 6.16b as a function of the modulation depth $\Delta\varphi$ and for different number M of electrodes. The fly-back length Λ_F is assumed to be equal to one electrode width ($\Lambda_F = \Lambda/M$). Although a fly-back of $\Lambda_F = 0$ is practically impossible with nematic liquid crystals, the corresponding efficiency is shown as the ideal case for comparison.

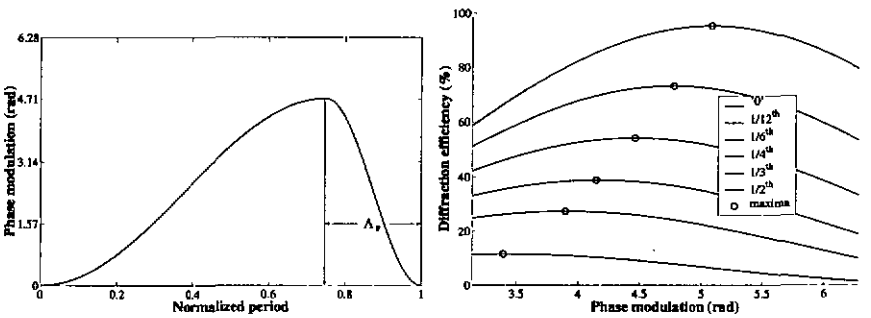

Figure 6.16: *a) Model for the average phase profile. b) Diffraction efficiency as a function of the phase modulation depth $\Delta\varphi$ for different number of electrodes.*

High frequency modulation caused by the electrodes

To include the effect of the valleys in the phase profiles (Fig. 6.12b), caused by the discrete electrodes, an additional modulation is superposed to the average phase profile introduced above. The first term in Eq. (6.7) is multiplied by,

$$\varphi_{HF}(x) = 1 + \delta\varphi \cdot \cos\left(\frac{2 \cdot \pi \cdot \left(M - \frac{1}{2}\right)}{\Lambda - \Lambda_F}\right) \tag{6.8}$$

where $\delta\varphi$ the modulation depth of the additional modulation and M is the number of electrodes within one period.

Figure 6.17a shows the phase profile corresponding to this model, which matches better

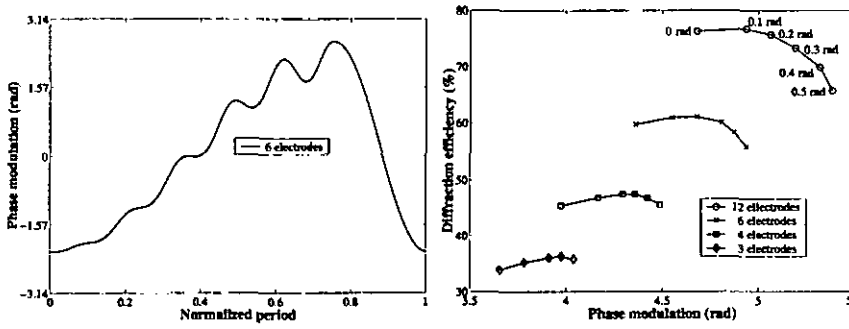

Figure 6.17: *Effect of the high frequency modulation. a) Example of the phase function. b) Calculated diffraction efficiency for M=12, 6, 4 and 3 electrodes per period calculations as a function of the phase modulation amplitude.*

the calculated phase profiles of parallel aligned gratings shown in Fig. 6.12b. In Fig. 6.17b, the maximal diffraction efficiency is plotted for M=3, 4, 6 and 12 electrodes and for different modulation amplitudes $\delta\varphi$ between 0 to 0.5 radians. The fly-back, assumed to be $\Lambda_F = 1.5 \cdot \Lambda/M$. This assumptions matches better with the simulated phase profiles (Fig. 6.16a) than $\Lambda_F = \Lambda/M$, although it depends also on the number of electrodes and the applied voltage. It is interesting to note that the efficiency is improved with respect to the smooth profile (Fig. 6.16b) for small numbers of electrodes. The efficiency is always lower that for the first model presented in Fig. 6.16a. It comes clearly out that a low number of electrodes is not interesting to reproduce a blazed grating, since the efficiency is very low.

Amplitude grating

In addition to the high frequency phase modulation, the electrodes have a second effect on the grating efficiency. Because the glass and the ITO do not have the same refractive index, an amplitude grating is present in the device. ITO has a higher refractive index ($n \simeq 1.7$) as the substrate ($n \simeq 1.5$). The ITO layers are about 25 nm thick and its contribution to phase modulation can be neglected. Instead, the reflection is quite important. The efficiency for the investigated devices drops by 10 to 15% because of this amplitude grating. The grating has the same spatial frequency as the electrodes. This means that its first diffraction order corresponds to the M^{th} diffraction

order of the phase grating. The amplitude modulation is considered as a binary grating, where l is the pitch, i.e. the distance between two consecutive electrodes. Equation (6.9) considers two transmission states corresponding to 1 (100% transmission) and a, the low transmission value.

$$A(x) = \begin{cases} 1\ for & 0 \leq x \leq l/2 \\ a\ for & l/2 < x \leq l \end{cases} \tag{6.9}$$

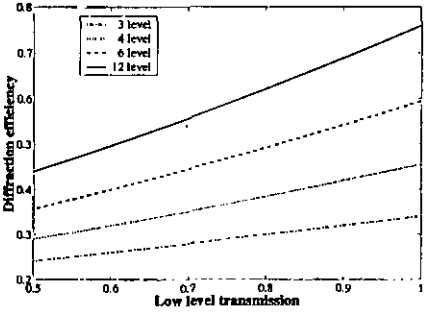

(a)

Figure 6.18: *Efficiency vs. the low transmission value (a) for 3, 4, 6 and 12 electrode per period grotings. The amplitude grating is applied to the optimized smooth profiles of Fig. 6.16b.*

Figure 6.3.4 shows the influence of the amplitude grating when combined with the smooth model for the phase profile. Beginning with the optimized parameters for the phase profiles of Fig. , the amplitude grating is applied resulting in a efficiency drop vs the low value transmission of the amplitude binary grating. Compared to the phase profile that diffracts into the $\pm 1^{st}$ order, the amplitude grating diffracts to the M^{th} order, being M the number of electrodes of a period.

6.4 Cell fabrication, operation and results

6.4.1 Cell fabrication

Array structuration

The electrode pattern for the cells is designed after the model shown in Fig. 6.19. The cells have been fabricated with a total number of 200 electrodes. The width of the contact-electrodes

is 250 μm, half the pitch. The whole cell is 5 cm x 5cm x 1.1 mm in size. Standard glass substrates (0.55 mm) with pre-deposed ITO (25 nm, 50 Ω/sq) is used. Because of the small feature size of 3 μm, the structure was dry-etched in a plasma reactor with Ar ions. Standard alignment polymer (PI-2545 for 2°, SN-70XX for 6°) were spin coated and velour rubbed either parallel or perpendicular to the electrodes. Spheric spacers of 6 μm are used. The counter-electrode substrate was assembled together with the structured substrate and the cell was finally vacuum-filled with liquid crystal (BL006).

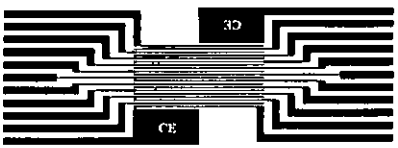

Figure 6.19: *Madel of the electrode pattern.*

Cell mounting and driving

The cell is mounted on a board for connection. The board has two arrays of electrodes which are grouped to form a 24 electrode period. The connection is made through zebra connectors of 360μm pitch. The driving signal is supported by a 25 pin parallel port. Through a PC (486) board (Amplicon PC224), 12 channels can be driven independently with DC and AC square signals of 1kHz frequency. The 24 channels of the connection port are therefore wired to get 12 electrodes per period. Driving voltage range lies within 5 Vrms.

6.4.2 Diffraction measurement

Figure 6.20 shows the measurement setup. The collimated, spatially filtered and linearly polarized ($Contrast - Ratio > 10^5$) beam impinges the cell perpendicularly and with the polarization parallel to the alignment direction of the liquid crystal. A linear CCD detector array with 512 pixels is used to record the intensity of the Fraunhofer diffraction pattern. The same PC that drives the channels makes also the acquisition of the array measurement and the detector of the reference beam I_{Ref}. The optimization of the voltage profile is obtained by optimization of two values: Improving the contrast between the N^{th} diffraction order and the 0^{th} order, and the absolute efficiency into the selected diffraction order N.

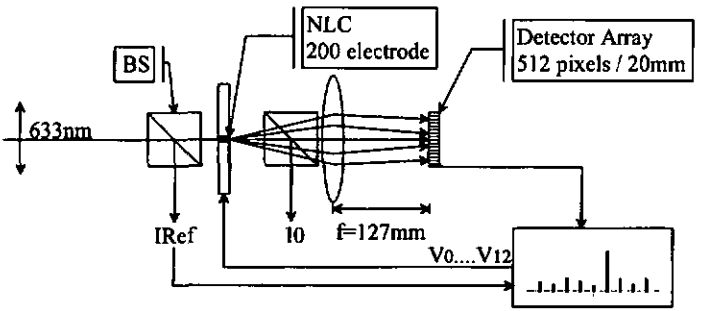

Figure 6.20: *Measurement setup with loop for the optimization.*

Perpendicular aligned cells

This kind of cell shows a behavior which corresponds to the theoretical previsions. In particular, the asymmetry in the diffraction pattern is observed when the voltage ramp is reversed, i.e. when the opposite diffraction order is addressed. Figure 6.21a shows also that the large dynamic range of the cell, more than two wavelengths of modulation, which allows to select up to the 3^{rd} diffraction order by changing the staircase voltage profile. This works particularly well for large numbers of electrodes, in this case M = 12. Figure 6.21b shows that reversing the voltage ramp result in a very different diffraction pattern. This is worst for short number of electrodes than for large number of electrodes.

Another aspect of the driving of perpendicular-aligned cells to point out is that they appear to work better with a bias voltage, but the same steepness of the voltage ramp. A probable reason is that a bias voltage homogeneously increases the tilt angle, thus reducing the risk of reverse tilt or any other director perturbation as those observed in Fig. 6.10.

Parallel-aligned cells

Figure 6.22a shows the different 1^{st} order diffraction efficiencies that can be selected using parallel aligned gratings of different periodicity. Peak values of the efficiencies are lower that those of perpendicular-aligned gratings, mainly due to the stronger effect of the in-plane field on the phase profile. On the other hand, a symmetric diffraction pattern is obtained with reversed voltage ramp, contrary to the previously discussed perpendicularly aligned gratings. Figure 6.22b shows the diffraction pattern of a grating with four electrodes per period and the resulting pattern for both voltage ramps.

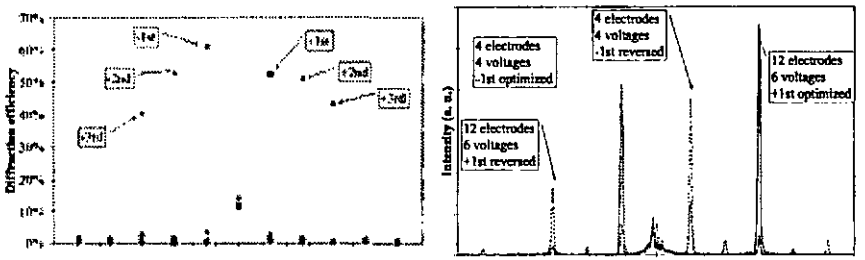

(a) (b)

Figure 6.21: *Measurements of a perpendicular oligned cells. a) The lorge dynomic range of the cell allows to switch up to the* 3^{rd} *diffraction order with 12 electrodes period. b) Perpendicular olignment results in asymmetric behavior. Higher number of electrodes and levels reduce this difference. (LC:BL006, thickness* = 6 μm, *feature size* = 3 μm, *pre-tilt* = 2°).

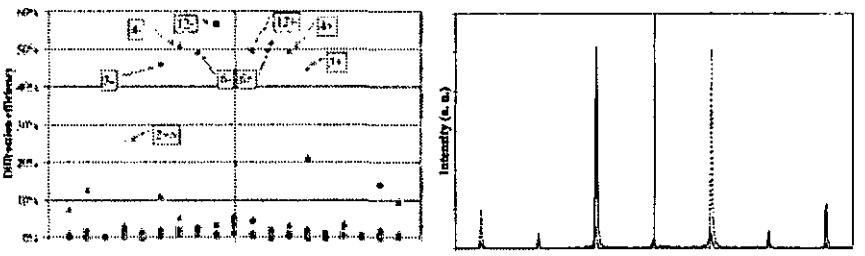

(a) (b)

Figure 6.22: *a) Diffraction efficiencies for different number of electrodes per period M. b) Symmetric diffraction patterns for a parollel aligned grating with optimized and reversed voltage romp. (LC: BL006, thickness* = 6 μm, *feature size* = 3 μm, *pre-tilt* = 6°).

Response time of the gratings

The main reason for the limit of response time of the device is the slow switching of the gratings with low voltages. The highest voltages applied to the electrodes are about 2.5 *to* 3 V and decrease monotonically when the 1^{st} diffraction order is addressed. In addition, the grating depends strongly on viscous and elastic smearing for the director profile between the electrodes, even when the voltages are applied. Altogether, the result is a relatively long switching time.

The first step is to determine the ideal voltage profiles. The optimization algorithm begins with a ramp and all the electrodes have a voltage different from zero. Figure 6.23a shows some optimized voltage ramps for different periods. The lowest voltage is below 1 V, i.e. the threshold voltage where it has no more effect on the director profile. In one of the examples, it has been set to zero, which had nearly no effect on the far-field pattern. The ramp is approximately linear with some corrections to compensate driving inaccuracies.

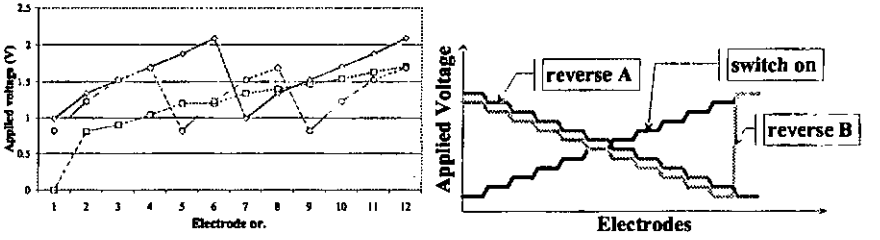

(a) (b)

Figure 6.23: *(a) Optimized voltages ramps for different periods. (b) Different schemes of switching.*

After having determined the voltage ramps, different switching schemes, as shown in Fig. 6.23b, can be analyzed. First, switching on and off all electrodes is considered. Also, reversing the voltage ramp has been studied. This can be done in two different ways, either by rotating around the center of the ramp and thus replacing the higher voltages by the lower voltages and so on (A), or by rotating at the highest voltage electrode (B).

Figure 6.24a shows some measurements for switching on and off the voltage ramps. Different combinations of voltage ramps have been considered. Although there are some differences, the values are similar. The switching time is thus mainly defined by the importance of the highest applied voltage and not the shape of the grating. On the other hand, Fig. 6.24b shows a scheme of the response signals when the ramps are reversed. The measured signal is the selected diffraction order. The local minima and maxima are caused by the rearrangement of the liquid crystal molecules in the cell. Although the cell is symmetric is of parallel alignment type, the measurement curves are not of the same shape. The main reason is that the curves do not show the same measurement. The continuous line shows how fast the optimized diffraction pattern is lost reversing the voltages. The second, dashed line shows how long it takes to the signal to recover after reset of the original voltage ramp. Most of the time is 'wasted' by the flow and it takes also

longer to obtain a specific shape than to delete it. Reversal of type A is some milliseconds slower than type B.

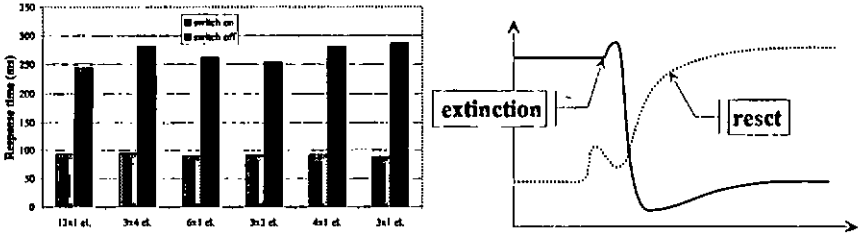

(a) (b)

Figure 6.24: *a) Measurements of switch-on and switch-off times for different period lengths. b) Typical response for ramp reversal of the* 0^{th} *and* 1^{st} *order. (LC: BL006, thickness* = 6 μm, *feature size* = 4 μm, *pre-tilt* = 2°, *parallel-aligned).*

6.4.3 Other aspects influencing the diffraction efficiency

There are two main effects influencing negatively the diffraction efficiency which are not caused by the liquid crystal itself. The first one is the presence of spacers in the active zone, and the second one is due to the structured electrodes.

Spacers

As mentioned in chapter 2 on technology, the presence of the spacers in the cell is responsible for a decrease in the performances of a liquid crystal device in general. The transmission through crossed polarizers is not zero, because the spherical spacers act as scattering centers. As a consequence, the diffraction efficiency cannot be further improved by optimizing the phase profile.

Etching

Dry etching is an aggressive method, which results in rough edges of the electrode. Again, this is a scattering source that is recognizable from the spreading of the zero order compared to the width of the other diffraction orders. Figure 6.25 shows the measured diffraction pattern. Clearly, the base of the zero order is by far larger than these for other diffraction orders.

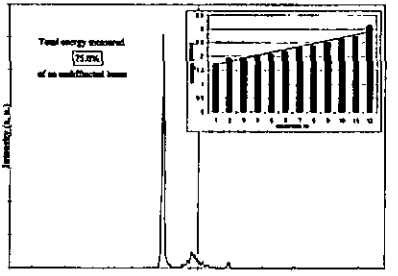

Figure 6.25: *Measured diffraction pattern for the best voltage profile (parallel aligned cell).*

ITO pattern

As discussed in section 6.3.4, the amplitude grating caused by the difference of the refractive index between the ITO and the glass substrate is responsible for an efficiency loss of at least 12%. This value has been measured by comparing the transmission of the cell in an unstructured zone with the transmission through the grating.

Electric impedance

Two aspects render the driving of the cell more difficult. First, as it can be seen in Fig. 6.19, the outer electrodes have a longer path than the inner ones. For a given resistivity of the ITO layer, the voltage drop is more important for the external electrodes. For the driving, every twelfth electrodes are connected to the same voltage. However, because of the different lengths of the connecting paths, the phase profiles are not the same at the center of the grating and at the ends. The resulting grating is not exactly periodic. Second, the cover-substrate is not etched and represents a large surface capacity.

6.5 Extension to three-dimensional structures

Given the flexibility to produce specific two dimensional phase profiles, it is interesting to study the possibilities of extending this method to three-dimensional devices, especially lenses. Two main configurations are considered, one is based on the properties of binary gratings and the other on those of tunable gratings. The micro-lens array base on fringing field effects was already discussed in chapter 3.

Binary profile lenses

This type of lenses is based on a binary phase modulation of π retardation. The lens consists of a set of rings with variable width and separation, as illustrated in Fig. 6.26. The width and separation of these rings decreases for an increasing radius. Thus, the maximum numerical aperture (NA) of the lens depends on the resolution limit fixed either by the technology ($\sim 3\mu m$) or by the liquid crystal minimal period. This later is related with the discussed critical period length.

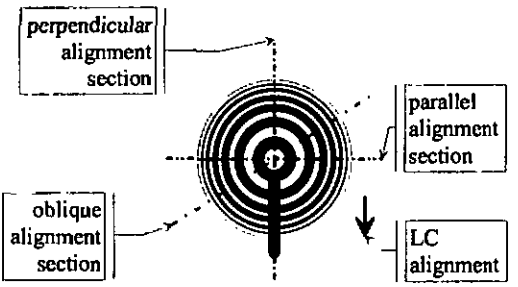

Figure 6.26: *Fresnel lens with rings of variable width. The one directional alignment at the surface results in sections with parallel, perpendicular and oblique alignment of the LC, with respect to the electrodes.*

As discussed in chapter 5, the length of the period where a π phase shift can be realized is linearly dependent of the thickness. With high birefringent liquid crystals like BL006, the minimal thickness required for π retardation is $d \geq \lambda/(2 \cdot \Delta n) \approx 1.15\,\mu m$. According to Fig. 5.10, the electrode width must be $> 5\mu m$. With standard technology, thicknesses below $5\mu m$ are very difficult to realize because of the high risk of electrical shortcut. This limits the ring smallest width to $15\,\mu m$. Figure 6.27 shows that both in simulated and measured lenses the efficiency is at its theoretical maximum (40.5 %) until the zones or rings of width below the critical length are reached.

Driving this type of lens is simple, because all rings are electrically connected and the same voltage is applied. This reduces the functionality to two working states, that is, either focusing at the designed focus length, or not focusing at all. If the device could be realized at its smallest thickness, it would be a quite fast device, with an estimated switching off time of $\sim 5\,ms$!

Nevertheless, it must not be forgotten that the one dimensional alignment at the surfaces results in section with parallel, perpendicular and oblique alignment of the LC with respect to the electrodes, as indicated in Fig. 6.26. Therefore, all the problems and limitations mentioned

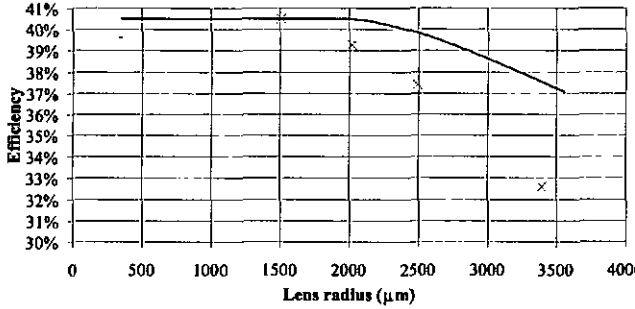

Figure 6.27: *Efficiency vs. diameter for fixed focal length = 100 mm. The continuous line corresponds to a simulated binary lens of 6 μm thickness, where the efficiency of each zone is calculated after Fig. reffig:p-diff-eff. The crosses correspond to a measured cell of 5 μm thickness.*

in chapter 5 are present. Specially, high pre-tilt is necessary to improve the rotational symmetry.

Tunable lenses

Based on the tunable blazed gratings, these lenses are only technologically limited by the width of the electrodes. The efficiency of the phase profile will depend on the suppression of the high frequency caused by the discrete electrodes which can be realized with a more important thickness although strongly worsening the switching speed. Again, the problems concerning the planar alignment are found for this type of device.

Given that each ring has its own voltage, the overall shape of the phase profile can be adjusted and therefore the focal length becomes adjustable too. Two operating modes are possible, either as refractive lens or as diffractive lens. For the first case, all the electrodes are used to reproduce the spherical profile in a single zone. This is specially interesting if th modulation depth of the cell is of several wavelengths. For the diffractive type illustrated in Fig. 6.26a, the thickness is again a important parameter, since it will determine the width of the 2π phase steps and therefore the efficiency.

Figure 6.29 shows how the efficiency drops when the numerical aperture increases. The outer zones have a decreasing number of electrodes and therefore the efficiency drop. The efficiency

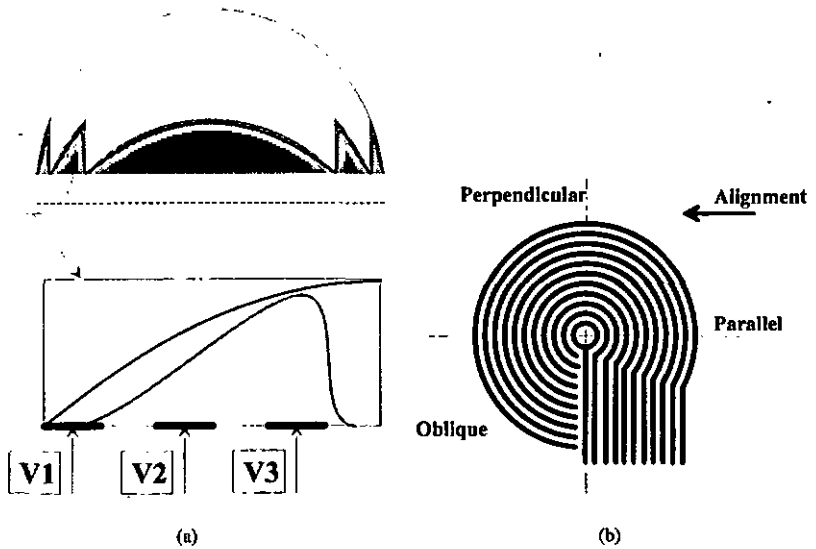

Figure 6.28: *a) The spherical profile is approximated with the liquid crystal. At least 3 electrodes are required for each zone. b) Connecting each ring individually results in a loss of active area and efficiency drop.*

of each zones is calculated using

$$\eta_{zone} = \left(\frac{\sin\left(\frac{\pi}{M}\right)}{\frac{\pi}{M}}\right)^2 \cdot \left(\frac{\Lambda - \Lambda_F}{\Lambda}\right)^2. \tag{6.10}$$

The highest efficiency is obtained with the smallest feature size. But the numerical aperture (NA) is extremely small and, it is not a diffractive lens at all, since the limit of 100 electrodes is reached with a single zone.

A specific problem of this device comes from the different voltages used. A sector of the disc must be used to connect the inner rings with the driving voltages. More rings result in a more important surface wasted for connecting and therefore a decrease of the efficiency of the lens. Figure 6.26c shows this connecting zone.

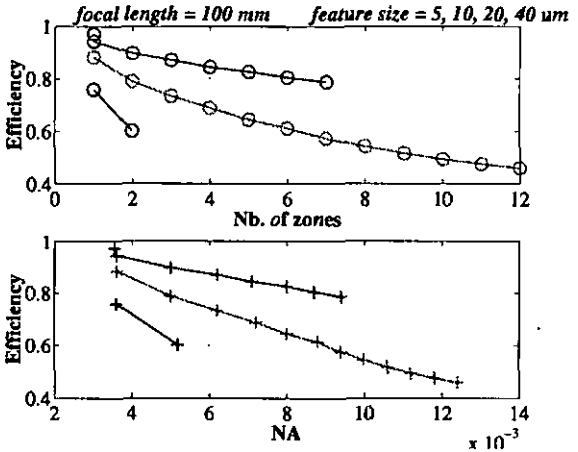

Figure 6.29: *Efficiency vs. number of zones or numerical aperture for different feature sizes. The calculation is limited to a maximum of 100 electrodes and at least 3 electrodes per zone.*

Conclusion

For all types of lenses, including micro-lens arrays, the main problem comes from the alignment. Planar alignment result in a phase profile which is not spheric. The homeotropic (vertical) alignment has a rotational- or radial-symmetric director profile, but the phase profile is not, due to the twist modulation that results from the radial alignment illustrated in Fig. 6.30.

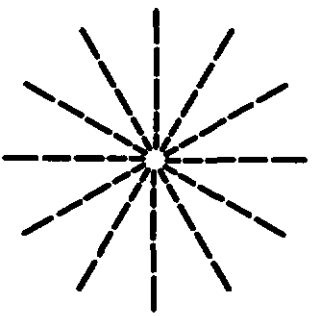

Figure 6.30: *Radial director profile and polarization direction. It is clear that the device will not result in a spheric phase modulator.*

A cascade of two identical lenses might be a solution although requiring a half-wave plate between both lenses.

6.6 Summary

1. *A staircase phase profile can be reproduced in liquid crystals with an high frequency array of electrodes.*

2. *The smooth deformation improves efficiency between the electrodes except between the extreme voltage electrodes.* The phase transition is smooth creating a fly-back and resulting in efficiency drop. This fly-back length is proportional to the thickness and limits the resolution of the grating.

3. *Parallel alignment to the electrodes gives high efficient gratings whose ramp can be reversed without efficiency loss.*

4. *Perpendicular alignment is also high-efficient but not reversible.*

5. *Several wavelengths of modulation depth results in a very flexible device which can select up to the* 3^{rd} *diffraction order.*

6. *The high frequency of the electrodes can decrease the efficiency for thin layers and through the intensity modulation of the electrodes.*

7. *Diffractive lenses, with binary or spherical profile, can be produced with planar-aligned nematic liquid crystal.* But the relative alignment of the liquid crystal with respect to the edge of the electrode rings will not result in a perfect rotational-symmetric profile.

8. *The efficiency of the lenses is directly influenced by the resolution that can be reached with the liquid crystal profiles.* (Critical period length for binary profiles and fly-back length for tunable profiles)

Conclusion

With this work, it has been shown that an ad initio analysis of nematic liquid crystal devices, and more concretely diffractive devices, is possible. The different steps of the modeling have been considered, from the director profile to the far-field propagation of light, and give accurate results. The following points have been discussed and further improvements are proposed.

LC simulation Software One dimensional simulations are current nowadays for the optimization of the optics of liquid crystal displays. The software used (LCDMaster) allows to analyze the behavior of the liquid crystal when switched, both at equilibrium and vs time. But it also allows to analyze the optical characteristics of the device as a whole including all the compensation sheets, polarizers, substrates, etc. This tool has been also be used in the infrared spectra, at 1550 nm wavelength. The properties database have been adapted to the new spectra (dispersion) and the related parameters have been scaled conveniently.

Two and three-dimensional simulations are not so often used and the program does not give as much information as for the one-dimensional simulations. But they give the more important result, that is, the two or three-dimensional distribution of the directors resulting from a complex electric field distribution. The calculations are mainly limited by the calculation grid, which is regularly spaced and of limited density of points. The grid is not locally adaptive to the strong gradients of the electrical field that might appear at the edges of the electrodes. These simulations are extremely resources- and time-consuming. Therefore, optimization of devices is not imaginable nowadays. Nevertheless, quite complex configurations have been analyzed, such as multi-electrode gratings and lenses. From the simulations of diffractive devices using planar-nematic LC's, the most important result to point out is the effect of the relative orientation of the directors with respect to the edges of the discrete electrodes.

Light propagation The device configuration used, that is, planar-aligned nematic liquid crystal in thin layers ($\sim 5\mu m$), permits to use the Jones matrix method to calculate the propagation

of polarized light through the device using the refractive index distribution obtained from the LCDMaster two and three-dimensional simulations. The lateral gradients appear to be smooth enough to accept the propagation as straight. The orthogonal grid obtained from LCDMaster can be directly used and the calculation performed for each column independently. This is only valid for normal incidence. An amplitude and retardation profile is obtained after the calculation. This profile, generally part of a phase grating, is propagated in free space. This is done assuming Fraunhofer diffraction and calculated using Fourier transform. The results obtained are in very good agreement with the measurements of the gratings realized.

Binary diffractive gratings The main result obtained from this type of grating is that the resolution of such gratings is limited. The period length is limited by the lateral extension of the deformation, which is an obvious consequence of the visco-elastic properties of the liquid crystal together with the appearance of fringing fields at the edges of the structured electrodes. This limit is also directly related to the thickness of the cell. As expected, the relative orientation of the directors respectively to the electrode edges result in an asymmetry in the far-field image.

Multilevel gratings It has been shown that high efficient diffractive devices with electrodes of $3\mu m$ width can be made. Still, a large margin for improvement is present. Two main aspects limit their performance. First, the design of the electrodes. The voltage drop along the electrode, due to the resistive characteristics of ITO, is not the same for all the electrodes, since they are of different lengths. Second, the same ITO electrodes act as a binary diffractive grating which results in an important efficiency drop of the device.

Simple driving methods have been used for multilevel diffractive gratings. There is also a large margin for improvement, specially what concerns the switching speeds and the corresponding driving signals. For applications such as routing of optical fiber beams, high efficient algorithms could be implemented in the driving and control loop to improve the diffraction efficiency and selectivity of the diffractive gratings. The slow response of the devices to the driving signals is a result of the low voltages used, close to the threshold, and the characteristics of nematics. Specific driving signals would be required for specific applications.

The measurement and control loop used has allowed to characterize the properties of the diffractive gratings that have been realized and to verify the previsions made before, which have been proven correct.

Adaptive lenses After the observations obtained from binary and multilevel gratings, the application to adaptive lenses is obvious. Three types of lenses have been considered; micro-lenses,

binary Fresnel lenses and multilevel Fresnel lenses. While micro-lenses and binary lenses have practically a single focal point, multilevel lenses could be variable focal devices. But a more flexible device would be a less efficient one by the presence of connecting electrodes. Also, all three types of lenses present the asymmetry discussed with the gratings through its relative alignment to the electrodes. The rotational symmetry of the electrodes is not matched by the planar-aligned LC, presenting a natural asymmetry for the device.

Technology Besides, a new technology for cholesteric texture devices has been developed. The ribs technology allows to isolate different liquid crystals within a single layer acting as a barrier. they serve also to control the thickness of the layer in two ways; by fixing the thickness and as adhesive. Additionally, they improve the resistance of the device against external mechanical stresses.

Acknowledgements

I would like to thank

- Prof. Réné Dandliker, director of the thesis.
- Prof. Pierre Ambs for the interest in the thesis and the availability to become member of the jury.
- Prof. Hans-Peter Herzig as member of the jury and colleague at IMT.
- Dr. Toralf Sharf, for the productive discussions during the last two years at the IMT and the German lessons.
- Dr. Neil Collings, for accepting me for the project and the guidance during he first two years at the IMT.
- Dr Joachim Grupp as memeber of the jury, and for the guidance in the technology of liquid crystals as well as giving me access to the tools at ASULAB SA.
- M. Rolf Klappert, for the discussions in liquid crystals technology and properties.
- Dr. Manuel Teijido for computer support and tennis lessons.
- Dr. Alain Courteville for his photographic knowledge and the help blaming Microsoft.
- M. Marcel Groccia for his help on electronics and measurements.
- Frederic Gonté for closing the window.
- Olivier Ripoll for his exhausting news on computers and software.
- Irene Phillipoussis and Stephanie Clement for her "très spéciale" feminine touch, the smoke and sitting on the stairway to the cafet'.

- All the other members of the IMT Applied Optics group for the fun we had.
- Special thanks to the founders and members of the ClubMax (Dr. Rodellar, Dr. Lopez de Meneses, Dr. Thonet, Dr. Constantini, Dr. Noro, Dr. Ziliani, Andrea, Georgette, Dr. Isa, Dr Nadenau, and so on....) at the EPFL, for the never-professional activities.
- More special thanks to the ever faster growing Spanish colony at the EPFL (David, Edu, Juarez, Eulalia, Elvira, Arrate, Pedro, Patricia, Marc, Laura,) for filling my mailbox with highest priority contents such as: "A comeeeeeeeeeeeer! 12:30 DE" or "Helado a las 16:45 en la Coupole"
- ...and to the family; Pa, & Ma, & BK & Co., & Drea & Co, and all the other relatives.

Bibliography

[1] J. W. Goodby, "Phase structures of calamitic liquid crystals," in *Low molecular wight liquid crystals I* (D. Demus, J. Goodby, G. W. Gray, H. W. Spiess, and V. Vill, eds.), vol. 2A of *Handbook of liquid crystals*, pp. 488–505, Weinheim: Wiley-VCH, 1998.

[2] R. Stannarius, "Elastic properties of nematic liquid crystals," in *Low molecular weight liquid crystals I* (D. Demus, J. Goodby, G. W. Gray, H. W. Spiess, and V. Vill, eds.), vol. 2A of *Handbook of liquid crystals*, pp. 60–68, Weinheim: Wiley-VCH, 1998.

[3] S. T. Wu, "Infrared properties of nematic liquid crystals: an overview," *Opt. Eng.*, vol. 26, no. 2, pp. 120–128, 1987.

[4] G. Pelzl, "Optical properties of nematic liquid crystals," in *Low molecular weight liquid crystals I* (D. Demus, J. Goodby, G. W. Gray, H. W. Spiess, and V. Vill, eds.), vol. 2A of *Handbook of liquid crystals*, pp. 128–141, Weinheim: Wiley-VCH, 1998.

[5] P. G. Gennes, "Static distortions in a nematic single crystal," in *The Physics of Liquid Crystals* (W. Marshall and D. H. Wilkinson, eds.), The International Series of Monographs on Physics, pp. 59–95, Oxford: Clarendon Press, 2nd ed., 1975.

[6] J. L. West, X. Wang, Y. Ji, and J. R. Kelly, "Polarized uv-exposed polymide films for liquid-crystal alignment," vol. 26, pp. 703–706, SID Symposium Digest, 1995.

[7] T. Hashimoto, T. Sugimaya, and K. Katoh, "Tn-lcd with quartered subpixels using polarized uv-light-irradiated polymer orientation films," vol. 26, pp. 887–890, SID Symposium Digest, 1995.

[8] Rolic, "Animated demonstrations of lpp technology of rolic ltd.," 1999.

[9] J. Chen, P. J. Bos, D. R. Bryant, D. L. Johnson, S. H. Jamal, and J. R. Kelly, "Four-domain tn-lcd fabricated by reverse rubbing or double evaporation," vol. 26, pp. 865–868, SID Symposium Digest, 1995.

[10] C. M. Titus and P. J. Bos, "Efficient, polarization-independent, reflective liquid crystal phase grating," *Appl. Phys. Lett.*, vol. 71, no. 16, pp. 2239–2241, 1997.

[11] C. J. Newsome, M. O'Neill, and R. J. Farley, "Laser etched gratings on polymer layers for alignment of liquid crystals," *Appl. Phys. Lett.*, vol. 72, no. 17, pp. 2078–2080, 1998.

[12] K. Kimura, N. Naito, S. Shirai, and N. Yamauchi, "Design and evaluation of low-cross-talk twisted nematic liquid crystal cells for optical switches," *Opt. Lett.*, vol. 17, no. 23, pp. 1647–1649, 1992.

[13] B. Zueger, "Liquid crystal optical switch at 1.53 um," diploma, Institut de Microtechnique / Université de Neuchâtel, 1997.

[14] K. Hashimoto, M. Okada, K. Nishiguchi, E. Yamakawa, and T. Taniguchi, "Reflective color display using cholesteric liquid crystals," vol. 29, pp. 897–900, SID Symposium Digest, 1998.

[15] T. Minato and K. Suzuki, "Orientation of temperature gradient-cooled ferroelectric and antiferroelectric liquid crystals in restricted rectilinear space," *Liq. Crys.*, vol. 23, no. 1, pp. 43–50, 1997.

[16] T. Minato and K. Suzuki, "Temperature gradient-cooled smectic-a phase orientation and its effects on cl orientation in ferroelectric liquid crystals," *Liq. Crys.*, vol. 24, no. 5, pp. 727–733, 1997.

[17] T. J. Gardner and R. P. Wenz, "Stn alignment on rib-spaced plastic lcd substrate," vol. 26, pp. 695–698, SID Symposium Digest, 1995.

[18] H. P. Herzig, "Design of refractive and diffractive micro-optics," in *Micro-Optics: Elements, systems and applications* (H. P. Herzig, ed.), London: Taylor and Francis, 1997.

[19] W. Turalski, A. C. Mitus, and A. Miniewicz, "Monte carlo simulation of electric fields induced spatial light gratings in nematic liquid crystals," *P. Appl. Opt.*, vol. 6, pp. 589–598, 1997.

[20] H. Mori, E. C. Gartland, J. R. Kelly, and P. K. Bos, "Multidimensional director modelling using the q tensor representation in a liquid crystal cell and its application to the p cell with patterned electrodes," *Jpn. J. Appl. Phys.*, vol. 38, pp. 135–146, 1999.

[21] J. E. Anderson, P. Watson, and P. J. Bos, "Shortcomings of the q tensor method for modelling liquid crystal devices," vol. 30, pp. 198–201, SID Symposium Digest, 1999.

[22] Shintech, "Lcdmaster," 1996.

[23] S. Liu, C. Li, and Y. Chen, "Polarization device employing the combination effect of double refraction and diffraction," *Appl. Phys. Lett.*, vol. 67, no. 14, pp. 1972–1974, 1995.

[24] M. Jepsen and H. J. Gerritsen, "Liquid crystal filled gratings with high diffraction efficiency," *Opt. Lett.*, vol. 21, no. 14, pp. 1081–1083, 1996.

[25] G. P. Nordin, M. W. Jones, J. H. Kulick, R. G. Lindquist, and S. T. Kowel, "Three-dimensional display utilizing a diffractive optical element and an active matrix liquid crystal display," *Opt. Eng.*, vol. 35, no. 12, pp. 3404–3412, 1996.

[26] W. T. He, T. Nose, and S. Sato, "A double-layer polymer / liquid crystal grating with polarization direction-independent diffraction properties," *Jpn. J. Appl. Phys.*, vol. 37, no. part2, No. 7A, pp. 795–797, 1998.

[27] S. H. Lee, S. L. Lee, and H. Y. Kim, "Electro-optic characteristics and switching principle of a nematic liquid crystal cell controled by fringe-field switching," *Appl. Phys. Lett.*, vol. 73, no. 20, pp. 2881–2883, 1998.

[28] N. A. Riza and N. Madamopoulos, "Photonic delay line using electrically switched gratings in polymer dispersed liquid crystal," *Opt. Eng.*, vol. 37, no. 11, pp. 3061–3065, 1998.

[29] H. Sakata and M. Nishimura, "Tunable zero-order diffraction using liquid crystals filled in groove-gratings," in *Microoptics Conference MOC'99* (J. S. A. Phys., ed.), (Makuhari, Japan), pp. 216–219, 1999.

[30] L. M. Blinov, "Behavior of liquid crystals in electric and magnetic fields," in *Fundamentals* (D. Demus, J. Goodby, G. W. Gray, H. W. Spiess, and V. Vill, eds.), vol. 1 of *Handbook of liquid crystals*, pp. 477–534, Weinheim: Wiley-VCH, 1998.

[31] K. Okano, K. Kitahara, and E. Ushizawa, "Surface disclinations on modified substrate," *Jpn. J. Appl. Phys.*, vol. 33, pp. 6262–6267, 1994.

[32] Shintech, "Lcdmaster user guide," 1996.

[33] P. J. Collings and M. Hird, *Introduction to liquid crystals.* The liquid crystals book series, London: Taylor and Francis, 1997.

[34] J. R. Kelly, "Twist," 1995.

[35] Autronic-Melchers, "1dimos - 2dimos."

[36] M. Kitamura, "Computer simulation of director profile in two dimensional electric field," in *International Display Research Conference*, (Monterey, CA), pp. 350–353, 1994.

[37] M. Kitamura, "Computer simulation of director profile in three-dimensional electric field," vol. 26, pp. 540–542, SID Symposium Digest, 1995.

[38] J. H. Ferziger, "Ordinary differential equations i: Initial value problems," in *Numerical methods for engineering application*, pp. 75–82, New York: Wiley Interscience, 2 ed., 1998.

[39] R. C. Jones, "New calculus for the threatment of optical systems. vii. properties of the n-matrices.," *J. Opt. Soc. Am.*, vol. 38, pp. 671–685, 1948.

[40] H. Wöhler and M. E. Becker, "The optics of liquid crytals (seminar notes)," in *Eurodisplay'93* (SID, ed.), (Strasbourg (France)), SID, 1993.

[41] P. Allia, C. Oldano, and L. Trossi, "Linear optics: Matrix methods," in *Physics of liquid crystalline materials* (I.-C. Khoo and F. Simoni, eds.), pp. 337–363, Gordon and Breach, 1991.

[42] H. L. Ong, "Electro-optics of electrically controlled birefringence liquid crystal displays by 2x2 propagation matrix analytic expression at oblique angle," *Appl. Phys. Lett.*, vol. 59, no. 2, pp. 155–157, 1991.

[43] V. Gu and P. Yeh, "Extended jones matrix method ii," *J. Opt. Soc. Am. A*, vol. 10, ao. 5, pp. 966–973, 1993.

[44] A. Lien, "A detailed derivation of extended jones matrix representation for twisted nematic liquid crystal displays," *Liq. Crys.*, vol. 22, no. 2, pp. 171–175, 1997.

[45] R. M. A. Azzam, "Principal lincar polarization states of an optical system," *J. Opt. Soc. Am. A*, vol. 9, no. 1, pp. 147–150, 1992.

[46] C. H. Gooch and H. A. Tarry, "The optical properties of twisted nematic liquid crystal structures with twist angles <=90," *J. Phys.*, vol. 8, no. D: Applied Physics, pp. 1575–1584, 1975.

[47] D. W. Berreman, "Optics in smoothly varying anisotropic planar structures: Application to liquid crystal twist cells," *J. Opt. Soc. Am. A*, vol. 63, no. 11, pp. 1374–1380, 1973.

[48] R. H. Good and A. Karali, "Transmission of light through a slab of cholesteric liquid crystal," *J. Opt. Soc. Am. A*, vol. 11, no. 7, pp. 2145–2155, 1994.

[49] J. A. Fleck and M. Feit, "Beam propagation in uniaxial anisotropic media.," *J. Opt. Soc. Am. A*, vol. 73, no. 7, pp. 920–926, 1983.

[50] B. Witzigmann, P. Regli, and W. Fichtner, "Rigorous electromagnetic simulation of liquid crystal displays," *J. Opt. Soc. Am. A*, vol. 15, no. 3, pp. 753–757, 1998.

[51] J. A. Kosmopoulos and H. M. Zenginoglou, "Geometrical optics approach to the nematic liquid crystal grating: numerical results," *Appl. Opt.*, vol. 26, no. 9, pp. 1714–1721, 1987.

[52] G. Beliakov, "Reconstruction of optical characteristics of waveguide lenses by the use of ray tracing," *Appl. Opt.*, vol. 33, no. 16, pp. 3401–3404, 1994.

[53] W. H. Southwell, "Ray tracing in gradient-index media," *J. Opt. Soc. Am.*, vol. 72, no. 7, pp. 908–911, 1982.

[54] B. E. A. Saleh and M. C. Teich, "Polarization and crystal optics," in *Fundomentals of Photonics*, Wiley Series in Pure and AppliedOptics, pp. 193–234, New York: John Wiley and Sons, Inc., 1991.

[55] B. E. A. Saleh and M. C. Teich, *Fundamentals of Photonics*. Wiley Series in Pure and Applied Optics, New York: John Wiley and Sons, Inc., 1991.

[56] T. K. Gaylord and M. G. Moharam, "Thin and thick gratings: terminology clarification," *Appl. Opt.*, vol. 20, no. 19, pp. 3271–3273, 1981.

[57] D. W. Berreman, "Optics in stratified anisotropic media: 4x4 matrix formulation," *J. Opt. Soc. Am. A*, vol. 62, no. 4, pp. 502–510, 1972.

[58] K. Lu and B. E. A. Saleh, "Reducing berreman's 4x4 formulation of liquid crystal display optics to 2x2 jones vector equations," *Opt. Lett.*, vol. 17, no. 22, pp. 1557–1559, 1992.

[59] H. G. Galabova, Y. Jiang, L. Li, S. Vartak, and S. M. Faris, "Achromatic wide angle clc-based broadband polarizer," vol. 30, SID Symposium Digest, 1999.

[60] N. Collings, M. Bouvier, B. Züger, and J. Grupp, "High contrast twisted nematic liquid crystal cells for optical switching at 1.55mm," *Mol. Cryst. Liq. Cryst.*, vol. 1, pp. 277–285, 1998.

[61] R. Völkel, H. P. Herzig, P. Nussbaum, R. Dändliker, and W. B. Hugle, "Microlens array imaging system for photolithography," *Opt. Eng*, vol. 35, no. 11, pp. 3323–3330, 1996.

[62] T. Scharf, J. Fontannaz, M. Bouvier, and J. Grupp, "An adaptative microlens formed by homeotropic aligned liquid crystal with positive dielectric anisotropy," *Mol. Crys. Liq. Crys.*, vol. 331, pp. 235–543, 1999.

[63] Z. He, Z. Ling, T. Nose, and S. Sato, "Liquid crystal display devices with slit patterned electrode structures," *Jpn. J. Appl. Phys.*, vol. 36, pp. 2128–2133, 1997.

[64] G. Chilaya, G. Hauck, H. D. Koswig, and D. Sikharulidze, "Electric-field controlled color effect in cholesteric liquid crystals and polymer-dispersed cholesteric liquid crystals," *J. Appl. Phys.*, vol. 80, no. 3, pp. 1907–1909, 1996.

[65] D. Subacius, S. V. Shiyanovskii, P. Bos, and O. D. Lavrentovich, "Cholesteric gratings with field-controlled period," *Appl. Phys. Lett.*, vol. 71, no. 23, pp. 3323–3325, 1997.

[66] S. N. Lee, L. C. Chien, and S. Sprunt, "Polymer-stabilized diffraction gratings from cholesteric liquid crystals," 1998.

[67] R. G. Lindquist, J. H. Kulick, G. P. Nordin, J. M. Jarem, S. T. Kowel, and M. Friends, "High-resolution liquid crystal phase grating formed by fringing fields from interdigitated electrodes," *Opt. Lett.*, vol. 19, no. 9, pp. 670–672, 1994.

[68] H. Okada, P. J. Bos, and H. Onnagawa, "In-plane liquid crystal beam steering devices with a beam separation structure," *Jpn. J. Appl. Phys.*, vol. 37, pp. 2576–2580, 1998.

[69] J. Chen, P. J. Bos, H. Vithana, and D. L. Johnson, "An electro-optically controlled liquid crystal diffraction grating," *Appl. Phys. Lett.*, vol. 67, no. 18, pp. 2588–2590, 1995.

[70] M. Lu and K. H. Yang, "Nematic liquid crystal phase-gratings for reflective spatial light modulators," *Jpn. J. Appl. Phys.*, vol. 37, pp. L587–L590, 1998.

[71] J. W. Goodman, "Fresnel and fraunhofer diffraction," in *Introduction to Fourier Optics* (S. W. Director, ed.), pp. 63–95, New York: McGraw Hill, 2nd international ed., 1996.

[72] N. A. Riza and M. C. deJule, "Three-terminal adaptive nematic liquid crystal lens device," *Opt. Lett.*, vol. 19, no. 14, pp. 1013–1015, 1994.

[73] S. Kowel, P. Kornreich, and A. Nouhi, "Adaptive spherical lens," *Appl. Opt.*, vol. 23, no. 16, pp. 2774–2777, 1984.

[74] D. P. Resler, D. S. Hobbs, R. C. Sharp, L. J. Friedman, and T. A. Dorschner, "High-efficiency liquid-crystal optical phased-array beam steering," *Opt. Lett.*, vol. 21, no. 9, pp. 689–691, 1996.

[75] N. Wolffer, B. Vinouze, and P. Gravey, "Holographic switching between single mode fibres based on electrically addressed nematic liquid crystal gratings with high deflection accuracy," *Opt. Comm.*, vol. 160, pp. 42–46, 1998.

[76] M. Waeny, "Elektrisch schaltbare strahlablenker mit fluessigkristallen," diploma, Paul Scherrer Institut and IMT, 1997.

[77] M. Oh-e and K. Kondo, "The in-plane switching of homogeneously aligned liquid crystals," *Liq. Crys.*, vol. 22, no. 4, pp. 379–390, 1997.

[78] M. Oh-e, M. Yoneya, and K. Kondo, "Switching of negative and positive dielectro-anisotropic liquid crystals by in-plane electric fields," *J. Appl. Phys.*, vol. 82, no. 2, pp. 528–535, 1997.

[79] M. Oh-e, M. Yoneya, M. Ohta, and K. Kondo, "Dependence of viewing angle characteristics on pretilt angle in the in-plane switching mode," *Liq. Crys.*, vol. 22, no. 4, pp. 391–400, 1997.

[80] S. Tahata, A. Tsumura, M. Mizunuma, A. Tamatani, Y. Morii, M. Fujii, and F. Matsukawa, "A wide viewing angle lcd controlled by a lateral field," *SPIE*, vol. 3015, pp. 134–140, 1997.

[81] U. Vokinger, "Happy i," 1998.

[82] P. F. McManamon, E. A. Watson, T. A. Dorschner, and L. J. Barnes, "Applications look at the use of liquid crystal writable gratings for steering passive radiation," *Opt. Eng.*, vol. 32, no. 11, pp. 2657–2664, 1993.

[83] P. F. McManamon, T. A. Dorschner, D. L. Corkum, L. J. Friedman, M. Holz, S. Liberman, H. Q. Nguyen, D. P. Resler, R. C. Sharp, and E. A. Watson, "Optical phased array technology," *Procs. IEEE*, vol. 84, no. 2, pp. 268–298, 1996.